IMPACT OF CLIMATE-RESPONSIVE STRATEGIES ON FUTURE AIR QUALITY UNDER CLIMATE CHANGE

A Thesis
Presented to
The Academic Faculty

by

Peng Liu

In Partial Fulfillment
of the Requirements for the Degree
Doctor of Philosophy in the
School of Chemical and Biomolecular Engineering

Georgia Institute of Technology
May 2016

COPYRIGHT ©2015 BY PENG LIU

IMPACT OF CLIMATE-RESPONSIVE STRATEGIES ON FUTURE AIR QUALITY UNDER CLIMATE CHANGE

Approved by:

Dr. Athanasios Nenes, Advisor
School of Chemical and Biomolecular Engineering
Georgia Institute of Technology

Dr. David S. Sholl
School of Chemical and Biomolecular Engineering
Georgia Institute of Technology

Dr. Armistead G. Russell, Co-Advisor
School of Civil & Environmental Engineering
Georgia Institute of Technology

Dr. Martha A. Grover
School of Chemical and Biomolecular Engineering
Georgia Institute of Technology

Dr. Yi Deng
School of Earth and Atmospheric Sciences
Georgia Institute of Technology

Date Approved: Nov 23, 2015

To my dear grandparents,
To grow up is a pain, but I think I made it.

ACKNOWLEDGEMENTS

During the years pursuing the degree, I have been helped, encouraged, and supported by a lot of people, to whom I have been truly grateful. I feel very lucky to have them along the way. Above all, I would love to thank my family, who always trust me, and give me the faith to trust myself. I would like to thank my lovely group mates, Ricardo, Shannon, Jack, James, Marcus, Sunni, Xiaowen, Lucas, and Cong, for all the insightful discussions and for all the fun moments we had over the years. I would especially like to thank Dr. Yongtao Hu, who gave me the first hint of the numerical modeling involved in this thesis, and has always been patient and helpful. Last, I would like to express my deepest appreciation to my advisors, Dr. Athanasios Nenes and Dr. Armistead G. Russell, for their guidance, patience, and support that in many times went beyond the academy.

TABLE OF CONTENTS

LIST OF TABLES

LIST OF FIGURES

Page

LIST OF SYMBOLS AND ABBREVIATIONS

$P(t, L)$	Similarity at time t at the spatial scale of L
$< >$	Spatial average over the simulation domain
σ	Stefan-Boltzmann constant
Z_0	Momentum roughness length
m	Wave number in zonal direction
n	Wave number in meridional direction
Δx	Grid spacing in x direction
Δy	Grid spacing in y direction
PM	Particulate Matter
US EPA	U.S. Environmental Protection Agency
IPCC	Intergovernmental Panel on Climate Change
GHGs	Green House Gases
WRF	Weather Research and Forecast
SMOKE	Sparse Matrix Operating Kernel for Emissions
CMAQ	Community Multiscale Air Quality

RCMs	Regional Climate Models
CTMs	Chemical Transport Models
GCMs	General Circulation Models
VOCs	Volatile Organic Compounds
LSMs	Land Surface Models
LULC	Land Use and Land Cover
PBL	Planetary Boundary Layer
CCN	Cloud Condensation Nuclei
IN	Ice Nuclei
T_{SK}	Skin temperature
MODIS	Moderate Resolution Imaging Spectroradiometer
LST	Land surface temperature derived from remote sensing
GVF	Green Vegetation Fraction
UCMs	Urban Canopy Models
UHI	Urban Heat Island
UHS	Urban Heat Sink
NLCD	National Land Cover Database

BB	Biomass burning
SEUS	Southeastern U.S.A
NARR	North American Regional Reanalysis
LW	Long wave radiation
SW	Short wave radiation
T2	Air temperature at 2m height
LES	Large Eddy Simulation

SUMMARY

Air quality has been an important concern related to public health. This research is motivated by the challenge to understand how U.S. air quality will be affected by climate-responsive strategies under climate change. Numerical modeling is chosen as the primary research tool through the study, which mainly focused on the modeling development and its applications. The complexity and uncertainty of the responses in air quality to different strategies, to a large extent, stem from the modeling of regional climate at resolutions fine enough for a regional air quality study. Therefore, as to the model development, the thesis work contributes from two aspects to improve the modeling of regional climate: a nudging approach during the dynamic downscaling, and a sub-grid approach based on the existing Noah land surface model. With the sharpened modeling tools, the applications include (A) to estimate the impact of climate responsive strategies on future climate and air quality; (B) to study the impact of heat mitigation scenarios for urban areas on urban heat island (UHI) effect and heat related death; and (C) to investigate the impact of biomass burning on regional climate of the southeastern U.S. Given that the applications above were carried out as the collaborations with other graduate students and research groups, not all of them are included in this thesis. This thesis will focus on the modeling development, validation, and a case study in application (B) and the application (C), respectively.

CHAPTER 1

INTRODUCTION

Air pollution is one of the leading risk factors to public health at both global and regional scales [1], and anthropogenic emission has been the primary concern to solve the problem. In the United States, significant improvement in air quality has been achieved by the implementation of emission controls under the Clean Air Act during the past decades, though some regions still fail to meet the National Ambient Air Quality Standards (NAAQS) for a single or multiple pollutants (Figure 1.1).

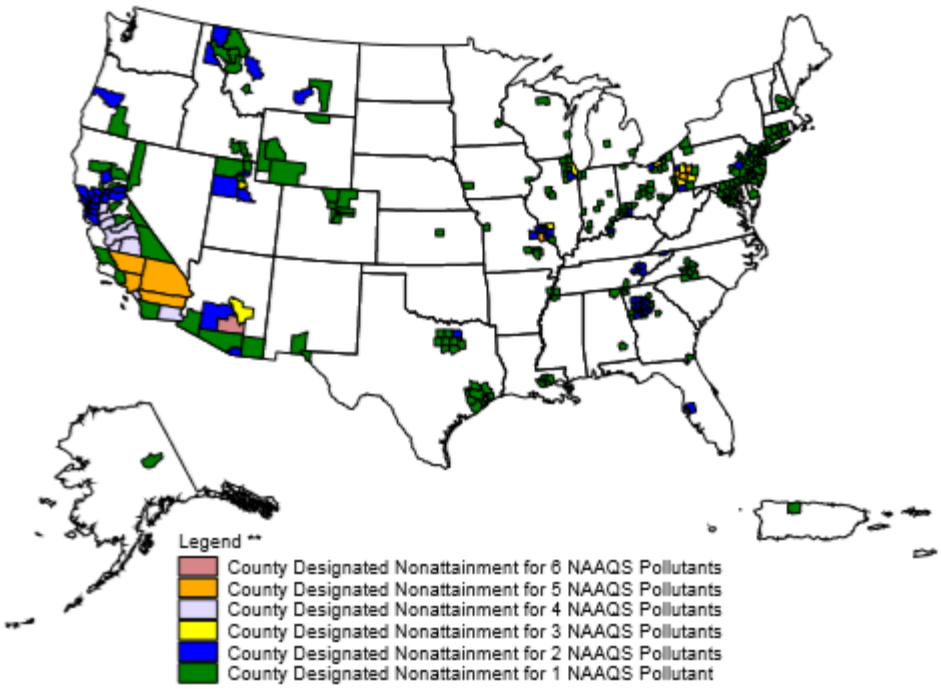

Figure 1.1 Counties designated "Nonattainment" for Clean Air Act's National Ambient Air Quality Standards (NAAQS) based on the "The Green Book Nonattainment Areas for Criteria Pollutants" (as of October 01, 2015) by U.S. Environmental Protection Agency (US EPA). The NAAQS are health standards for Carbon Monoxide, Lead (1978 and

2008), Nitrogen Dioxide, 8-hour Ozone (2008), Particulate Matter (PM-10 and PM-2.5, 1997, 2006 and 2012), and Sulfur Dioxide (1971 and 2010). Partial counties, those with part of the county designated nonattainment and part attainment, are shown as full counties on the map. (map available from http://www3.epa.gov/airquality/greenbook/mapnpoll.html)

1.1 Air Quality Challenges Under Climate Change

New challenges for air quality, however, have emerged due to the climate change for two reasons. First, the concentration and composition of pollutants can be affected by climate change via different processes and factors, such as transport, mixing, chemistry, background concentrations of relative chemicals, and etc. In 2001, the National Research Council (NRC) raised the question "… to what extent will the United States be in control of its own air quality in the coming decades" given that "… changing climatic conditions could significantly affect the air quality in some regions of the United States… ". The Intergovernmental Panel on Climate Change (IPCC) warned of possible air quality degradation in some regions due to climate change in the Fourth Assessment Report (IPCC, 2007) [2]. Since then, the air quality implications of a changing climate have been investigated intensively [3-12]. Meanwhile, better performance in regional climate modeling is desired, because meteorological fields play a paramount role in the formation, mixing and transport of air pollutants.

Second, in response to future climate change, a variety of climate-responsive strategies, including technologies, practices and policies has been brought up to mitigate the global warming. However, how air quality will respond to different climate-responsive strategies is in question. Therefore, when assessing the climate-responsive strategies, their impact on climate and air quality should be considered in a joint and integrated manner. If climate-responsive strategies can be demonstrated to have mutual benefits in reducing global warming and regional air pollution, the attractiveness of such

strategies will increase. Conversely, climate change mitigation strategies that could degrade regional air quality become less attractive.

Why do some climate-responsive strategies tend to favor air quality while others may have adverse impact on air quality? This is because forcings important to local/regional air quality, such as emissions and land use, usually change while emissions in green-house gases (GHGs) are reduced owing to the climate-responsive strategies. For example, some technologies, such as carbon capture and sequestration (CCS), would significantly co-benefit air quality, resulting from the extremely low emissions in particulate matter (PM), NOx and SO_2 as well as almost-zero CO_2 emissions, compared to the current technology employed in power plants using either coal or natural gas. Some strategies, such as switching from gasoline to diesel or ethanol for fuels, may be less beneficial, or even potentially harmful to air quality due to the increased emissions of specific pollutants [13]. Another climate-responsive strategy of particular interest is to replace the fossil fuels with biomass fuels. The state of Georgia (U.S.), for example, plans to produce 15% of its transportation fuels from locally produced biofuels by the year 2020 (http://energy.georgiainnovation.org/feature_projects/details/56: accessed Sept. 26, 2008). To meet the demand for biomass fuel, land use is expected to change (e.g. conversion from forest to agricultural land, or vice versa). Meanwhile, emissions from biomass burning is expected to increase because prescribed burning will become more frequent and extensive in order to increase productivity, reduce wildfire risk and sustain wildlife habitat. Both the change in land use and emissions may affect the local/regional air quality directly, or may modify the local/regional climate as well, and in return affect the air quality. The involved feedbacks of air pollutants to meteorology make it more complex to assess the response of air quality to such climate-responsive strategy.

To deal with both of the two challenges, an essential step is to build the reliable relationship between an individual forcing (such as land use, emissions, and etc.) and its response in regional climate. With improved estimate in meteorological fields, the impact

on air quality is expected to be better estimated. In addition, the relationship between an individual forcing and its responses in climate and air quality is especially valuable information for policy-makers. Efforts have been made to build such relationships based on observation data. However, in the real world, forcings usually come into play at the same time. In addition, responses in climate are highly non-linear. Therefore, it is very difficult to distinguish the impact of one forcing from another based merely on observations. Numerical modeling provides such an alternative that we can rely on to establish the relationship between a single (or multiple) forcing and its responses. Therefore, throughout this work, numerical modeling is chosen as the primary tool to fulfill the scientific task. Towards the ultimate goal to understand how air quality responds to a variety of climate-responsive strategies, the main contribution of this thesis involves the model developments to improve the performance of regional climate modeling, with two case studies included as model application.

1.2 Modeling Framework

A variety of numerical modeling tools have been available to simulate the forcings and responses that we are interested in. During this study, the framework and main model platform is based on the "Models-3" regional air quality modeling system. Models-3 has three primary components, a regional meteorological model, an emissions processor, and a chemical transport model. The first two parts will provide the meteorological conditions and emission information that are necessary to drive a chemical transport model. In this research, the Weather Research and Forecast (WRF) [14], Sparse Matrix Operating Kernel for Emissions (SMOKE) [15] and the Community Multiscale Air Quality (CMAQ) [16] models are chosen as the three components of the modeling system. The WRF/SMOKE/CMAQ system represents the state-of-the-science in regional air quality modeling. WRF, SMOKE and CMAQ are relatively well known and extensively documented models. In addition to its scientific foundation, the widening community of

users and continuous model development make this system attractive for use. For example, CMAQ is equipped with the Decoupled, Direct Method in Three Dimensions (DDM-3D) [17, 18], a direct and efficient method to calculate the sensitivity of model outputs to model inputs. High-order DDM [19] has been available recently to make the calculation more accurate. The adjoint method, a backward method for sensitivity analysis, has also been under development [20, 21] for CMAQ. Such sensitivity methods are powerful tools for diagnosing the model responses of air quality to the changes in the input fields and parameters.

1.2.1 Modeling of Regional Climate and Air Quality

The meteorological fields at local/regional scales are essential to the model performance of chemical transport models. To obtain the projections of future climate, general circulation models (GCMs) serve as the primary tool to understand how global climate will change under different scenarios [22]. However, meteorological information provided by GCMs becomes unreliable at scales smaller than about 200 km [23], the spatial resolution of which is still too coarse to be directly used for regional climate and air quality studies [24]. Therefore, downscaling GCMs outputs has been proposed to bridge the gap of scale discrepancy between the global and regional climate information. Downscaling has been categorized into four types (Table 1.1) based on the research purpose [25]. This study involves downscaling application of type 2 and type 4. From type 1 to type 4, constraints from real-world observation diminish. As a result, the accuracy of small-scale features generated by downscaling deteriorates as more climate variables are from model predictions instead of observations. However, such uncertainties in regional climate are mainly due to the issues in GCMs [26], which are beyond the scope of this study.

Table 1.1 Four types of downscaling applications

Type	Purpose	Input to RCMs
1	short-term numerical weather prediction	global analysis of observed data plus observed regional initial conditions
2	regional climate simulation	atmosphere information from global or regional re-analyses in which the regional initial conditions are forgotten
3	seasonal prediction	global atmospheric model prediction with prescribed observed surface conditions (e.g., sea surface temperatures)
4	climate prediction	multi-decadal global climate model prediction based on prescribed radiative forcing

Downscaling can be achieved by statistical methods (called statistical downscaling) or by high-resolution regional climate models (RCMs) (called dynamical downscaling). This work will only focus on the latter. Although dynamic downscaling has been validated and widely applied by a lot of studies [25-32], issues still remain, which has been well summarized by previous studies [27, 33, 34]. Among these issues, a key challenge has been to balance the model performance of RCMs in adding small-scale features which are the internal solutions of RCMs developed as a result of the combination of model physics and high-resolution surface information, and simultaneously retaining the large-scale features which are inherited from the RCMs input fields (e.g. GCMs outputs). One of the main contributions of this thesis work is that it demonstrated how model performance of RCMs can be improved by the implementation of different nudging techniques during dynamic downscaling.

In this work, CMAQ is used to simulate air quality at fine scales. CMAQ, as one of the state-of-the-art chemical transport models (CTMs), integrates the understandings of the complex processes that affect the concentrations of pollutants in the atmosphere. CMAQ is a three-dimensional Eulerian (i.e., gridded) model that simulates ozone,

particulate matter (PM), toxic airborne pollutants, visibility, and acidic and nutrient pollutant species throughout the troposphere. It comprises of detailed chemical and physical processes in gas, particle and cloud phases in order to simulate the complex interactions of atmospheric chemistry and physics.

A main issue of the commonly used WRF/SMOKE/CMAQ system is that this system usually does not include feedbacks of air pollutants to climate, especially the feedback of aerosols. Aerosol feedback can be summarized as chemistry-aerosol-cloud-radiation-climate. On one hand, atmospheric aerosols affect climate through 1) changing the radiation balance by directly absorbing and scattering the solar radiation (known as aerosol direct effect); 2) modifying meteorological variables that depend closely on vertical and horizontal radiation distributions, such as planetary boundary layer (PBL) height, circulation, convection and clouds (e.g. aerosol semi-direct effect); and 3) altering the formation of clouds and precipitation by serving as cloud condensation nuclei (CCN) and ice nuclei (IN) (known as aerosol indirect effect). Therefore, feedbacks of air pollutants can be important to local/regional climate. On the other hand, the modified meteorological conditions will in return affect the pollutants, because spatial distributions and formation mechanisms of aerosols are governed by atmospheric processes including chemistry in gas phase, aerosol thermodynamic and dynamic processes, cloud processes, and deposition, all of which are closely related to meteorological conditions. The complexity and the importance of this feedback has made it one of the most interesting uncertain research areas in understanding climate change and its potential impact on air quality [2, 35, 36]. Hence, in this work, the recently developed coupled WRF-CMAQ system [37] will be used.

1.2.2 Modeling of Emission and Land Surface

SMOKE, an emissions processing system designed to create gridded, speciated and hourly emissions, is used to provide the emission inputs to CMAQ. SMOKE input data

consists of emissions inventories, temporal and chemical speciation profiles, spatial surrogates, gridded meteorology and land use data, and other ancillary files for specifying the timing, location, and chemical nature of emissions.

In order to obtain the projections in emissions inventories for different climate-responsive strategies, EPA MARKAL 9R (an acronym for MARKet Allocation) [38, 39] is used. MARKAL is an energy system model that projects the penetration of technologies and their associated emissions. Candidate strategies come from other studies [40-42], which are economically attractive with great potential for application in the future and. Three steps involve in preparing the emissions corresponding to different climate-responsive strategies. First, by implementing MARKAL 9R, different climate-responsive strategies will lead to different changes in emissions, including volatile organic compounds (VOCs), NOx, SOx, and speciated PM. Then, the emission outputs from MARKAL 9R are mapped to specific inventory categories in standard emission inventories, which can be used as input for SMOKE. Last, SMOKE will create the final emissions information as the input for CMAQ. The emission modeling and emission inputs for CMAQ involved in this work were mainly prepared by Dr. Marcus Trail (a former graduate student advised by Dr. Russell), Dr. Yongtao Hu (a senior research scientist in Georgia Tech) and the collaborators from NESCAUM (Northeast States for Coordinated Air Use Management, Boston, Massachusetts, U.S.A).

Land surface is another important forcing to local/regional climate and air quality [43-46], and expected to change significantly in the future. Land-atmosphere interactions in numerical models are described by land surface models (LSMs), by which the lower boundary of the flux exchange between land and atmosphere are computed, including energy, moisture and momentum.

In this study, the Noah LSM is chosen as the primary tool to study the impact of land use change on local/regional climate and air quality. The Noah LSM [47] has been widely used in both regional and global weather and climate modeling. However, a main

limitation for the Noah LSM is that Noah LSM only considers the dominant land use type in each grid cell, which may limit its utility. For example, in response to climate change, there is a growing interest in the heat-adaptation strategies for urban areas. These strategies usually involve the modification in land use and land cover (LULC) over urban areas. Detailed LULC scenarios at fine scales (e.g. tens to hundreds of meters) are developed from the perspective of city-planning. The scenarios then need to be investigated by regional climate and air quality models. However, the fine-scale modifications in LULC may not be reflected in Noah LSM because dominant land cover type of a grid cell usually does not change, unless simulations of ultra-high resolution are conducted, which can be subject to numerical issues as well as excessive computational cost. Therefore, in this work, a sub-grid approach for the Noah land surface model is developed to overcome its limitation of using a single, dominant land cover type across a grid cell for the assessment of surface properties. In addition, the model performance is evaluated at the sub-grid level by comparison with remote sensing- derived data. To our knowledge, this is the first effort to evaluate the modeled sub-grid properties at such a fine scale against satellite observations.

1.3 Thesis Outline

Towards the ultimate goal of understanding the impact of climate-responsive strategies on air quality, this thesis, based on the current "Model-3" modeling framework and the issues that may potentially limit the performance of regional climate modeling, focuses on the model developments from two aspects. In chapter 2, it is demonstrated that the performance of dynamic downscaling process can be in general improved with the implementation of spectral nudging. In Chapter 3, a sub-grid approach based on the Noah land surface model is developed and evaluated. The new approach makes the "Model-3" modeling framework more powerful, especially when studying the impact of land use/land cover change at urban scales, when land use/land cover change is expected to

occur at scales much finer than the typical spatial resolution of regional climate models. Chapter 4 involves a case study of this kind. Then, in chapter 5, the impact of another important forcing on regional climate, namely emissions from biomass burning, is investigated using the state-of-the-science coupled WRF-CMAQ. The research directions in the future are discussed in chapter 6.

CHAPTER 2

IMPROVING THE PERFORMANCE OF DYNAMIC DOWNSCALING BY SPECTRAL NUDGING[1]

During the dynamic downscaling, the simulation of regional climate models (RCMs) tends to drift away from the driving fields. Developing a solution that addresses this issue, by retaining the large scale features (from the large-scale fields) and the small-scale features (from the RCMs) has led to the development of "nudging" techniques. Here, we examine the performance of two nudging techniques, grid and spectral nudging, in the downscaling of NCEP/NCAR data with the Weather Research and Forecasting (WRF) Model. The simulations are compared against the results with North America Regional Reanalysis (NARR) data set at different scales of interest using the concept of similarity. To our knowledge, this study is the first effort to demonstrate that with the appropriate choice of wave numbers, spectral nudging outperforms grid nudging in the capacity of balancing the performance of simulation at the large and small scales.

[1] This chapter is based on the publication: Liu, P., Tsimpidi, A. P., Hu, Y., Stone, B., Russell, A. G., and Nenes, A.: Differences between downscaling with spectral and grid nudging using WRF, Atmos. Chem. Phys., 12, 3601-3610, doi:10.5194/acp-12-3601-2012, 2012.

2.1 Motivation

Dynamical downscaling has been at the forefront of model development of regional climate models [48], and now is being used to address how regional air quality would change in future climate. In the process of dynamical downscaling, errors are introduced primarily in two ways. One is due to incomplete model physics. The other type of error results from the downscaling itself. For example, dynamical downscaling typically starts with a set of coarse-resolution large-scale fields, which are used as the initial conditions (ICs) and lateral and surface boundary conditions (LBCs) for the RCMs. As the simulation evolves, the internal solution developed by RCMs may be affected by the size of domain, the spin-up period and update frequency of LBCs. Issues related to dynamic downscaling have been summarized by previous studies [27, 33, 34].

A key source of downscaling errors is the inconsistency along boundaries [49, 50] since RCM simulation drifts away from the GCMs driving fields. It has been a challenge to balance the performance of RCMs in adding small-scale features and simultaneously retaining the large-scale features. Nudging techniques are introduced to RCMs to address this issue. A nudging term is added to the predictive equation of the variable to be nudged in its grid-point model:

$$\frac{\partial Q}{\partial t} = S(Q) - \eta(Q - Q^*) \quad (1)$$

Where Q is the meteorological field to solve by RCMs, t the integration time, $S(Q)$ the internal solution of field Q by RCMs, Q^* the same meteorological field as Q but from the driving data of RCMs or from observations, and η the nudging coefficient.

The lateral boundary relaxation technique was brought up [49], in which the solution of RCM is nudged to the driving field in a "buffer zone" along boundaries. However, this technique is still unable to fulfill the goal of retaining the large-scale information provided by GCMs at the interior of the modeling domain. In order to capture the features of the driving force through the domain, grid nudging was developed [51] and has been

applied to downscaling reanalysis data for regional air quality modeling of historical episodes. In this technique, nudging is conducted in every grid cell. Another nudging technique that has gained interest recently is spectral nudging [52, 53], in which the nudging term is spectrally expanded in both the zonal and meridional directions:

$$Q(x,y,t) - Q^*(x,y,t) = \sum_{m=0}^{L_m/2\Delta x} \left(A_m \cos\left(\frac{2\pi m x}{L_m}\right) + iB_m \sin\left(\frac{2\pi m x}{L_m}\right)\right) \times \sum_{n=0}^{L_n/2\Delta y} \left(A_n \cos\left(\frac{2\pi n y}{L_n}\right) + iB_n \sin\left(\frac{2\pi n y}{L_n}\right)\right) \quad (2)$$

Where Δx Δy are the grid spacing in x and y direction respectively, L_m L_n the size of modeling domain in x and y direction respectively, m n the wave number in x and y direction respectively, and A B the coefficients for Fourier transform.

In spectral nudging, only the waves under selected wave numbers are kept in the nudging term. All other waves are filtered out. By keeping the long waves in the nudging term, studies [54, 55] found that spectral nudging can help eliminate the large-scale precipitation bias, and, at the same time, maintain the features of small scale.

The existing studies, which used dynamical downscaling for the purpose of regional air quality modeling [3, 31, 56-59], have implemented boundary relaxation, grid nudging, or no nudging. Few have involved spectral nudging. Spectral nudging, however, may have an advantage over no nudging or boundary nudging [60-63] and could theoretically outperform grid nudging. From the perspective of spectrum, grid nudging modifies the RCMs results throughout the spectrum with the same strength, however, the short-wave information provided by RCMs is thought to be more reliable than that provided by GCMs. Therefore, grid nudging has the risk of over-forcing the RCMs at small scales [25]. However, few studies discuss the comparison between grid and spectral nudging and how to determine optimal cut-off wave numbers for spectral nudging.

This study aims at improving the performance of downscaling using spectral nudging, with a particular focus on developing regional-scale fields for assessing the impact of climate change on air quality. The main difficulties involve how to evaluate the results between grid and spectral nudging and how to determine the appropriate wave numbers for spectral nudging. In order to address these issues, the performance of downscaling at multiple scales was investigated. The applications of scale analysis in the evaluation of downscaling are well summarized by other study [64].

2.2 Methods

2.2.1 Model Description and Simulation Design

Weather Research and Forecasting (WRF) model [14] version 3.1.1 is used in this chapter as the regional climate model for dynamic downscaling. To mimic the spatial resolution of GCMs output, NCEP/NCAR reanalysis data is used to drive the WRF. The NCEP/NCAR reanalysis data has a spatial resolution of 2.5×2.5 degree and is archived every 6 hours. The NCEP/NCAR data is chosen not only to provide the driving fields for WRF, but also to facilitate the evaluation the downscaling performance using different nudging techniques. Four historical episodes, including July 2009, October 2009, January 2010 and April 2010, each of which represents a season, are investigated by WRF with grid nudging, spectral nudging and no nudging respectively. The modeling domain covers the COntiguous United States (CONUS) and portions of southern Canada and northern Mexico, and is centered at 40°N and 97°W with dimensions of 162×126 horizontal grids cells with a grid-spacing of 36 km. It contains 35 vertical levels, with the top pressure of 5000pa.

The physical configurations in WRF are kept the same for all the simulations in this study, except for the nudging technique employed. Both grid and spectral nudging are configured to nudge temperature and horizontal winds, but water vapor mixing ratio can

only be nudged in grid nudging, and geo-potential height only in spectral nudging. Only horizontal winds are nudged at all vertical levels, while no nudging is conducted for other variables within the planetary boundary layer (PBL). The strategy for grid nudging is based on previous studies [51, 65], which showed that this configuration reduced the bias most. For spectral nudging, same nudging strategy is used within PBL to keep the simulation consistent with grid nudging, and above PBL, geopotential field is nudged, instead of water vapor mixing ratio, which does not have large-scale features as strong as other fields and would not be nudged in the spectral nudging of WRF. The nudging coefficients for all variables for both grid and spectral nudging are set to be 0.0003 s^{-1} [66]. During the simulation, nudging is conducted every 6 hours consistent with the frequency of the NCEP/NCAR reanalysis data. When spectral nudging is conducted, all waves with wave numbers greater than a preset number are not nudged. In this study, the wave number in both directions is set to be 3 (m=n=3, where m and n represent the wave number in zonal and meridional directions, respectively). This preliminary choice is made based on two considerations. One is the scale of the driving field, in which the GCM is able to provide reliable information and this information is also expected to be captured by RCM. Previous study [53] determined that scales of about 15º and larger are considered to be reliably analyzed by NCEP. The other consideration is the size of WRF domain. In this study, the WRF modeling domain is about 6000 km×4600 km in zonal and meridional direction respectively. Hence, wave number 3 is employed as the first choice in both directions in order to capture NCEP/NCAR features of scale about 2000km. Sensitivity tests on cut-off wave number choice are conducted later to investigate the impact of wave number.

2.2.2 Evaluation Method

The concept of similarity [53] is used to evaluate the downscaling performance at different scales, using the metric, $P(t,L)$,

$$P(t,L) = 1 - \frac{\left\langle \left[\psi(t,L) - \psi^*(t,L) \right]^2 \right\rangle}{\left\langle \psi(t,L)^2 \right\rangle} \tag{3}$$

where t is the simulation time, L the scale of interest, $P(t,L)$ the similarity, $\psi(t,L)$ the input field (e.g., the NCEP/NCAR data), $\psi^*(t,L)$ the output field (e.g., the WRF output), < > the spatial average over the modeling domain. Similarity at different scales of interest is calculated every six hours just after the nudging is updated by calculating the representative values of $\psi(t,L)$ and $\psi^*(t,L)$ at different scales. The performance of downscaling at large and small scales is evaluated in the opposite way with respect to similarity using equation (3). For large scales, it is better when the downscaling results are more consistent with the input fields, so higher similarities are desired; while for small scales, the results are better when more variance is added, so lower similarities are desired.

The question arises as to how the large and small scales are determined. As mentioned previously, information at about 15º and larger is considered to be reliably analyzed by NCEP. Accordingly, 2000 km and larger is chosen as the "large scale". At this scale, when comparing WRF output with NCEP/NCAR input data, the higher the similarity is, the RCM is viewed as performing better. As to the "small scale", instead of the WRF resolution of 36 km, 300 km is chosen in order to capture features that occur at multiple grids, which are more reliably captured by RCMs than individual grid cells. And compared to the NCEP/NCAR data, 300km is a small scale, and the RCMs should be adding variability that is not resolved by the GCM. Therefore, 300km is chosen as the "small scale" and lower similarities are desired.

The calculation of similarity at 2000 km or 300 km involves three steps. First, the WRF input field, namely the NCPE/NCAR data, is interpolated to the same resolution as

the WRF results. Second, grid cells of 36 km resolution in the modeling domain are re-divided according to the scale of interest so that each new "aggregated" cell includes multiple original grid cells. For each new cell, its representative values of input and output fields, namely $\psi(t,L)$ and $\psi^*(t,L)$ in equation (3), are computed from the spatial average of the 36km NCEP/NCAR data and WRF results. Finally, similarity is calculated by equation (3). At the large-scale case, for instance, the NCEP/NCAR 2.5×2.5 degree data is first interpolated to a 36km resolution, so that for both input and output fields, the modeling domain includes 162 (zonal) by 126 (meridional) cells. Because we are concerned about the features at the scale of about 2000 km, the modeling domain could be re-divided into 3×3 new cells, each of which has 54×42 original cells, and then $\psi(t,L)$ and $\psi^*(t,L)$ at the scale of 2000 km are calculated by averaging the 54×42 cells of input and output fields respectively.

A critical issue is whether the decrease in similarity at small scales is of reasonable magnitude. In other words, if the current choice of wave numbers insufficiently constrains the RCM so that the similarity decreases too much at the small scale, and vice versa. To answer this question, the North America Regional Reanalysis (NARR) data set [67] is used to assess the appropriate level of similarity decrease between large and small scales. NARR data set has a spatial resolution of the 32 km and the quality of NARR data has been evaluated with surface station and sounding measurements [67]. In one case, if NARR data set is consistent with NCEP/NCAR data at the large scale, which means similarities between these two data set are high, NARR data set is viewed as the best result we could have after downscaling from NCEP/NCAR data, and the similarity between NCEP/NCAR and NARR data at the small scale could serve as the criteria for a reasonable range of similarity for the small-scale results. If the NARR data set can not provide enough high similarity at the large scale, similarity between NCEP/NCAR and NARR at small scale can not be used directly as the criteria. Instead, the difference of

similarity between large and small scale would be used as the reference when assessing whether the change in similarity between input and downscaled fields is reasonable.

2.3 Comparison between Grid and Spectral Nudging

Given that the ultimate goal is to use the downscaled meteorological fields to drive a regional chemical transport model, we are especially concerned about the fields that will significantly affect the concentration of pollutants. Therefore, we investigate temperature, horizontal kinetic energy (as a surrogate for wind speed), and hydro fields, including clouds, accumulated precipitation and water vapor mixing ratio; analysis is carried out at three vertical levels, the surface, 850hpa and 500hpa. Only the results of Jul 2009 are shown here, since other tested episodes give similar results.

2.3.1 Similarity in Temperature at Different Scales

Temperature is nudged in both grid and spectral nudging. At 850hpa, at the large scale, both spectral and grid nudging results have high similarities through the simulation period (Figure 2.1 a). The temporal means of similarity $P(t, L)$ at the large scale (as summarized in Table 2.1) is over 0.99999 for both. Hence, the spatial averaged relative difference of temperature is less than about 0.3% (square root of (1-0.99999)), which means at the large scale, both of the nudging techniques are equally capable of capturing the features of the driving fields.

High similarity is not true at small scales, as spectral nudging gives a much lower similarity than grid nudging. Lower similarity is expected at small scales because variance is expected to be added by the RCM. The similarity between the NCEP/NCAR and NARR data (Figure 2.1 b, Table 2.2) is calculated to determine whether or not the lower similarities given by nudging techniques at the small scale are consistent with using NARR data. The decrease in similarity between NCEP/NCAR and NARR data from large to small scale indicates that at the small scale, spectral nudging performs

better than grid nudging because of a lower similarity. If nudging is not applied during the simulation, the RCM is not able to retain the features at large scales (Table 2.1).

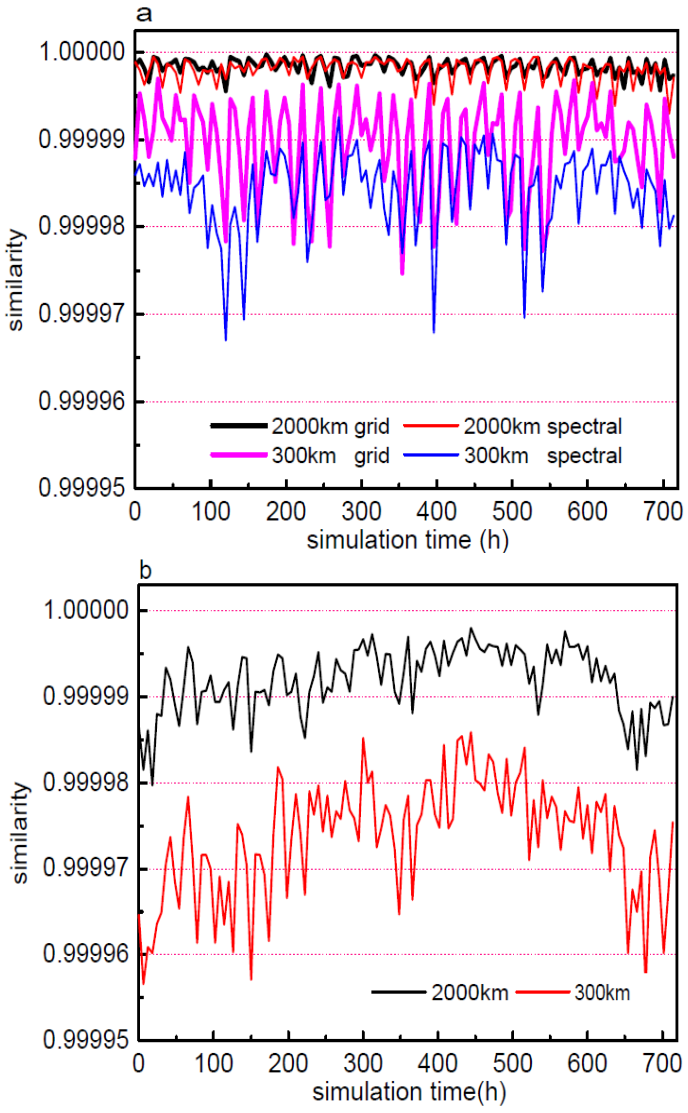

Figure 2.1 Time series plots of similarity in temperature at 850hpa at 2000km and 300km scales for Jul 2009: (a) similarity between NCEP/NCAP and downscaling results by WRF with grid and spectral nudging, respectively; (b) similarity between NCEP/NCAR and NARR data.

Table 2.1 Mean and standard deviation of similarities in temperature between NCEP/NCAR and WRF outputs during July 2009 at different scales

	Grid Nudging		Spectral Nudging		No Nudging	
	2000 km	300 km	2000 km	300 km	2000 km	300 km
T_s	0.99999 ± 0.8×10^{-5}	0.99995 ± 1.6×10^{-5}	0.99999 ± 0.5×10^{-5}	0.99995 ± 1.3×10^{-5}	0.99998 ± 1.0×10^{-5}	0.99992 ± 1.8×10^{-5}
T_{850}	0.999998 ± 1.0×10^{-6}	0.999990 ± 5.4×10^{-6}	0.999998 ± 1.4×10^{-6}	0.999984 ± 4.7×10^{-6}	0.999988 ± 5.5×10^{-6}	0.999958 ± 9.0×10^{-6}
T_{500}	1.000000 ± 0.1×10^{-6}	0.999999 ± 0.2×10^{-6}	1.000000 ± 0.1×10^{-6}	0.999997 ± 0.7×10^{-6}	0.999990 ± 4.2×10^{-6}	0.999974 ± 8.1×10^{-6}

Subscripts s, 850 and 500 stand for surface, 850hpa and 500hpa.

Table 2.2 Mean and standard deviation of similarities in temperature between NCEP/NCAR and NARR during July 2009 at different scales

	2000km	300km
T_s	$0.99998\pm1.0\times10^{-5}$	$0.99994\pm1.9\times10^{-5}$
T_{850}	$0.999992\pm3.8\times10^{-6}$	$0.999974\pm6.7\times10^{-6}$
T_{500}	$0.999997\pm1.6\times10^{-6}$	$0.999991\pm2.4\times10^{-6}$

Subscripts s, 850 and 500 stand for surface, 850hpa and 500hpa.

The similarity results at 500hpa are very similar to the results at 850hpa, except that the difference of similarity between grid and spectral nudging is even smaller. At the small scale, for instance, the difference of the mean between the two nudging techniques is on the order of 10^{-6}, and the difference of standard deviation of similarity on the order of 10^{-7}.We have to ask does the small difference in similarity really matter? In other

words, we want to know if the similarity is still able to be used to assess the performance of downscaling, or it is just noise when the difference of similarity is very small. To answer this question, we compare the probability distribution of the temperature difference between the NCEP/NCAR data and the WRF output (by grid and spectral nudging respectively) with the distribution of temperature difference between NCEP/NCAR data and NARR data (Table 2.3). Changing from the large to small scale, the width of the distribution provided by grid nudging changes little compared with spectral nudging and NARR data, which indicates that for the temperature field at 500hpa, grid nudging over-forces the RCM results towards the driving fields and the small-scale features expected from RCM are hindered.

Table 2.3 Mean and standard deviation (SD) of the distribution of temperature difference at 500hpa of July 2009 at different scales

Data set	at the Scale of 2000km		at the Scale of 300km	
	Mean (K)	SD (K)	Mean (K)	SD (K)
NARR minus NCEP/NCAR	-0.11	0.533	-0.10	1.219
Grid Nudging minus NCEP/NCAR	-0.09	0.173	-0.09	0.337
Spectral Nudging minus NCEP/NCAR	-0.08	0.209	-0.07	0.837

To further investigate whether the larger variance provided by spectral nudging is reasonable or not, the correlation between WRF output and NARR data is investigated by orthogonal regression (Figure 2.2). At the small scale, spectral nudging improves the correlation with NARR data compared with grid nudging by giving a slope more close to 1. Other regression methods, such as least square regression, are also tested and we get consistent results. The results above indicate that the metric of similarity at different scales is important in evaluating the performance of downscaling, even when the difference between similarity values is very small. At the surface, grid and spectral

nudging show little difference in similarity, which is not unexpected because temperature is not nudged within the PBL.

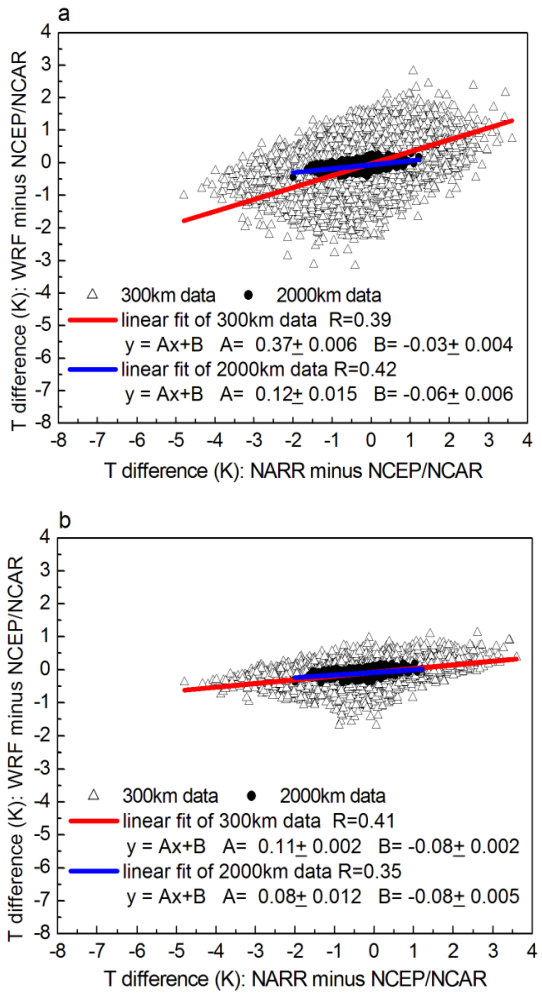

Figure 2.2 Correlation for the temperature anomaly from NCEP/NCAR data at 500hpa at 2000km and 300km scales for Jul 2009 with linear regression of 95% confidence. (a) anomaly of WRF output by spectral nudging vs anomaly of NARR data; (b) anomaly of WRF output by grid nudging vs anomaly of NARR data.

2.3.2 Similarity in Horizontal Kinetic Energy at Different Scales

Spectral nudging, likewise, performs better than grid nudging for horizontal kinetic energy (KE) with comparable similarity at the large scale and lower similarity consistent

with NARR at the small scale at both 850hpa (Figure 2.3) and 500hpa (Table 2.4; Table 2.5). In addition, at the small scale, the similarity found using spectral nudging varies temporally with the same trend as that of NCEP/NCAR and NARR data (Figure 2.3). However, the similarity found using grid nudging shows little such variability.

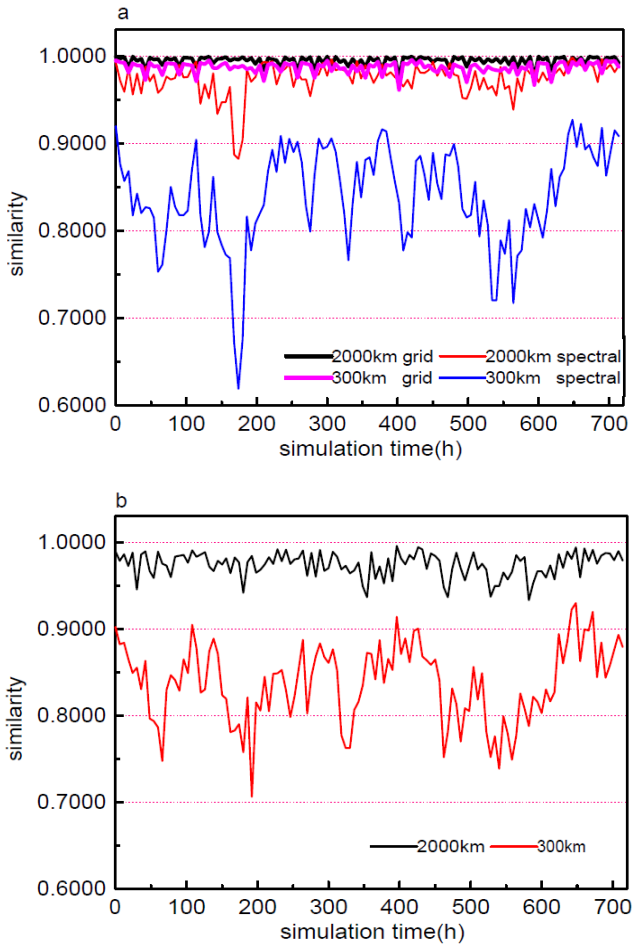

Figure 2.3 Time series of similarity in horizontal kinetic energy at 850hpa at 2000km and 300km scales for Jul 2009: (a) similarity between NCEP/NCAP and downscaling results by WRF by grid and spectral nudging respectively; (b) similarity between NCEP/NCAR and NARR data.

By comparing with the change in episode-averaged similarity between NCEP/NCAR and NARR from large to small scale (Table 2.5), the results (Table 2.4) also show that

spectral nudging performs better than grid nudging in the magnitude of similarity decrease. In addition, for grid nudging, little change exists in standard deviation of the similarity when changing from large to small scale; while for spectral nudging, larger changes shows, with the magnitude of change more similar to that between NCEP/NCAR and NARR. If no nudging is used, low similarities occur with standard deviation much larger compared with that from NCEP/NCAR and NARR, indicating that constrains exposed on WRF are not strong enough to retain the features at large scales from the driving fields. The results at the surface are similar to those at 500hpa and 850hpa.

Table 2.4 Mean and standard deviation of similarities in horizontal kinetic energy between NCEP/NCAR and WRF outputs during July 2009 at different scales

	Grid Nudging		Spectral Nudging		No Nudging	
	2000 km	300 km	2000 km	300 km	2000 km	300 km
KE_s	0.98 ± 0.9×10^{-2}	0.94 ± 1.7×10^{-2}	0.94 ± 3.4×10^{-2}	0.83 ± 5.8×10^{-2}	0.87 ± 11.7×10^{-2}	0.65 ± 14.3×10^{-2}
KE_{850}	1.00 ± 0.5×10^{-2}	0.99 ± 0.7×10^{-2}	0.97 ± 1.9×10^{-2}	0.84 ± 5.7×10^{-2}	0.89 ± 7.8×10^{-2}	0.61 ± 12.3×10^{-2}
KE_{500}	0.999 ± 0.5×10^{-3}	0.997 ± 0.9×10^{-3}	0.996 ± 3.3×10^{-3}	0.940 ± 2.1×10^{-2}	0.946 ± 2.8×10^{-2}	0.769 ± 6.5×10^{-2}

Subscripts s, 850 and 500 stand for surface, 850hpa and 500hpa.

Table 2.5 Mean and standard deviation of similarities in horizontal kinetic energy between NCEP/NCAR and NARR during July 2009 at different scales

	2000km	300km
KE_s	$0.90\pm5.3\times10^{-2}$	$0.76\pm7.8\times10^{-2}$
KE_{850}	$0.97\pm1.4\times10^{-2}$	$0.84\pm4.5\times10^{-2}$
KE_{500}	$0.993\pm4.5\times10^{-3}$	$0.940\pm2.1\times10^{-2}$

Subscripts s, 850 and 500 stand for surface, 850hpa and 500hpa.

The improvement in the decrease of similarity from large to small scale implies significant differences of the nudged variable between grid and spectral nudging. For example, at 500hpa (Table 2.4), grid nudging leads to a mean KE similarity of 0.997 at the small scale; while spectral nudging decreases the mean of similarity to 0.940. The kinetic energy difference between grid and spectral nudging is around 20%.

2.3.3 Similarity in Hydro-Fields at Different Scales

Difference in similarities for horizontal kinetic energy (KE) suggests that the results from grid and spectral nudging can be very different for fields strongly affected by KE, such as clouds and precipitation, both of which are important in regional climate and air quality modeling. Therefore, we further investigated the impact of nudging techniques on hydro-fields, including column total clouds, accumulated precipitation and water vapor mixing ratio at different height.

Cloud hydrometeor mixing ratios provided by WRF are used to calculate the monthly averaged cloud mass (including cloud water, cloud rain, ice, snow and graup) in each column and compared with the convective cloud fraction averaged from NARR data archived every 3 hours. The convective cloud from NARR data is used for comparison instead of total cloud because the horizontal resolution of WRF in this study is not high enough to explicitly resolve such clouds. The two nudging techniques lead to greater differences over the middle and the eastern regions of the U.S, with spectral nudging better capturing the cloud features (Figure 2.4). The superiority of spectral nudging becomes more apparent when comparing the precipitation with NARR data (Figure 2.4b). Grid nudging significantly depresses the precipitation across the middle of the U.S. Moreover, in the southeast, results from spectral nudging more closely resemble NARR data than grid nudging. Spectral nudging (Figure 2.4d) generates the similar rainfall region over the east coast, although the rainfall region shifted toward southwest compared with NARR data; grid nudging (Figure 2.4f) did not generate this feature at all.

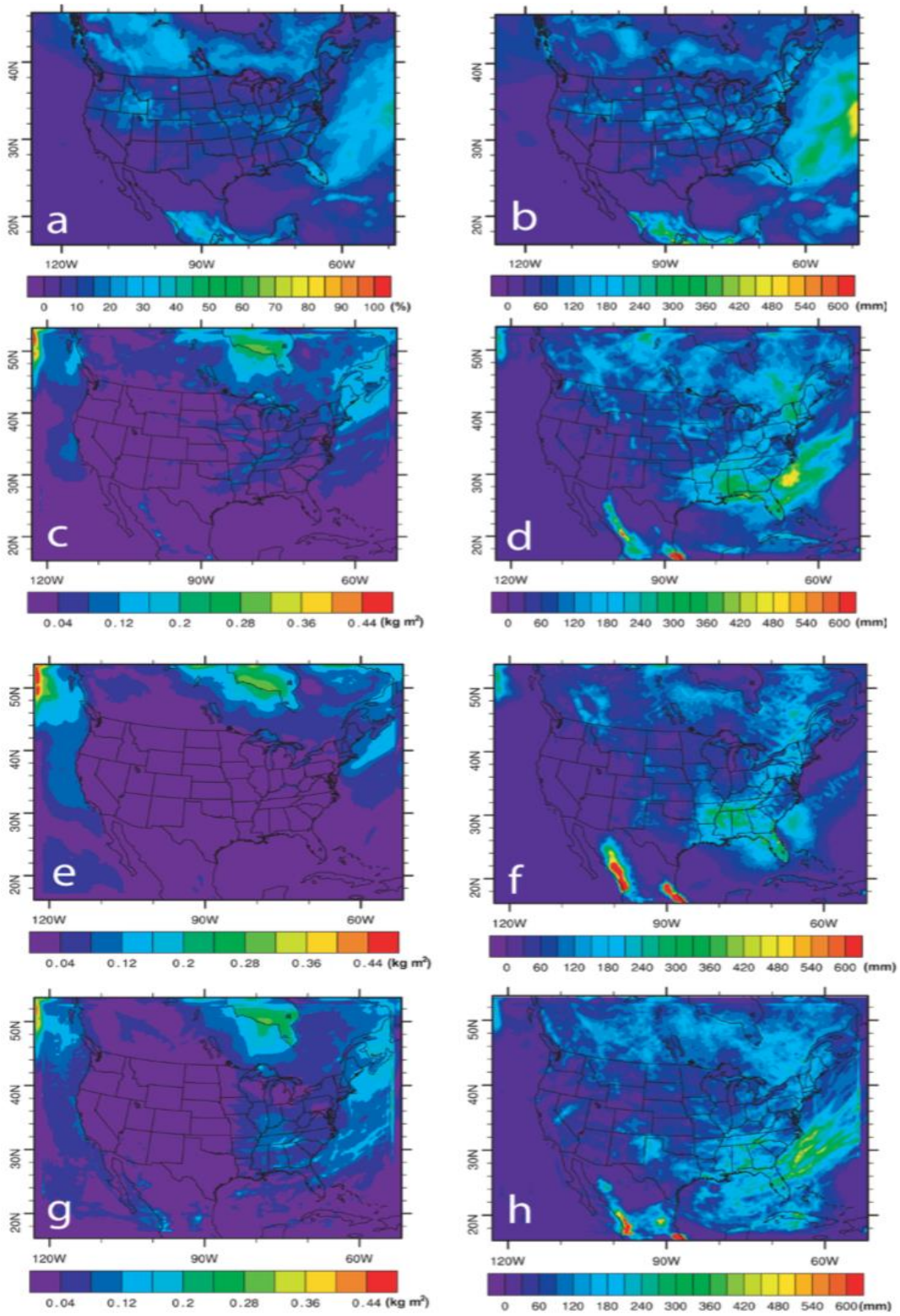

Figure 2.4 Comparison of monthly averaged cloud fraction (or cloud water) and monthly accumulated precipitation using WRF and NARR data for Jul 2009. (a)(b) NARR; (c)(d)

WRF simulation using spectral nudging; (e)(f) WRF simulation using grid nudging; (g)(h) WRF simulation using "grid no gq".

The difference in precipitation shown above includes the impact of nudging horizontal KE and water vapor mixing ratio as well. To exclude the impact of the latter, another case is tested, in which grid nudging is used with the same configuration described in section 2.2.1, except that the nudging of water vapor mixing ratio is turned off (this case is referred to as "grid no gq" and the cases with nudging configuration described in section 2 are referred to as "grid" and "spectral" respectively). Compared with "grid" case, "grid no gq" case shows little difference in the similarities of temperature and horizontal KE at both large and small scales (not shown here). Therefore, the difference of precipitation between "grid no gq" and "spectral" cases better represents the impact of horizontal KE. We find out that compared with "spectral" case, "grid no gq" case (Figure 2.4h) reproduces precipitation regions over Canada and the Atlantic Ocean, although with less strength. However, it still fails to generate the features across the middle of the U.S. In addition, much more rainfall occurs over the Gulf of Mexico.

For water vapor mixing ratio, only grid nudging, not spectral nudging, is applied to water vapor mixing ratio in the "grid" case of this study. If spectral nudging is used, the correction to water vapor mixing ratio results from the changes in other fields.

At the large scale, the similarity using spectral nudging is still as high as that by grid nudging at the surface and 850hpa (Table 2.6). At 500hpa, however, spectral nudging does not maintain the large-scale features as well as grid nudging (Figure 2.5 a), although the similarity of grid and spectral nudging at 500hpa differs little for temperature and horizontal kinetic energy. This can be linked to the prediction of cloud formation, which is at a scale smaller than that is captured by the GCM, and is very sensitive to a number of local factors.

Table 2.6 Mean and standard deviation of similarities in water vapor mixing ratio (QV) between NCEP/NCAR and WRF outputs during July 2009 at different scales

	Grid Nudging		Spectral Nudging		No Nudging	
	2000 km	300 km	2000 km	300 km	2000 km	300 km
QV_s	0.993 ± 4.3×10^{-3}	0.986 ± 7.3×10^{-3}	0.990 ± 5.4×10^{-3}	0.979 ± 8.8×10^{-3}	0.988 ± 6.5×10^{-3}	0.974 ± 9.8×10^{-3}
QV_{850}	0.999 ± 1.8×10^{-3}	0.991 ± 6.6×10^{-3}	0.996 ± 1.4×10^{-3}	0.969 ± 7.5×10^{-3}	0.993 ± 3.4×10^{-3}	0.944 ± 1.6×10^{-2}
QV_{500}	1.000 ± 0.8×10^{-3}	0.996 ± 3.2×10^{-3}	0.970 ± 1.7×10^{-2}	0.880 ± 2.6×10^{-2}	0.970 ± 1.6×10^{-2}	0.817 ± 4.9×10^{-2}

Subscripts s, 850 and 500 stand for surface, 850hpa and 500hpa.

When changing from large to small scale, for all the vertical layers of interest, spectral nudging provides the desired decrease in similarity of water vapor mixing ratio as compared to NARR; while for grid nudging, little difference occurs at small and large scales (Table 2.6; Table 2.7).

Table 2.7 Mean and standard deviation of similarities in water vapor mixing ratio (QV) between NCEP/NCAR and NARR during July 2009 at different scales

	2000km	300km
QV_s	$0.994\pm3.5\times10^{-3}$	$0.981\pm6.9\times10^{-3}$
QV_{850}	$0.994\pm2.2\times10^{-3}$	$0.967\pm6.4\times10^{-3}$
QV_{500}	$0.992\pm4.6\times10^{-3}$	$0.950\pm1.4\times10^{-2}$

Subscripts s, 850 and 500 stand for surface, 850hpa and 500hpa.

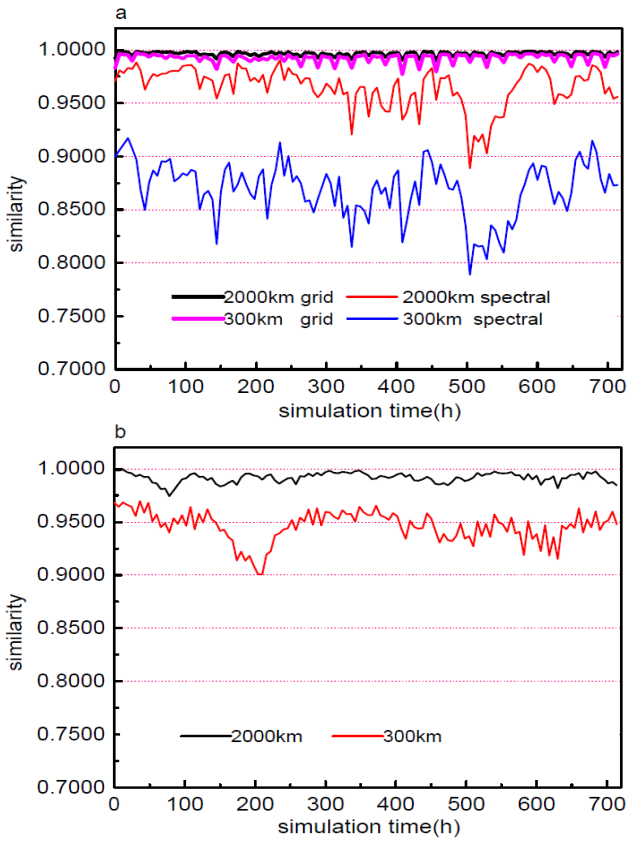

Figure 2.5 Time series of similarity in water vapor mixing ratio at 500hpa at 2000km and 300km scales for Jul 2009: (a) similarity between NCEP/NCAP and downscaling results by WRF by grid and spectral nudging; (b) similarity between NCEP/NCAR and NARR data set.

2.4 Sensitivity to Wave Number in Spectral Nudging

Choice of wave numbers in spectral nudging impacts the quality of downscaling. If the wave number is too large, which means the nudging term includes all the longer waves under the selected wave numbers, the results of spectral nudging would approach grid nudging, because the results are overly forced at the smaller scale. If the wave number is too small, the long waves included in the nudging term may not be able to represent enough energy to force the RCMs to replicate the large scale features. Here, a sensitivity test is conducted to investigate how the fields of interest respond to changes in wave

numbers. In previous simulations, the wave numbers for spectral nudging were 3 in both zonal and meridional directions. Here, wave number sets of m=n=2 and m=n=6 (m and n represent the wave number in zonal and meridional direction, respectively) are tested as applied to the four episodes simulated and the similarity at the large and small scales are investigated.

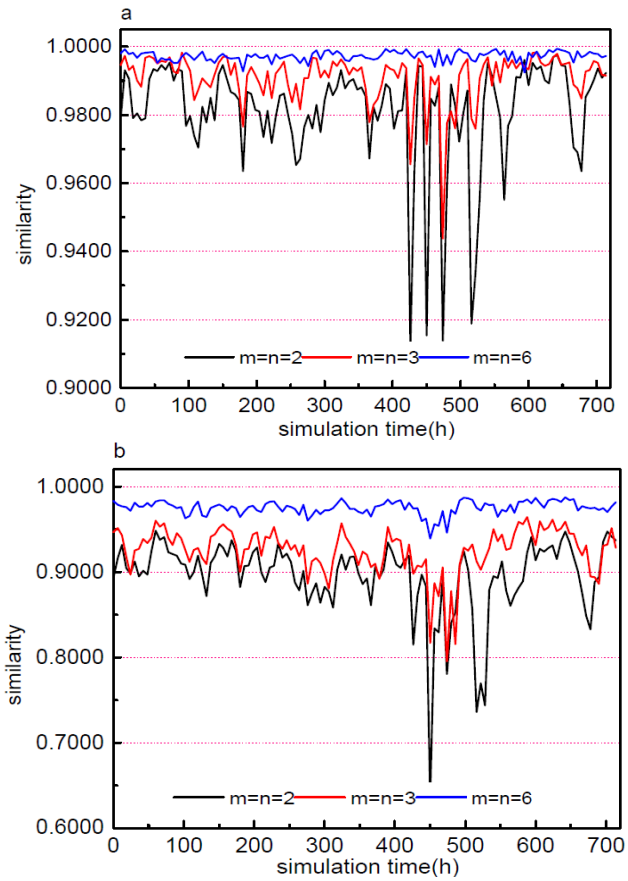

Figure 2.6 Time series of similarity in horizontal kinetic energy at 850hpa for Jan2010 by spectral nudging with different wave numbers: (a) similarity between NCEP/NCAP and downscaling results by WRF at 2000km scale; (b) similarity results at 300km scale. m and n represent the wave number in zonal and meridional direction respectively.

For the horizontal kinetic energy, at both large and small scales (Figure 2.6), when the wave numbers decrease, the ability of spectral nudging to follow large scale features

becomes weaker as the similarity markedly decreases; while when wave numbers increase, the performance of spectral nudging approaches grid nudging by giving high similarity values, particularly at the small scale. As the wave numbers increase, the variability and difference between large and small scales also becomes smaller (Table 2.8). It is critical to choose the wave numbers which are able to generate reasonable difference between different scales and variability at the scales of interest. Therefore, the results in section 2.3 indicate that the choice of wave numbers m=n=3 is an appropriate choice for the studied case here. The results of sensitivity test also suggest that similarity at the small scale is more sensitive to wave number choice than that at the large scale (Table 2.8). As wave number increase, the loss of variability at small scales is larger than the increase of consistency at large scales. Therefore, smaller wave numbers are preferred as long as the features at the large scales of interest can be captured, in order to reduce the loss of variability at small scales. The choice of wave number had little impact on temperature and water vapor.

Table 2.8 Temporal mean and standard deviation (SD) of the similarity (between NCEP/NCAR and WRF output by spectral nudging) in horizontal kinetic energy at 850hpa of January 2010 at the scale of 2000 km and 300 km respectively, using different wave numbers (m and n represent the wave number in zonal and meridional direction, respectively).

	at the Scale of 2000km		at the Scale of 300km	
wave number	Mean	SD	Mean	SD
m = n = 2	0.98	1.6×10^{-2}	0.90	4.5×10^{-2}
m = n = 3	0.99	0.7×10^{-2}	0.93	2.8×10^{-2}
m = n = 6	1.00	0.1×10^{-2}	0.98	0.8×10^{-2}

2.5 Conclusions

The performance of two nudging techniques, grid and spectral nudging are examined in the downscaling of NCEP/NCAR data with the Weather Research and Forecasting (WRF) Model. The simulations are compared against the results with North America Regional Reanalysis (NARR) data set at different scales of interest using the concept of similarity.

Compared with grid nudging, spectral nudging provides a better balance between the need to keep RCM results consistent with the large scale driving forces that would be provided by GCMs, and at the same time, allows more variance added at the smaller scales. The performance of spectral nudging is very good for temperature and horizontal kinetic energy at 850hpa and 500hpa. In addition, the improvement at the small scale allowed by spectral nudging is not only reflected in spatial variability, but temporal variability as well.

In order to take the advantage of spectral nudging, appropriate wave numbers should be chosen based on a thorough sensitivity analysis. The results of sensitivity tests show that for the case studied here, the choice of wave numbers set at m=n=3, or wave lengths of about 2000 km is well supported. The choice of wave numbers is determined by the size of modeling domain and the scale of driving forces that RCMs should retain. Results suggest that the similarity at the small scale is more sensitive to wave numbers than that at the large scale, and as wave numbers increase, spectral nudging performs more similarly to grid nudging and begins to over-force the RCMs results at the small scale. The sensitivity tests also imply that many of the biases of large-scale modes are associated with resolved small-scale features, and only spectral nudging can help to alleviate the biases while keeping the resolved small-scale features to a reasonable extent.

CHAPTER 3

IMPROVING THE MODELING OF LAND SURFACE BY DEVELOPING THE S-NOAH APPROACH[2]

Studies have demonstrated that anthropogenic impacts on land use/land cover (LULC) can affect historical and future climates at a variety of spatial scales. For example, many researches have focused on investigating the impact of urbanization and irrigation on surface temperature, rainfall patterns, and the hydrologic cycle at local and regional scales based on observational data [43-46, 68-70]. By comparing observation and reanalysis data, studies estimated the additional warming or cooling trends due to LULC change under the background of changing climate, with the results being sensitive to land cover type [71-73]. These approaches, however, may have difficulty in separating the impact of LULC change from synoptic-scale forcing [74] and other non-climatic factors [75, 76]. Numerical modeling provides an alternative that enables sensitivity experiments to assess climate responses to LULC change at both regional [77, 78] and global scale [79, 80].

[2] This chapter is based on the manuscript: Liu, P., Hu, Y., Stone, B., Ivey, S., Nenes, A., and Russell, A.G. (2015), Development of a subgrid approach for the NOAH land surface model and evaluation of modeled subgrid surface temperature with MODIS derived land surface temperature (submitted)

In this chapter, a subgrid approach, termed S-Noah, is developed based on the widely-used Noah land surface model [47] to overcome its limitation of using a single, dominant land cover type across a grid cell for the assessment of land surface properties. S-Noah is tested in the Weather Research and Forecasting (WRF) model [14] at a spatial resolution of 4-km×4-km. Furthermore, the model performance at sub-grid level is evaluated against remote sensing-derived land surface temperatures (LSTs). To our knowledge, this is the first study to evaluate the modeled subgrid properties at such fine scale against satellite observations.

3.1 Motivation

3.1.1 Importance to Include the Sub-Grid Heterogeneity in Land Surface Models

In numerical modeling, land surface is described by land surface models (LSMs), in which the boundaries of fluxes (including energy, moisture and momentum) exchanged between land and atmosphere are computed. Although a grid cell in the modeling domain is usually a mixture of multiple land cover types and their associated properties, some LSMs approximate the grid surface with its dominant land cover type. However, if a grid cell contains several land use types with differing properties, as found in urbanized settings, assuming a homogeneous surface poses limitations. First, research showed that partitioning of sensible heat (SH) and latent heat (LH) are sensitive to the subgrid surface heterogeneity [81]. Second, the randomly distributed turbulent motions resulting from subgrid surface heterogeneity, especially when grid spacing is coarse, can organize into mesoscale circulations [82], which may play an important role in producing and organizing clouds and precipitation, and may also interact with synoptic forcings as well. A previous study [83] summarized the issues associated with both monitoring and modeling work related to the impact of LULC change on climate. As pointed out, the

representation of mixed land use within a grid cell still remains a weak component in LSMs and additional work is needed.

3.1.2 Potential Limitations in Noah Land Surface Model due to Lack of Sub-Grid Treatment

The Noah LSM has been widely used in both regional and global weather and climate modeling. Continuous development and improvement of Noah has been conducted to improve the model performance under different conditions of weather, climate, soil and land cover types. Studies showed that Noah displays similar or superior performance compared with other LSMs [84-87] and compares well against observational data [88-92].

Although the Noah LSM has many advantages, it only considers the dominant land use type in each grid cell, which may limit its utility. For example, there is a growing interest in how adverse heat effects on human health under future climate may be alleviated by local/regional LULC modification in urban areas [93]. Detailed LULC scenarios at fine scales (e.g. tens to hundreds of meters) are available and need to be investigated by RCMs. However, the fine-scale modifications in LULC may not be reflected in Noah LSM because dominant land cover type of a grid cell usually does not change, unless simulations of ultra-high resolution are conducted, which can be subject to numerical issues as well as excessive computational cost.

One possible way to represent the land surface heterogeneity at the sub-grid level is to couple the urban canopy models (UCMs) with the Noah LSM to account specifically for the heterogeneity resulting from urban and vegetated surfaces within the same grid cell [94, 95]. However, UCMs often require very detailed urban canopy information as inputs (e.g. road dimensions and building density), but such information is usually not available when future urban land use scenarios are developed. Furthermore, the homogeneous representation of vegetated surfaces within a grid cell is usually not sufficient. On one hand, in many regions, the main LULC changes involve the changes of

green vegetation types (such as deforestation for agriculture or reforestation from agriculture) [96], which may have significant impacts on regional climate [97-99]. This is because the interaction between vegetation and atmosphere may vary strongly with vegetation type [100, 101], leading to significant differences in flux exchange (including energy, water, and momentum) between the land surface and atmosphere. On the other hand, the representation of vegetated surfaces can affect the model performance over the urban surface within the grid cell. For example, one study [102] showed that the performance of the UCMs under a range of urban environments and climatic conditions depended mostly on the representation of vegetated surface surrounding the urban areas and much less on the parameters used to describe the urban surface.

In this study, a computationally effective subgrid approach, called S-Noah is developed for the Noah LSM. A similar subgrid approach in the WRF-Noah framework was developed recently [103]. The two studies were conducted independently and the subgrid approach was evaluated differently. The other study [103] evaluated model performance at grid level. This study, however, focuses on the evaluation of subgrid performance. To our knowledge, few studies have been conducted aiming at LSM performance at the subgrid level, due to a lack of observations at a typical resolution of RCMs (e.g. 4-km).

3.2 Methods

3.2.1 Description of the S-Noah Approach

The subgrid approach, termed "S-Noah", is based on the "tile" concept, instead of dividing the land surface of a grid cell into multiple finer grid cells, because the latter is usually more computationally expensive. For example, a grid cell with typical spatial resolution in RCMs (e.g. 4-km), may contain hundreds of finer surface grid cells to

reflect the detailed LULC scenarios, while for the tile approach, the number of tiles is equal to (or less than) the number of land cover types.

Applying S-Noah involves looping the Noah LSM over all land use tiles/types constituting the land surface in each grid cell. During the each iteration, the grid cell is treated as if it were 100% covered by a specific land use type/tile. Resulting properties are referred to as the subgrid properties by S-Noah (e.g. subgrid surface skin temperature (T_{SK}) of agriculture, forest and urban are calculated by S-Noah, as illustrated in Figure 3.1 a). After looping over all land use tiles/types, subgrid properties are aggregated to grid-level properties based on flux aggregation. In other words, grid-level surface fluxes (e.g. heat and moisture) are determined by averaging the subgrid fluxes weighted by the area fraction of land use tiles within the grid cell. Grid-level T_{SK} is estimated by surface energy balance. The "skin" here refers to the surface where the phase change of water occurs (e.g. transpiration of plants, water evaporation or condensation at the bare soil). In Noah LSM, energy is balanced at the skin surface for each tile *i*:

$$(1 - A_i)F_{SW,i} + E_i\ F_{LW,i}\ - \sigma E_i T_{SK,i}^4\ \ + Q_{L,i} + Q_{S,i} + Q_{SOIL,i} = 0 \qquad (1)$$

where F_{SW} and F_{LW} represent the short wave and long wave radiation reaching the surface respectively; *A is* the albedo; *E* is the emissivity; σ is the Stefan–Boltzmann constant; and *i* is the land cover type. The first two terms represent the absorbed short and long wave energy by land cover type *i*, which depend on its specific albedo and emissivity. The third term is the outgoing long wave radiation, which is directly related to T_{SK}. Q_L and Q_S describe the energy transfer between surface and lower atmosphere in the form of latent and sensible heat, and Q_{SOIL} describes the energy transfer between surface and soil. T_{SK} of a grid cell is estimated by summing up its subgrid energy fluxes weighted by the land use fraction (Eq.2), instead of averaging the subgrid T_{SK} directly.

$$\frac{\sum_{i\neq water} f_i\left[(1 - A_i)F_{SW,i}+E_i\ F_{LW,i}+ Q_{L,i} + Q_{S,i} + Q_{SOIL,i}\right]}{(1-f_{water})} = \sigma\frac{\sum_{i\neq water} f_i\ E_i T_{SK,i}^4}{(1-f_{water})}$$

$$= \sigma T_{SK}^4 \frac{\sum_{i \neq water} f_i E_i}{(1 - f_{water})} \quad (2)$$

where f_i is the subgrid land use fraction of tile i; f_{water} is the water fraction within the grid cell; water surface is not included ($i \neq water$) when S-Noah loops over land cover types. This is because Noah is only applicable to land surfaces. Hence, S-Noah ignores the contribution from the water surfaces within the grid cell.

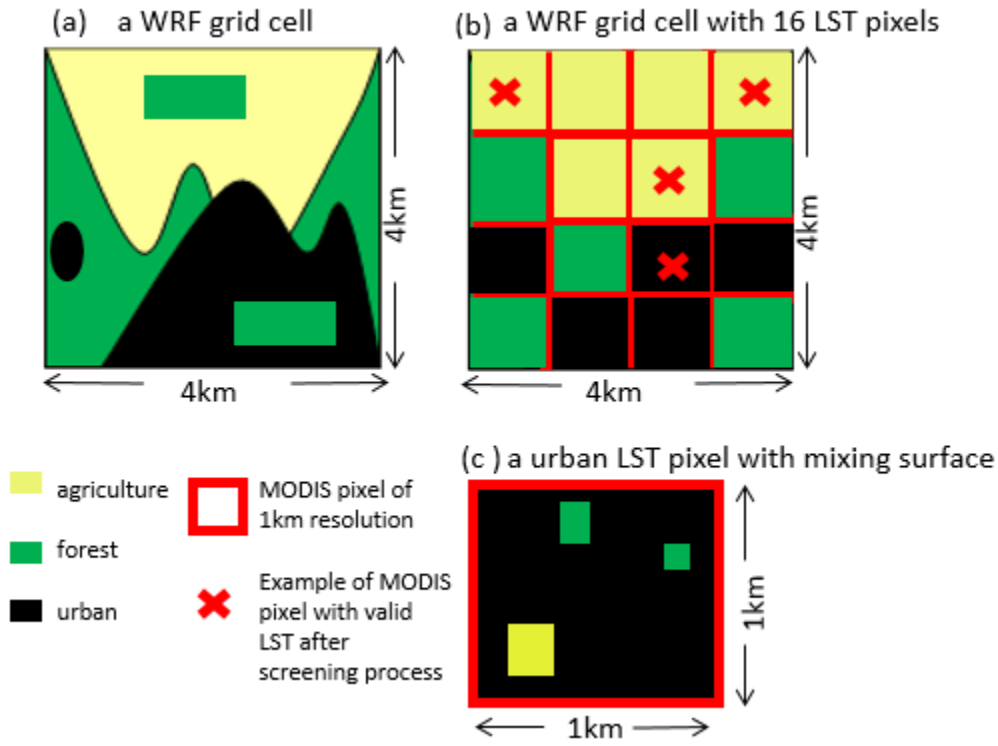

Figure 3.1 Schematic graph for: (a) a 4-km×4-km grid cell simulated by WRF, where S-Noah is applied. The schematic grid cell contains 3 land cover types/tiles. When S-Noah is applied, the T_{SK} of each subgrid tile is estimated, and referred to as subgrid $T_{SK\text{-}a}$, $T_{SK\text{-}u}$, and $T_{SK\text{-}f}$ for agriculture, urban and forest tile, respectively; (b) 1-km×1-km LST pixels overlapping the WRF grid cell, with its dominant land cover types obtained from LC-1 data. After screening process described in section 3.3.1, the valid LSTs, if any, are marked with red-cross. In this schematic plot, valid LSTs are only found for agriculture

(LST-a) and urban (LST-u), but not forest (LST-f). If multiple valid LSTs for certain land cover type exist within the same WRF grid cell, taking agriculture surface for example, 3 valid LSTs for agriculture are found, and the averaged of them will be used as the subgrid LST for agriculture (LST-a) and then compared with $T_{SK\text{-}a}$ of S-Noah; (c) mixing surface of a 1-km×1-km LST urban pixel, with its urban fraction obtained from NLCD (LC-2) data. This urban fraction is used in the screening process related to "urban fraction limit".

3.2.2 Model Description of WRF to Test S-Noah

WRF version 3.1.1 [14] was used, driven by the North American Regional Reanalysis (NARR) data [67], which covers North America at 3-h intervals and 32-km grid spacing. The simulation domains contain a 12-km×12-km resolution "mother" domain (d01) covering the southeastern US and a 4-km×4-km resolution nested domain (d02) covering most parts of the state of Georgia (Figure 3.2).

Details of the WRF configuration are as follows: 34 vertical layers with model top at 100hPa; original Noah LSM for the "mother" domain and S-Noah for the nested domain; IGBP land use data; Lin scheme for cloud microphysics; Kain-Fritsch scheme for cumulus convection; Rapid Radiation Transfer Model and Dudhia for long wave and short wave radiation transfer; Monin-Obukhov scheme for the surface layer and Yonsei University scheme for PBL; urban canopy model is off; grid nudging is on for the mother domain for wind, temperature and moisture above PBL; and one-way nesting. For evaluation purposes, the simulation period includes summers (May to September) from the year 2003 to 2005, with re-initialization every six days, the first day of which serves as a spin-up period. On one hand, this simulation period is chosen to facilitate the comparison with remote sensing data, which is described in the section 3.3.1. On the other hand, the urban heat island (UHI) effect usually exposes the most significant influence in terms of the heat stress for human health during the summer time. A control

run was also carried out with the same setup except that the original Noah LSM was applied to the nested domain.

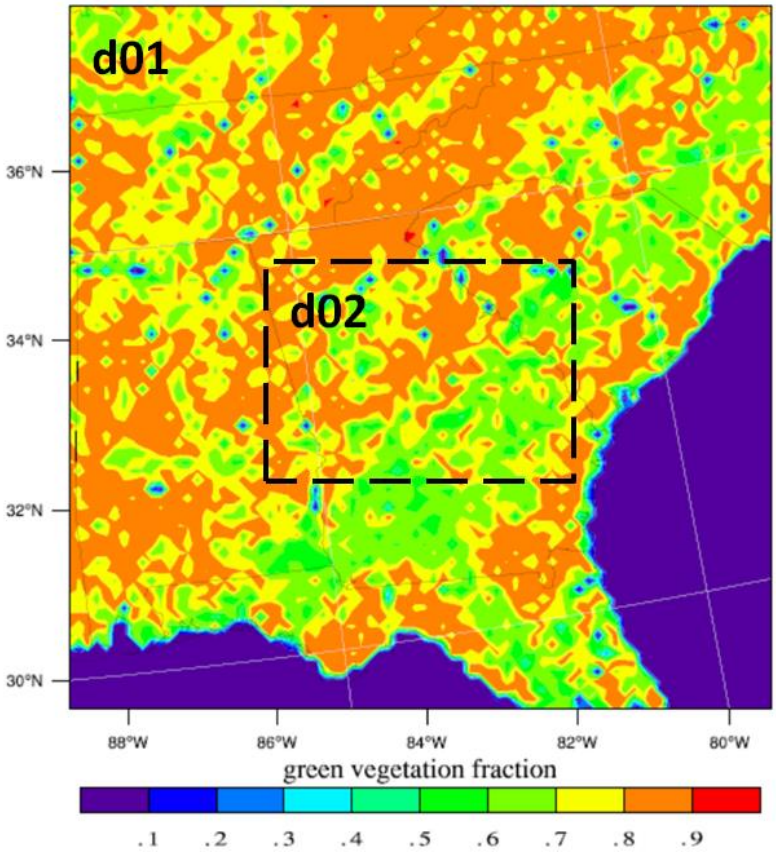

Figure 3.2 WRF simulation domains to test the S-Noah approach, including a "mother" domain (d01) of 12-km resolution, and a nested domain (d02, dashed box) of 4-km resolution covering most of the state of Georgia. The original Noah LSM is applied to domain d01, and S-Noah is applied to domain d02. Color contour represents the green vegetation fraction (GVF) in July based on MODIS-FPAR data from 2001 – 2010.

3.2.3 Specific Issues in the Application of S-Noah

Two issues need to point out here during the implementation of S-Noah. First, bulk transfer coefficient based on grid-level atmospheric stability is used for fluxes (moisture,

heat and momentum) between land surface and lower atmosphere, instead of a local transfer coefficient specific to each subgrid land cover tile. Studies [82, 103, 104] have shown that using a bulk coefficient is reasonable as long as the scale of subgrid heterogeneous land patches is small (e.g. 5km or less). As mentioned previously, the urban LULC modification of interest is usually at scales of tens to hundreds of meters. In addition, in this study, S-Noah is tested by WRF with a grid spacing of 4km. Hence, the bulk transfer coefficient is a reasonable choice here. The transfer coefficients for heat and moisture are functions of momentum roughness length, and grid averaged momentum roughness length is estimated as described below.

$$Z_0 = exp\left(\frac{\sum_{i \neq water} f_i \ln z_{0_i}}{(1-f_{water})}\right) \quad (3)$$

where Z_0 is the grid averaged momentum roughness length.

The second issue is related to the green vegetation fraction (GVF), which is an important parameter for the Noah LSM when estimating the heat and moisture partitioning between vegetated and bare soil. Surface properties, including albedo, emissivity and roughness length, also vary with GVF. Monthly GVF data is available in WRF and was derived from the MODerate Resolution Imaging Spectroradiometer (MODIS) fraction of absorbed photosynthetically active radiation (FPAR) data from 2001 – 2010 [105]. The default monthly GVF varies in space (Figure 3.2), and is not explicitly a function of land cover type. However, there has been research demonstrating that GVF varies significantly with land cover type [106]. Therefore, when applying S-Noah to a grid cell, it makes more sense to use GVF specifically for each subgrid land surface type/tile, compared with the default GVF values at the grid-level. A similar issue may also occur when historical land use data (or future land use scenarios) are used in studies, in which the corresponding change in GVF due to LULC change is usually not taken into account.

To determine the dependence of GVF on land cover type for the simulation domain d02 in this study, first, the land use information with 1-km×1-km resolution was obtained from 30 second International Geosphere Biosphere Programme (IGBP)-Modified MODIS land use data, and the corresponding monthly GVF was obtained from MODIS-FPAR GVF data. Both of the two data sets are available in the WRF package. Then, for each land cover type, all 1-km×1-km grid cells that are fully covered (> 99%) by that land cover type, were found. Last, using the grid cells found in previous step, the spatial mean and standard deviation (SD) of monthly GVF were calculated for that land use type. Consistently with existing study, the obtained GVF does vary significantly with land cover type, with the largest difference found to be about 0.3 between "evergreen broadleaf forest" and "barren and sparsely vegetated". Meanwhile, the results showed that for all the land use types, the SD of monthly GVF is within 20%. For example, GVF of croplands in July is about 0.57 ± 0.10. Existing study [107] has showed that for Noah LSM, the partitioning between latent and sensible heat changes about 10 Wm^{-2} with a GVF change of 0.25, suggesting that impact of the GVF due to its spatial variability of a single land cover type is in general weak, and that the impact due to its variance among different vegetation types is expected to be slightly stronger. Therefore, in this study, the parameter of GVF was simplified by removing its spatial variability. A lookup table including the monthly GVF for each land use type is used during S-Noah, so that only the difference in GVF related to land cover types is accounted for.

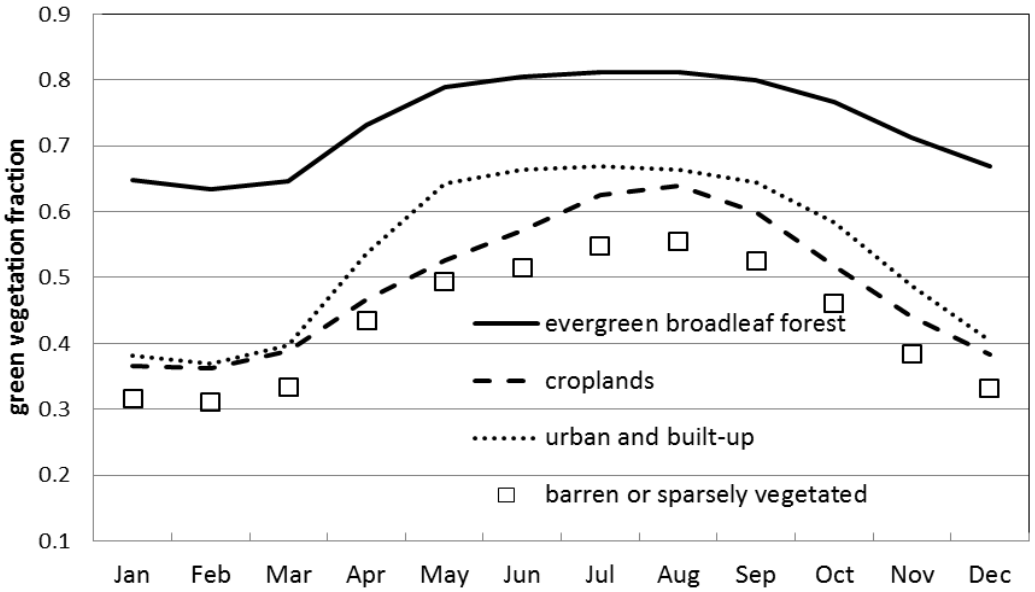

Figure 3.3 Nested-domain (namely domain d02 with resolution of 4-km) averaged monthly green vegetation fraction (GVF) for land cover types of evergreen broadleaf forest, croplands, urban and built-up, and barren and sparsely vegetated surface based on IGBP-Modified MODIS land use classification.

3.3 Evaluation of S-Noah at the Sub-Grid Level Using Land Surface Temperatures Derived from Remote Sensing

A comprehensive evaluation for S-Noah should be conducted at both the grid and subgrid levels. Grid-level performance is relatively straightforward by direct comparison with observations (e.g. 2m air temperature, ground surface flux measurement, and aircraft measurement etc, as shown in a similar study [103]. Few studies have focused on the subgrid performance because observations are usually too sparse in space or time to provide sufficient subgrid coverage. However, the model performance at the subgrid level is important, because it provides insight on whether including subgrid heterogeneity in LSM would improve model predictions as expected. A unique contribution of this study

is that the S-Noah performance at subgrid level was evaluated, with a particular focus on modeled skin temperature (T_{SK}). T_{SK} is a key property modeled by Noah LSM because it is closely related to the energy partitioning at the land surface and the energy flux exchange between land surface and lower atmosphere. In addition, T_{SK} can be directly applicable to health studies that use the quantity to assess human exposures to heat [108].

Here, the satellite-derived land surface temperatures (LSTs) are employed to evaluate the modeled T_{SK} at subgrid level. LST is derived from radiance measured by thermal infrared (TIR) sensors and is equal to the thermodynamic temperature for a homogeneous surface [109]. In Noah/S-Noah LSM, energy is balanced at the skin surface, and hence, T_{SK} also corresponds to the surface thermodynamic temperature. Therefore, T_{SK} simulated by Noah/S-Noah is comparable to the satellite-derived LST. Hereafter, T_{SK} refers to the skin temperature modeled by Noah or S-Noah, and LST refers to the surface temperature derived from remote-sensing.

The modeled subgrid T_{SK} by S-Noah is evaluated from two aspects: a) the variability in subgrid T_{SK} of a single land cover type, including urban and agricultural surfaces, respectively, and b) the skill of S-Noah in capturing the T_{SK} contrast between urban and agricultural surfaces at the subgrid level. The second aspect is of interest because surface properties of these two land types differ the most. Furthermore, maximum differences in LST are expected between urban and vegetated surfaces so that differences in LST have a larger chance to be significantly greater than the uncertainty in the retrieval of LST itself.

3.3.1 Screening the Land Surface Temperatures Derived from Remote Sensing

To evaluate the subgrid T_{SK} modeled by S-Noah, Collection-5, level-3 LST products with 1-km resolution from MODIS [110, 111] are used (MOD11A1 for Terra and MYD11A1 for Aqua satellite), with crossing time of about 1030h and 2230h for Terra, and about1330h and 0130h for Aqua. The data was obtained from the online Data Pool at the NASA Land Processes Distributed Active Archive Center (LP DAAC), USGS/Earth

Resources Observation and Science (EROS) Center, Sioux Falls, South Dakota (https://lpdaac.usgs.gov/data_access)). The MODIS Reprojection Tool (MRT) (http://lpdaac.usgs.gov/tools/modis_reprojection_tool) was used to project the MOD11A1 and MYD11A1 data onto the WRF domain d02. Hence, each 4-km×4-km grid cell in d02 (Figure 3.2) includes 16 1-km×1-km LST pixels as boxes outlined in red in Figure 3.1b. At the same time, the dominant land cover type corresponding to each 1-km×1-km LST pixel was obtained (hereafter LandCover-Data1, or LC-1, shown as colors filling the boxes outlined in red in Figure 3.1b). LC-1 data is necessary for two reasons. First, when evaluating the subgrid T_{SK} of a certain land cover type, it has to guarantee that LSTs and T_{SK} of the same land cover type are used for comparison. Second, it is necessary to ensure the consistency between the LST and the land cover type used to retrieve it, because the retrieval depends strongly on surface emissivity, which is determined by the snow cover and dominant land cover type of a pixel (in this study, no snow exists in during the simulation periods). IGBP land cover classification is used in retrieving Collection-5 LST, and the land use data was generated by observations from 2001 to 2002 (archived in product MOD12Q1). The land use data was reprojected by MRT as well onto the d02 WRF domain with 1-km×1-km resolution, so that LC-1 data maps exactly with the LST pixels. Given the large dependence of LST on the land cover type and its emissivity, the years closest to MOD12Q1 data period were chosen as the simulation episodes (summers of 2003-2005) in order to diminish the impact of inconsistent LULC on LST.

Further screening of the MODIS 1-km×1-km LST data is required for the purpose of subgrid T_{SK} evaluation. First, only LST values with the quality flags showing as “clear sky” and “good quality” are considered. Second, the viewing angle of LST is constrained within ±30° for both day and night time. During day time, the viewing angle effect on LSTs is quite large especially at large zenith angles. For example, during this study, it was noticed that at the same location, the LST at 1:30pm can be lower than that at

10:30am within the same day if the viewing angle is large, which does not make sense. One important reason is that when viewing angle is large, the radiance from areas adjacent to the pixel of interest is measured as well while measuring the radiance from the pixel of interest. For example, the instantaneous field of view (IFOV) of MODIS pixels in TIR bands is about 1-km by 1-km at nadir, 1.3-km (along-track) by 1.6-km (across-track) at viewing zenith angle near 40° and 1.7-km by 3.3-km at viewing angle of 60° [112]. As a result, the radiance measured can actually come from an area much larger than the 1-km×1-km pixel, although the resolutions of LST products and the land cover and emissivity data used to retrieve LST are as fine as 1-km×1-km. Hence, without the constraint on viewing angle, the pixels may not be able to correctly represent the LST of its corresponding land cover type. In addition, the viewing angle effect on LST also depends on other factors such as surface slope, type and structure, and angular distribution of shadows, all of which are difficult to fully account for and quantify during the LST retrieval. Constraining the viewing angle turned out to be a key process for the evaluation of S-Noah in this study, and the cost of doing this is that fewer LST data are available for use. On average, about 10% data is left for MOD11A1 and 5% for MYD11A1 after screening based on these two criteria.

The last issue to consider in the screening process is the impact of mixed surfaces within the 1-km×1-km pixels on LSTs. Each 1-km×1-km LST is retrieved by assuming the pixel is homogeneously covered with its dominant land cover type (determined by LC-1 data) and using a pre-known emissivity specific to that land cover type. In reality, pixels are usually covered with multiple land cover types (Figure 3.1c). As a result, the measured radiance is not actually emitted by the dominant land cover alone. Similarly, actual surface emissivity may also differ from the pre-known value specific to the dominant land cover type. Therefore, the retrieved LST may not represent true LST of its dominant land cover type as expected. When the surface is mixed with different types of vegetation, the impact of mixed surface on LST usually tends to be small. This is because

for vegetated surfaces, the differences in emitted radiance and emissivity are usually small, so that their difference in LST is usually comparable to the retrieval uncertainty itself [110, 113]. However, when surface is mixed with both urban and vegetation, the impact of mixed surface on LST can be large due to their significant differences in the emitted radiance and emissivity. For example, the emissivity values for agriculture, broad leaf forest and urban are 0.983, 0.981 and 0.970 respectively in MODIS band 31. A significant impact on LST resulting from mixing of urban and vegetation is later supported by the results in section 3.3.3. Therefore, in the last step of the screening process, the 1-km×1-km LST data was filtered according to the urban fraction within the pixel (as illustrated in Figure 3.1c).

The urban fraction of each 1-km×1-km LST pixel was obtained by regriding the 30-m resolution land use/land cover data from National Land Cover Database 2001 (NLCD2001) [114] to 1-km×1-km grid cells exactly overlapping the LST pixels. This urban fraction data is termed as LandCover-Data2 (or LC-2). In this last screening step, an urban pixel (determined by LC-1) is valid with urban fraction (determined by LC-2) above 95%; and a vegetated pixel is valid with urban fraction below 5% for. This criterion of urban fraction for LST pixels is termed the "strong urban fraction limit".

In summary, MODIS LST with 1-km×1-km resolution was screened based on its quality flag, viewing angle, and urban fraction within the pixel. LSTs that passed the screening process are regarded as valid data for evaluating subgrid T_{SK} modeled by S-Noah.

3.3.2 Evaluation of S-Noah at the Sub-Grid Level for A Single Land Cover

The variability in subgrid T_{SK} of urban and agricultural surfaces is investigated in this section, respectively. For each 4-km×4-km WRF grid cell, valid 1-km×1-km LSTs for urban surface (referred to as LST-u; or agriculture, referred to as LST-a) were obtained, if there are any, following the screening criteria discussed in section 3.3.1. If more than one

valid LST of urban surface (or agriculture) are available within a 4-km×4-km WRF grid cell, the average is used (Figure 3.1b) for the later comparison with the subgrid T_{SK} of urban (or agriculture) modeled by S-Noah. Agricultural surface is chosen to demonstrate the performance of S-Noah on vegetated surfaces, because agriculture is the most abundant vegetated land cover type in domain d02. In addition, difference in LSTs between vegetated surfaces tends to be so small that the difference is usually comparable to the retrieval uncertainty in LST.

3.3.2.1 Results

Subgrid T_{SK} over three simulation periods is compared with MOD11A1 LST at each crossing time (local time; Figure 3.4). Results comparing with MYD11A1 are similar and not shown. In general, simulated subgrid T_{SK} from S-Noah correlates well with the LST, with higher correlation during night than daytime for both urban and agricultural surfaces. This is in part because the uncertainty of LST decreases during night [115, 116].

For agricultural surface, daytime correlation is worse than that of nighttime, with the subgrid T_{SK} (referred to as $T_{SK\text{-}a}$) shifting more towards higher values. This may result from the bias in soil moisture during the simulation. A study [117] showed that T_{SK} responds non-monotonically to the bias of soil moisture, especially for heavily vegetated surface. With a wet bias in soil moisture, Noah LSM was showed to be still able to reproduce canopy evapotranspiration reasonably, which suggests that the modeled T_{SK} is still adequately represented; while with a dry bias in soil moisture, the canopy evapotranspiration can be dramatically under-estimated, which leads to a significant over-estimate of T_{SK} [117]. It was also found that the impact of soil moisture on T_{SK} was much stronger during the day than the night, which is consistent with what is found here (Figure 3.4c,d).

For urban surface, different from agricultural surface, nighttime subgrid T_{SK} (referred to as $T_{SK\text{-}u}$) (Figure 3.4b) is more overestimated compared with that of daytime

(Figure 3.4a), and compared with $T_{SK\text{-}a}$ of nighttime (Figure 3.4d) as well, indicating that the default emissivity assigned to the urban surface may be low and that the radiative cooling of urban surface could be underestimated. No further tests for the related parameters were conducted here since it is outside of the scope of this study, but it is of interest to investigate in future studies.

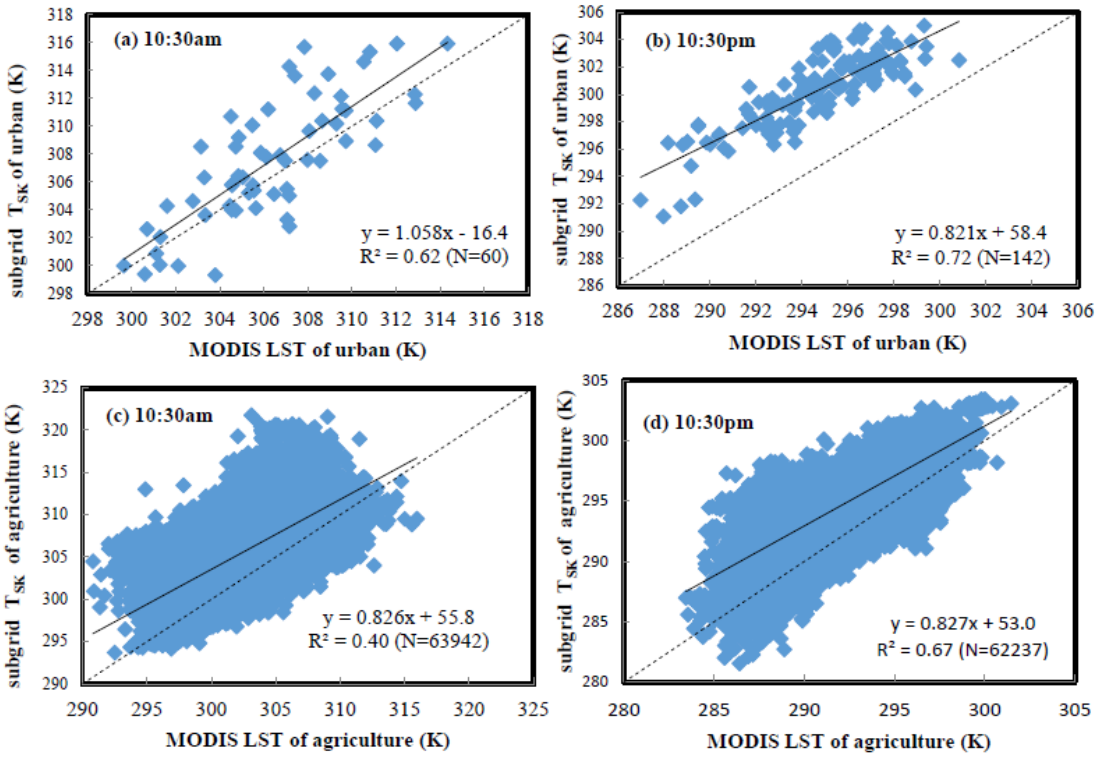

Figure 3.4 Scatter plots of MODIS LSTs vs. S-Noah subgrid T_{SK} at different crossing times for urban surface (a)(b) and for agricultural surface (c)(d). Solid line is the linear regression between the LSTs and T_{SK}, with N the number of data involved. Dashed line is the 1:1 line.

3.3.2.2 Discussion

Although the T_{SK} and LST at the subgrid level are close correlated (Figure 3.4), another reason could lie behind the high correlation, which is the changes in meteorological

conditions (e.g. radiation intensity), instead of the capability of S-Noah. In addition, the scatter of subgrid T_{SK} is wide. For example, at a given LST for agriculture during the daytime (Figure 3.4c), the subgrid T_{SK} varies more than 10 K. Therefore, a question arises as to whether or not the S-Noah approach overestimates the variability of the subgrid T_{SK}. To answer this question, ideally, for each 4-km×4-km WRF grid cell, its grid-level LST (and T_{SK}) should be subtracted from LST (and subgrid T_{SK}) of agriculture before the correlation between the subgrid T_{SK} and LST is examined. Grid-level T_{SK} is a standard output by S-Noah (Eq.2). However, it is difficult to obtain the grid-level LST, due to the limited availability of valid 1-km×1-km LST pixels within a WRF grid cell (Figure 3.1b). Through the three summers simulated in this study, less than 10 records were found that valid LSTs exist for all 16 LST pixels within a WRF grid cell.

Given the difficulty in obtaining grid-level LSTs, the variability of subgrid T_{SK} is therefore investigated in terms of the correlation between $T_{SK\text{-}u}$ and $T_{SK\text{-}a}$ at the subgrid level, and then compared with the correlation between LST-u and LST-a at the subgrid level. The correlation between $T_{SK\text{-}u}$ and $T_{SK\text{-}a}$ directly demonstrates the ability of S-Noah in predicting variability at subgrid level. Following the screening process as described in section 3.3.1, few records were found to have valid LST-u and LST-a at the same time (Figure 3.1b). This is because based on the criteria of "strong urban fraction limit" it is very rare to have the pixels with such pure urban and agricultural land covers co-exist within the same WRF grid cell. Therefore, with no other change in the screening process, the "strong urban fraction limit" was replaced by "medium urban fraction limit", in which the urban fraction must be over 80% for urban pixels and less than 20% for agriculture pixels.

The results show that at subgrid level, LST-u and LST-a are highly correlated (Table 3.1), with stronger correlation during nighttime. The standard error of regression (SD) reflects the variability in LST at subgrid level due to the subgrid heterogeneity in land surface, which is about 1.5K during daytime and 0.5K during nighttime. Similar

correlation was built between T_{SK-u} and T_{SK-a} at subgrid level as well (Table 3.1). Results show that S-Noah is able to reproduce the high correlation at subgrid level. As to the standard error of regression, in general, S-Noah provides stronger subgrid variability than T_{SK} with SD of about 2K. However, such variability in T_{SK} at subgrid level is much smaller than the scatter range found for subgrid T_{SK-a} (Figure 3.4c). The results indicate that S-Noah approach is able to provide reasonable subgrid variability in T_{SK}, and the wide scatter range (Figure 3.4c) is mainly due to the bias in fields/forcing at scale of 4-km and larger, instead of S-Noah approach per se.

Table 3.1 Linear regression of the temperatures between agricultural and urban surfaces at the subgrid level, using the land surface temperatures (LSTs) derived from MODIS, and using the subgrid skin temperature (T_{SK}) from S-Noah, respectively, with the number of data points in the S-Noah cases equal to or less than those in MODIS cases, because grids with clouds are excluded for the data in S-Noah cases. Results are in bold if they are significant at 95% confidence interval.

Local time	Data source	Regression slope	Regression intercept	R^2	Standard error of regression (K)	Number of data points
10:30am	MODIS	**0.904**	**27.1**	**0.85**	1.57	211
	S-Noah	**0.855**	**40.1**	**0.89**	1.57	186
1:30pm	MODIS	**1.009**	**-5.7**	**0.89**	1.35	34
	S-Noah	**0.780**	**61.4**	**0.77**	2.03	26
10:30pm	MODIS	**0.965**	**9.2**	**0.93**	0.55	123
	S-Noah	**0.879**	**30.7**	**0.75**	2.05	99
1:30am	MODIS	**0.977**	**5.9**	**0.98**	0.34	175
	S-Noah	**0.982**	**0.8**	**0.90**	1.52	167

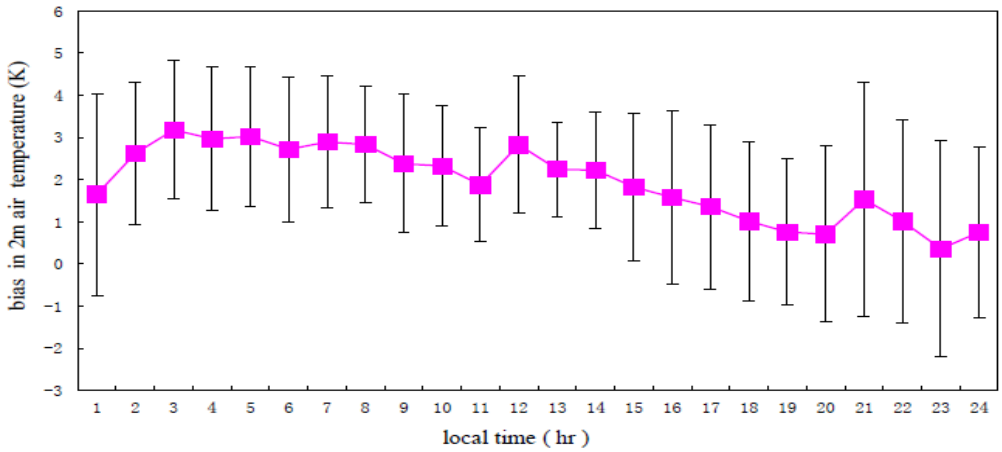

Figure 3.5 The diurnal cycle of the bias (and standard deviation) in 2m air temperature, when comparing the WRF results with observations available over the simulation domain d02 for summers 2003-2005.

To further confirm the reason for the wide scatter range found in subgrid $T_{SK\text{-}a}$ (Figure 3.4c), the modeled bias in meteorology at the grid level is investigated. WRF modeled 2-m air temperature is compared with observations (from TDL U.S. and Canada Surface Hourly Observations, available online at http://rda.ucar.edu/datasets/ds472.0). With about 30 observational sites available over domain d02, the 3-summer averaged mean bias and root mean square of error (RMSE) is plotted in terms of the diurnal cycle (Figure 3.5). The WRF control run gave similar results to S-Noah (not shown here), indicating that the bias in grid-level 2m air temperature is not related to the implementation of S-Noah. The comparison with observations shows that the 2m air temperature tends to be overestimated by about 2K in both bias and RMSE. In addition, larger bias shows up during the daytime than nighttime. Despite the relationship between LST and the 2m air temperatures not being clear [118], the result (Figure 3.5) still suggests that the wide range scattering of subgrid $T_{SK\text{-}a}$ (Figure 3.4c) may be mostly attributed to the modeled bias in atmospheric fields at scales of 4-km and larger.

Another appropriate question to raise here is whether or not the performance of S-Noah in subgrid T_{SK} depends on the extent of surface homogeneity of WRF grid cells, namely the extent that a WRF grid cell is covered by a single land cover type. In S-Noah, each surface land use element interacts with the atmosphere independently. In reality, however, subgrid surface heterogeneity may induce advection at both meso- and micro-scales, which may make the subgrid heat fluxes different from that estimated from the grid's atmospheric conditions. For example, the advection of hot dry air from subgrid urban land uses can enhance the evaporation of the subgrid vegetated surfaces downwind. The meso- and micro scales circulations generated by different land use elements are not captured by S-Noah. Therefore, we are interested in whether the performance of S-Noah in subgrid T_{SK-a} (or T_{SK-u}) depends on the fraction of agricultural (or urban) surface within a WRF grid cell. If not, it suggests that the S-Noah concept is reasonable at the tested scale. Owing to the limited number of data for the urban surface, only the case of agricultural surface is analyzed here. Two extreme situations in the coverage of agricultural surface are investigated. In one situation the 4-km×4-km WRF grid cell is sparsely covered by agriculture (less than 10%), and in the other situation the grid cell is almost fully covered by agriculture (over 99%). The subgrid T_{SK-a} is then correlated with the LST-a from the same WRF grid cell. The results (Table 3.2) clearly show that the modeling performance has little to do with the surface homogeneity of 4-km×4-km WRF grid cells.

S-Noah may not be applicable to RCMs when the grid spacing is either too coarse or too fine. Other studies have suggested that meso-scale circulations begin to be induced by land surface contrasts with a spatial extent of 5-10 km [119, 120]. Meanwhile, when the grid spacing is too fine (e.g. a couple of hundred meters), there may be not enough distance to dampen the impact of micro-meteorological features generated by the neighboring surface patches [121].

Table 3.2 Linear regression between the S-Noah subgrid skin temperature (T_{SK}) and the MODIS-derived land surface temperatures (LSTs) for the land cover type of agriculture, with data grouped according to the agriculture fraction within the WRF grid cells of 4-km resolution. Results are in bold if they are significant at 95% confidence interval.

Local Time	Agriculture fraction	Regression slope	Regression intercept	R^2	Number of data points
10:30am	<10%	**0.873**	**41.2**	**0.43**	4289
	>99%	**0.707**	**92.3**	**0.28**	4938
1:30pm	<10%	**0.745**	**80.8**	**0.39**	2333
	>99%	**0.435**	**176.4**	**0.17**	2890
10:30pm	<10%	**0.832**	**51.1**	**0.67**	3984
	>99%	**0.826**	**53.7**	**0.66**	5327
1:30am	<10%	**0.929**	**22.0**	**0.87**	2627
	>99%	**1.020**	**-4.7**	**0.89**	3330

3.3.3 Evaluation of S-Noah at the Sub-Grid Level for the Urban-Agriculture Contrast

In section 3.3.2.2, the correlation between T_{SK-u} and T_{SK-a} at subgrid level was investigated (Table 3.1). This section will focus on the contrast/difference between the T_{SK-u} and T_{SK-a} at subgrid level. The difference in LST between urban and agriculture surfaces within the same 4-km×4-km WRF grid cell is referred to as "subgrid LST contrast" hereafter. Similar to what happened in section 3.3.2.2, at each crossing time of Aqua and Terra, a very limited number of valid records for the "subgrid LST contrast" are found through all the simulated summers if the "strong urban fraction limit" is applied to the screening process, because it is very rare to have 1-km×1-km pixels of both urban and agricultural surfaces within the same 4-km×4-km WRF grid cell. To increase the number of data, "strong urban fraction limit" was removed from the screening process, with all other screening criteria unchanged (referred to as "no urban fraction limit" case). As a result, the obtained "subgrid LST contrast" reflects the subgrid-level LST contrast between urban and agriculture surfaces with impacts of surface mixing below the 1-

km×1-km LST resolution (Figure 3.1c). Therefore, the "subgrid LST contrast" is not directly comparable to the difference between $T_{SK\text{-}u}$ and $T_{SK\text{-}a}$, because modeled subgrid T_{SK} is a property of pure surface. This hurdle is overcome by estimating the T_{SK} of mixed surfaces from the T_{SK} of pure surfaces. In other words, subgrid-level T_{SK} contrast between urban and agriculture with mixed surfaces (referred to as "subgrid T_{SK} contrast") is estimated from $T_{SK\text{-}a}$, $T_{SK\text{-}u}$ and the urban fractions of 1-km×1-km pixels used to obtain the "subgrid LST contrast". Thus, the "subgrid T_{SK} contrast" can be compared with the "subgrid LST contrast".

3.3.3.1 Results

The cumulative probability of "subgrid T_{SK} contrast" is built and compared against with "subgrid LST contrast" for the "no urban fraction limit" case at each crossing time. Results show that in general the "subgrid T_{SK} contrast" by S-Noah (thin dash line in black in Figure 3.6) is able to capture the "subgrid LST contrast" (thick dash line in black in Figure 3.6), although with a narrower distribution, especially during the day (Figure 3.6a,c). This is because for each data point in the "subgrid T_{SK} contrast" distribution, the T_{SK} for mixed urban and mixed agriculture surfaces are generated from the same subgrid T_{SK} of pure surfaces (namely $T_{SK\text{-}a}$ and $T_{SK\text{-}u}$).

The results also show that the subgrid contrast between mixed surfaces from subgrid T_{SK} is usually smaller than that by LSTs. One reason is that the surface emissivity for LST retrieval is not corrected for the effect of mixing surface. For example, there are two LST pixels with similar fractions of urban and vegetated surfaces within the pixels, but one pixel is slightly dominated by urban surface (e.g. 51%) and the other by vegetated surface. The two pixels are supposed to have similar LSTs, and similar T_{SK} calculated from the $T_{SK\text{-}a}$, $T_{SK\text{-}u}$ and the urban fractions. However, during the retrieval of LST, a lower emissivity is used for the urban dominated pixel compared with emissivity used for

vegetation dominated surface. As a result, the LSTs tend to provide a slightly larger urban-agricultural contrast of the mixed surfaces.

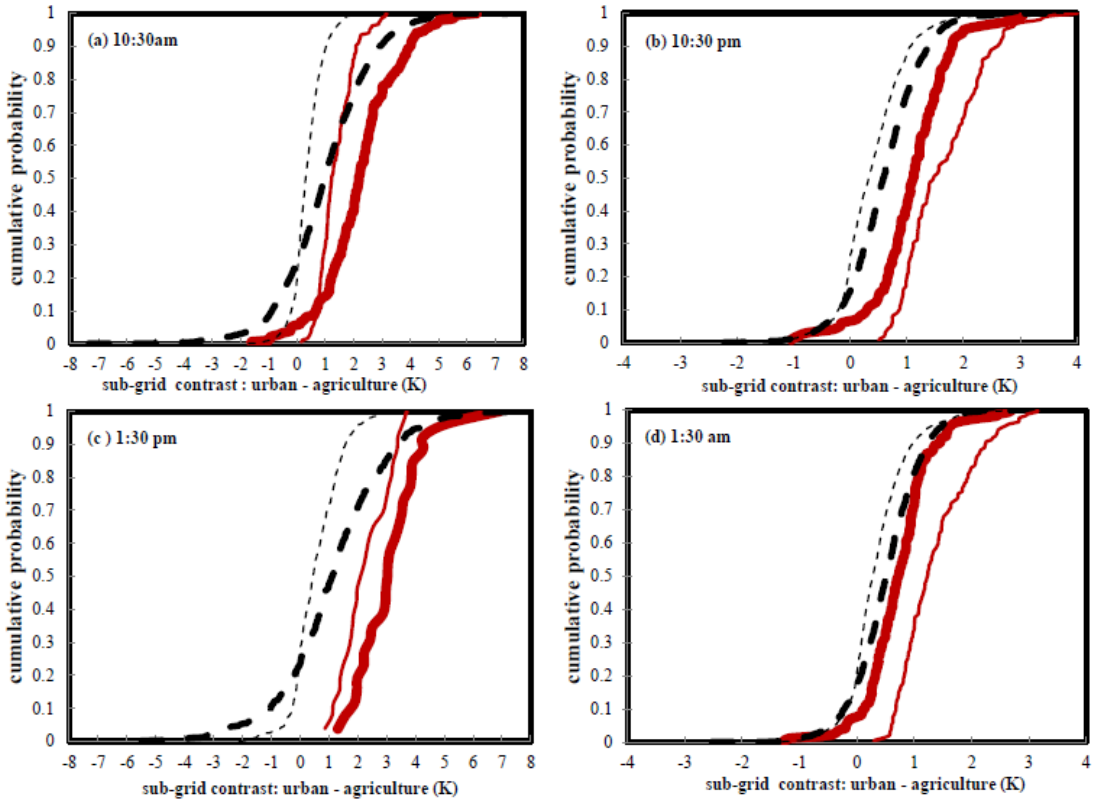

Figure 3.6 Cumulative probability distributions of the "subgrid LST contrast" (thick lines) and the "subgrid T_{SK} contrast" (thin lines) between urban and agricultural surfaces at different crossing time. The "subgrid LST contrast" is calculated from the differences between LST-u and LST-a at the subgrid level of WRF grid cells with 4-km resolution. Two cases are shown, in which different criteria regarding the urban fraction within the LST pixels are used during the screening process of LSTs as described in section 3.3.1, with "no urban fraction limit" case in thick dash line, and "medium urban fraction limit" case in thick solid line. In each case, the corresponding "subgrid T_{SK} contrast" (thin dash line for "no urban fraction limit" case and thin solid line for "medium urban fraction limit" case) is calculated using the T_{SK-a}, T_{SK-u} from S-Noah, and the urban fractions within the valid LST pixels, which are used to calculate the "subgrid LST contrast".

In addition to the “no urban fraction limit” case, the “medium urban fraction limit” case was also examined (solid lines in red in Figure 3.6), with case description detailed before. Results similar to “no urban fraction limit” case are found during the daytime. During the night (Figure 3.6 b d), stronger “subgrid TSK contrast” is obtained by S-Noah in “medium urban fraction limit” case, which is due to the overestimate of $T_{SK\text{-}u}$ during the night as found before (Figure 3.4b).

3.3.3.2 Discussion

Although LST has been utilized in many studies to investigate urban heat island (UHI) effect (termed as surface urban heat island (SUHI) [122] to distinguish the UHI defined by air temperature), SUHI has usually been quantified as the LST difference between an urban core and a surrounding buffer zone. However, limited research [123] has been conducted to investigate the SUHI at very fine or local scale, which is the subgrid level interested in this study. Therefore, a careful look is taken in this section at the “subgrid LST contrast” at a scale as fine as 4km and below.

The cumulative probability of “subgrid LST contrast” for the “no urban fraction limit” case was first examined with the number of qualified records listed (black dash line in Figure 3.7, which is the same as thick dash line in Figure 3.6). The results show that the local SUHI effect, on average, can still be seen at the fine scales, with mean temperature differences of 0.98±1.55K, 1.14±1.80K, 0.58±0.63K and 0.52±0.59K at 10:30am, 1:30pm, 10:30pm and 1:30am local time, respectively. This diurnal trend is consistent with the findings by other study [124], which showed that the LST difference between Paris and its rural area starts to show up after sunrise and grows quickly, culminates about 1h after the noon, and lasts through the night and may drop fast before sunrise. Other studies [125, 126] also observed that SUHI reached its peak during daytime, which is different from the diurnal variability of UHI from air temperature with

maximum UHI usually at night. Although on average, the "subgrid LST contrast" of urban-agriculture is evident in "no urban fraction limit" case, there is a large fraction of records (about 20%) with negative values, which is opposite to the expected SUHI effect. If the negative urban-agricultural contrast, known as urban heat sink (UHS) [126-129], occurs in reality at such local scales, it is interesting and important for the evaluation of S-Noah. Therefore, we further focus on identifying reasons behind the negative "subgrid LST contrast" between urban and agricultural surfaces.

The retrieval uncertainty of LST is considered first. Research showed that the uncertainty in MOD11A1/MYD11A1 LSTs is around 2-3K in bare soil regions, and 1 K for other land cover types [110, 130]. However, in the "no urban fraction limit" case, there are negative values (about 5-10%) much larger than LST uncertainty, especially during the daytime. Hence, the negative urban-agricultural contrast cannot be attributed to retrieval uncertainty alone.

Another hypothesis is that the long tail on the negative side of the distribution (dash lines in Figure 3.7) is related to surface mixing below the 1-km×1-km LST pixel scale (Figure 3.1c). As mentioned in section 3.3.1, when the land surface is mixed with different land cover types, radiance measured by sensors is not emitted by the dominant land cover alone. When the mixed surface contains mainly urban and vegetation, emitted radiance by a mixed surface and by a homogeneous surface can be significantly different, so that retrieved LST is affected and the urban-agriculture contrast even flips its sign from positive to negative. For example, for a LST pixel of urban mixed with vegetation (Figure 3.1c), the retrieved LST is lower than that of a pure urban pixel during the day, because the vegetation surfaces are usually cooler than urban surface and thus emit less radiance. Likewise, for a LST pixel of agriculture mixed with urban, the retrieved LST is higher than that of a pure agriculture pixel. To test this hypothesis, two more cases with different "urban fraction limits" were examined, with "no urban fraction limits" replaced by stricter constraints during the screening process. One case is "low urban fraction

limit," in which the urban fraction (based on LC-2) must be over 50% for urban pixels and less than 50% for agricultural pixels. The other is the "medium urban fraction limit" case, in which the urban fraction must be over 80% for urban pixels and less than 20% for agricultural pixels. As constraints on urban fraction become stricter, the long tail on the negative side of the distribution is significantly shortened or removed (Figure 3.7). It is expected that the distributions of "subgrid LST contrast" would move further towards the positive side as the impact of mixing surface is further ameliorated by more stringent constraints on urban fraction. However, as constraints become stricter, less data is available after the screening process. When "strong urban fraction limits" is applied, the number of valid records is too limited to build distribution. When the "medium urban fraction limit" applied, negative sides of the distributions still exist. However, given the retrieval uncertainties of LSTs and lack of other observational data, it is impossible to further identify if the urban heat sink happens at the scale of interest.

The results (Figure 3.7) indicate that, for 1-km×1-km MODIS LSTs, surface mixing below the resolution of the LST pixels must be taken into account when comparing the "subgrid LST contrast" at fine scales with the modeled subgrid T_{SK}. As reported [131], MODIS allows for the synoptic overview of the urban thermal environment, and ASTER (Advanced Spaceborne Thermal Emission and Reflection Radiometer, with a spatial resolution of 90 m) allows for a more accurate determination of LST for urban LULC types. However, even using LST data with higher spatial resolutions, mixing surfaces within LST pixels are always inevitable in the real world.

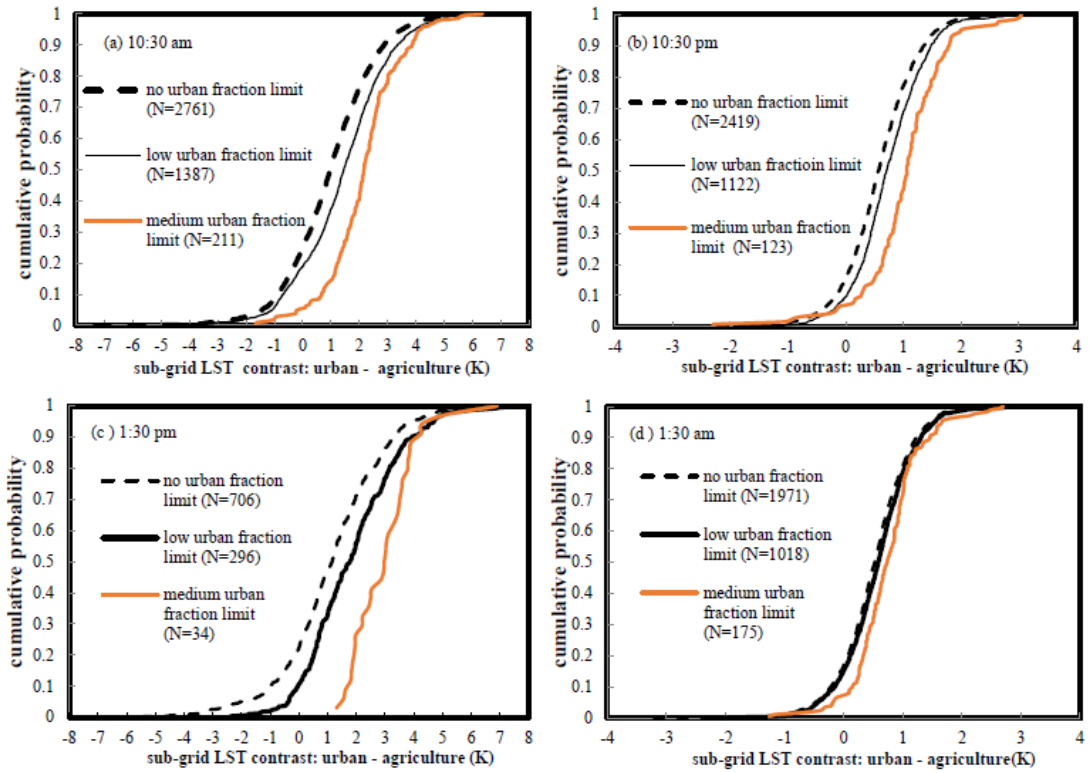

Figure 3.7 Cumulative probability distributions of the "subgrid LST contrast" between urban and agricultural surfaces (namely the local surface urban heat island (SUHI) effect) at different crossing times, when different urban fraction limits are used to filter the 1-km resolution MODIS LST data. For "low urban fraction limit", the urban fraction must be over 50% for urban pixels and less than 50% for agriculture pixels. For "medium urban fraction limit", the urban fraction must be over 80% for urban pixels and less than 20% for agriculture pixels. For "no urban fraction limit", there is no constrains on the urban fraction for urban and agriculture pixels.

3.4 Conclusions

In this chapter, an effective subgrid approach based on Noah LSM, called S-Noah, was developed. S-Noah predicts subgrid-scale surface properties specific to land cover tiles within the parent simulation grid cell and aggregates subgrid properties to grid level. S-

Noah was tested using WRF with a spatial resolution of 4-km. To evaluate S-Noah, the performance of S-Noah at the subgrid level was focused on, which is important but rarely studied due to lack of observations, because observations available are usually too sparse in space or time to provide sufficient coverage at subgrid level of the spatial resolutions typically used in regional climate models. The unique contribution of this study is that the surface skin temperature, which is an important surface property predicted by Noah (and S-Noah), was evaluated at the subgrid level (referred to as subgrid T_{SK}) by comparison with land surface temperatures (LSTs) derived from remote sensing. To our knowledge, this is the first effort to evaluate the modeled subgrid properties at such a fine scale against satellite observations.

A series of issues related to the LSTs data had to be addressed before a reasonable comparison between the T_{SK} and LST can be carried out at the subgrid scale. As pointed out, there are two issues of the most importance, namely the viewing angle and the mixing surface within LST pixels. The procedure for screening LSTs was built and successfully applied to the MODIS LST products.

Comparing LSTs with T_{SK} at subgrid level, it was shown that S-Noah successfully captured the urban-vegetation variability at subgrid level due to the heterogeneity in the land surface. S-Noah has been implemented in prior study [132], in which impacts of a variety of detailed and promising LULC scenarios on urban climate and heat-related health were studied across three U.S. cities (Atlanta (GA), Phoenix (AZ) and Philadelphia (PA)). S-Noah not only facilitates such studies, but also provides subgrid properties (e.g. T_{SK}), which can be directly applicable to health studies that use such quantity to assess human exposures to heat at scales finer than typical resolution of RCMs.

CHAPTER 4

INVESTIGATING A HEAT ADAPTATION STRATEGY FOR LOUISVILLE USING DYNAMIC DOWNSCALING AND S-NOAH[3]

As mentioned before, for dynamic downscaling, one of its important applications is the "regional climate simulation", in which atmospheric information from reanalyses is used to drive RCMs, and as the simulation goes, the regional initial conditions are forgotten. The simulated regional climate are generated from 1) the internal solutions of RCMs developed as a result of the combination of model physics and high-resolution surface information, such as land use/land cover, terrain, and etc.; and 2) the nudging terms applied to RCMs, if there is any. The "regional climate simulation" of dynamic downscaling has been widely used to study the impacts of local/regional forcings to regional climate. The land use/land cover (LULC), as one of the most important forcings to local/regional climate and air quality, is of particular interest and has been extensively investigated by studies, focusing on different regions/cities across the world.

[3] This chapter is based on the manuscript: Liu, P., Hu, Y., Stone, B., Nenes, A., and Russell, A.G. (2015), Assessing "white" surface mitigation strategy with high resolution numerical modeling—A case study involving the important issues of river temperature and cloud feedbacks (in preparation).

Though few studies have explicitly shown, the fundamental assumption of this kind of study using dynamic downscaling is that the LULC change only influences the climate at local/regional scales, but not at large scales. Therefore, the same atmospheric information used to drive the base case simulation in RCMs can still be used to provide boundary conditions (BC) and the nudging fields to RCMs. During this thesis work, it was found that this fundamental assumption is valid when the LULC change happens at the scale of a city.

In addition, in chapter 2, it was shown that the performance of dynamic downscaling can be improved by the implementation of spectral nudging, with appropriate nudging parameters used. In chapter 3, based on the existing Noah land surface model, S-Noah was developed to take into account the land surface heterogeneity at the sub-grid scale. All of work above gives the confidence in further investigating the problems in real world. In this chapter, a promising heat adaptation strategy, which involves LULC change specifically designed for the metropolitan area of Louisville (Kentucky, U.S.A), is explored using dynamic downscaling with spectral nudging and S-Noah.

4.1 Impact of Land Surface Change at the Urban Scale on Climate

Though not highlighted in this thesis, work was done during the research to obtain the projections of regional climate from GCMs by dynamic downscaling, and to investigate the impact of LULC change at urban scales on future climate. For example, the impact of LULC change in the Atlanta city area (State of Georgia, U.S.A) on climate at different scales was investigated. As mentioned, this work demonstrated the LULC change at urban scale had a very local influence on climate, with the influence mainly in the area where LULC change occurred.

WRF version 3.1.1 was used to downscale the climate projection in the year of 2050 obtained from a GCM by Goddard Institute for Space Studies (GISS). To investigate the impact LULC change in the Atlanta city area (State of Georgia, U.S.A) on climate at

different scales, a series of simulation domains with different spatial resolutions are included (Figure 4.1): the contiguous US with part of Canada and Mexico (with 36km resolution), the southeastern US (with 12km resolution) and the state of Georgia (with 4km resolution). During the simulation, spectral nudging was applied to the domains with 36km and 12km resolutions to maintain the climate patterns with scales larger than 2000km. Two-way nesting was also used in order to allow the potential feedbacks of the nested domains to its mother domain. In other word, if the impact of LULC change in Atlanta is able to develop into features with larger scales, and affect the climate of the southeastern U.S., or the whole U.S., a simulation with two-way nesting is necessary.

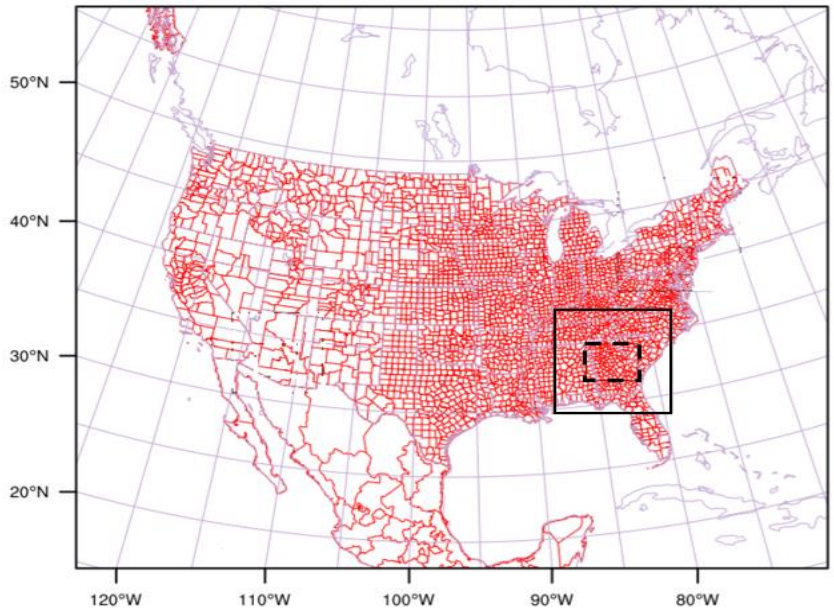

Figure 4.1 WRF simulation domains to investigate the impact of land use change at urban scale (Atlanta, Georgia, U.S.A) on climate at different scales. Three domains are included, with the outmost domain at a resolution of 36-km (the map is at the county-level for the U.S.A), the nested domain at a resolution of 12-km (as outlined in solid black line), and the nested domain at a resolution of 4-km (as outlined in dash black line) to cover the city of Atlanta.

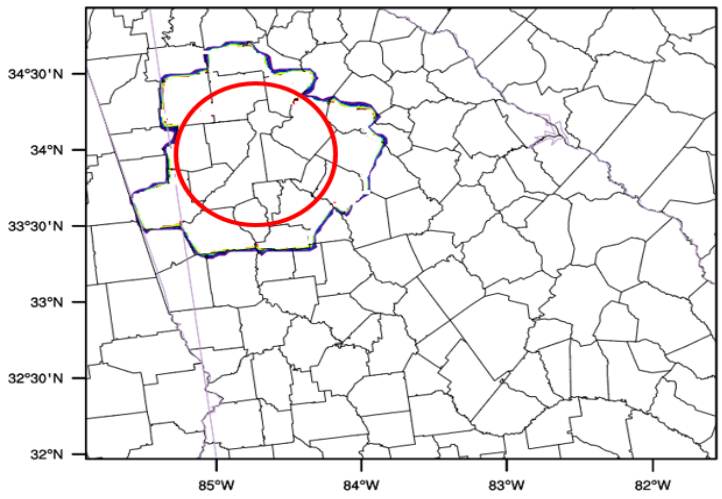

Figure 4.2 Zoom-in plot of the innermost simulation domain shown in Figure 4.1. The metropolitan area of Atlanta (GA, U.S.A) is outlined in blue line. The area within 30 miles of the center of Atlanta is outlined in red circle, and the circled area is covered by foreset in "base" case, and by asphalt in "impervious" case.

Two land use cases over the Atlanta city were investigated. For the "base" case, most of the urban area of Atlanta is covered with forest; while for the other case, termed as "impervious" case, all the urban area within 30 miles of the center of Atlanta (Figure 4.2) was replaced with asphalt. This choice was made to maximize the potential effects and scales of impact. To further make the two cases different as much as possible, a constant green vegetation fraction of 1.0 is assigned to the forest over the Atlanta; while 0.0 is assigned to the asphalt.

To test the significance of the impact of land use change, 5 ensemble members were generated for each land use case using different initial conditions. The summer-averaged (from May to September) air temperature at 2-m height was investigated, in terms of the difference between "impervious" and "base" case, because air temperature at 2-m height is essential to assess the heat-stress for human health. The results of student's t test found that the impact of land use change in Atlanta city had a very local impact (Figure 4.3). This finding indicates that the dynamic downscaling by RCMs, applied at continental and

regional scales, with BCs from the GCMs or re-analyses is an appropriate approach to investigate the impact of city-level LULC impact on its climate.

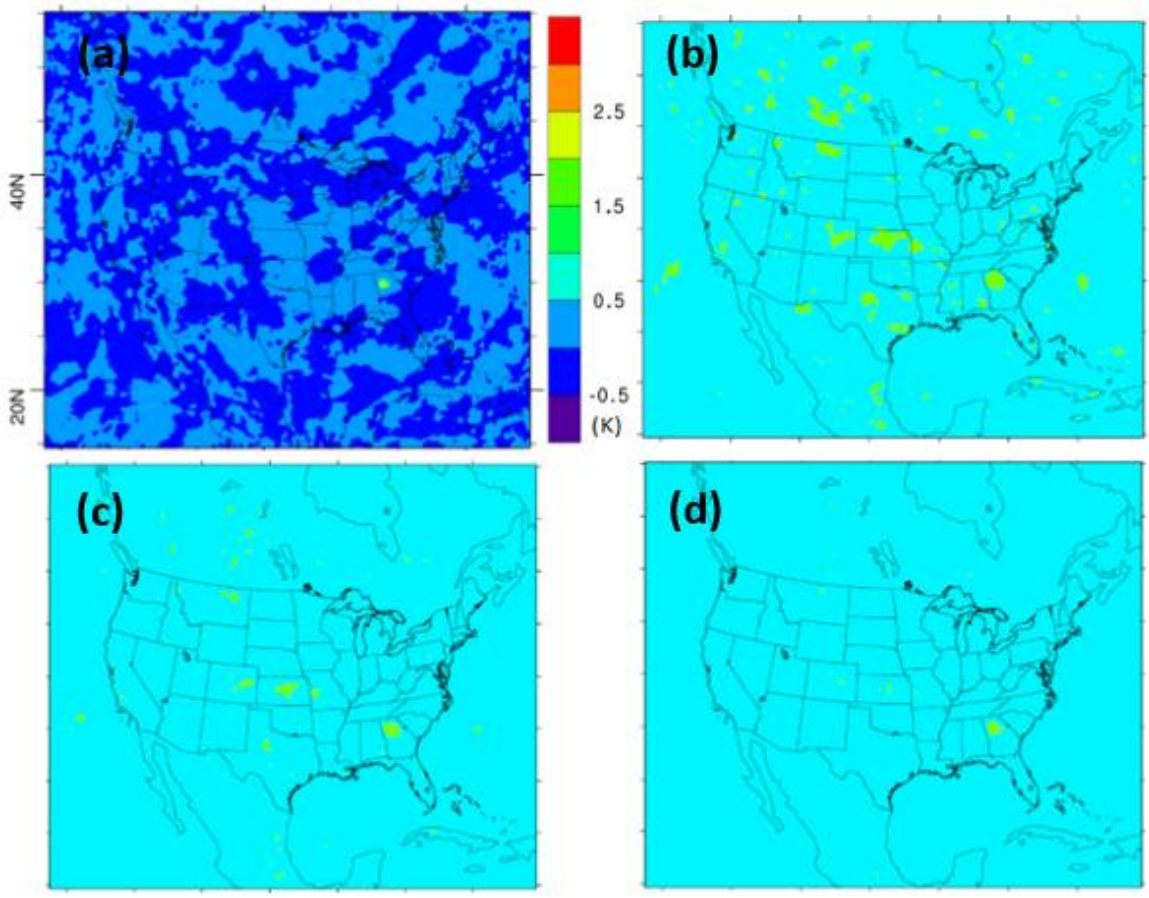

Figure 4.3 (a) The difference in summer-averaged (from May to September) air temperature at 2-m height between "impervious" and "base" case ("impervious" minus "base") simulated by WRF over the outmost domain. (b) Results of student's t-test based on the 5 ensemble members simulated in the "base" and "impervious" case respectively. Areas in yellow means the difference in summer-averaged (from May to September) air temperature at 2-m height is significant at the confidence interval of 95%; (c) same as (b) but with confidence interval of 99%; (d) same as (b) but with confidence interval of 99.9%.

4.2 Heat Stress and Adaptation Strategies for Urban Areas

Moderate or extreme heat may increase hospitalization rates [133, 134] and contribute to mortality [135-137]. The adverse impact of heat on human health has been receiving more attention, given that such threat is expected to grow significantly in the future due to the following reasons: 1) the "urban heat island" (UHI) effect may become stronger in the future due to the expansion of urban areas [138]; 2) urban populations will increase substantially; 3) climate change induced by greenhouse gases may impose extra heat stress on human health [139, 140], and heat waves are projected to become more intense, frequent, and longer as the average surface temperature increases [141-144]; and 4) urban and rural temperatures may respond unevenly to heat waves, with the former more vulnerable to heat extremes. For example, the added heat stress in cities can exceed the simple sum of the background UHI and heat wave effects [145].

While recognizing the serious heat-related health risks urban populations may experience in the future, adaptation strategies have been proposed to mitigate the UHI effect. During past decades, research has been conducted to assess the efficacy of different strategies, demonstrating that UHI can be ameliorated through judicious urban planning and design [132, 138, 146-149] and that heat-related mortality and premature mortality can also be decreased [132, 150, 151]. Among these mitigation strategies, "cool" or "white" surfaces, in which the albedo of impervious urban surfaces is increased by implementing high reflective materials, is considered promising, given the economic cost and the limited modifiable surface in urban environment. Potential mitigation in near-surface air temperature by reflective materials has been extensively investigated at different scales using numerical modeling, as reviewed previously [149]. Furthermore, some other aspects critical to urban environment may benefit as well from the surface whitening, such as building energy consumption and urban air quality [152].

In this chapter, a feasible surface whitening strategy is explored for the metropolitan area of Louisville (Kentucky, U.S.A), using the Weather Research and Forecasting Model (WRF) [27] version 3.6, with spectral nudging and S-Noah.

4.3 Simulation Design and Model Description

The complete dynamic downscaling process comprises of an outer domain (d01) with a grid spacing of 12 km, which is further downscaled to nested domains with resolution of 2.4 km (d02) and 480 m (d03) by one-way nesting (Figure 4.4a). Previous results in section 4.1 have demonstrated that the LULC change at such urban scale has little impact on the regional meteorological features. Therefore, the outmost domain covers the state of Kentucky and parts of its surrounding states, instead of covering the whole U.S., and one-way nesting is chosen.

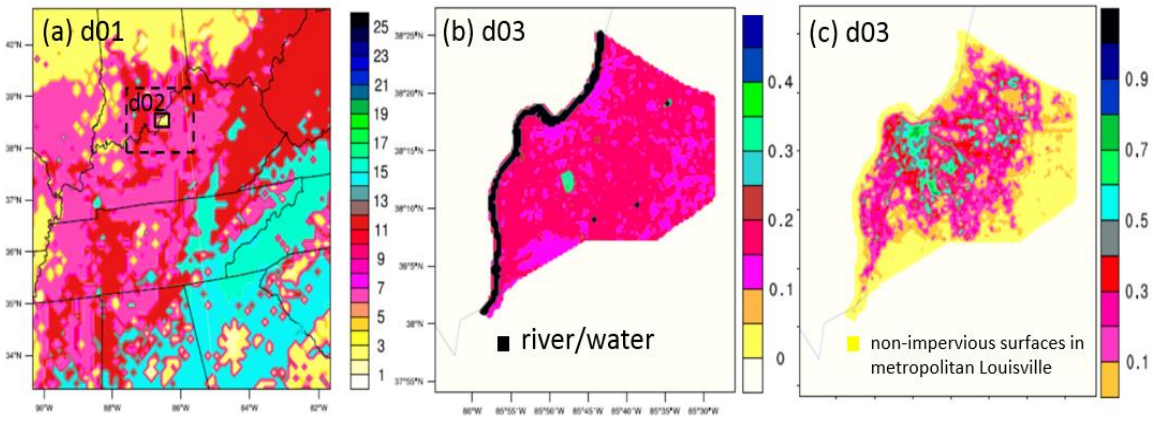

Figure 4.4 (a) WRF simulation domains for the case study of Louisville, Kentucky, U.S.A. The outmost domain (d01) covers the state of Kentucky and parts of its surrounding states, with a spatial resolution of 12-km. The nested domain (d02) is outlined by dash black line, with a resolution of 2.4-km. The innermost domain (d03) is outlined by solid black line, with a resolution of 480-m. The color contour represents the land use types based on USGS classification. (b) Zoom-in look of the most inner domain

d03 at the resolution of 480 m, with the color contour the surface albedo of the metropolitan area of Louisville (Kentucky, U.S.) in BASE case, and the Ohio River runs alongside the metro area. (c) the same as (b) but the total land use fraction of all five types of impervious surfaces in the metro area.

Meteorological initial and boundary conditions to drive the coarsest domain are from the North American Regional Reanalysis (NARR) product [67], with a spatial resolution of 32 km and temporal resolution of 3 hours. USGS land use classification is used for all domains. For the metropolitan area of Louisville (Figure 4.4b), the land use information was obtained at the parcel level and from national land cover dataset at 30m resolution, the resolution of which are much finer than the finest land use data available in WRF. For other area, the land use information was obtained from the data available in WRF. Furthermore, given that reflective materials with different albedo properties may apply to different urban surfaces, the impervious urban surfaces in the metro area (Figure 4.4c) were further divided into five categories (Figure 4.5), with their corresponding albedo properties listed in Table 4.1 for the BASE case and the mitigation case (referred to as ALBEDO case).

Table 4.1 Urban categories in metropolitan area of Louisville, KY, and their albedo values for BASE and ALBEDO cases.

	BASE	ALBEDO
Residence roofs	0.12	0.65
Non-residence roofs	0.12	0.88
Streets	0.12	0.44
Airports	0.44	0.44
Others	0.12	0.44

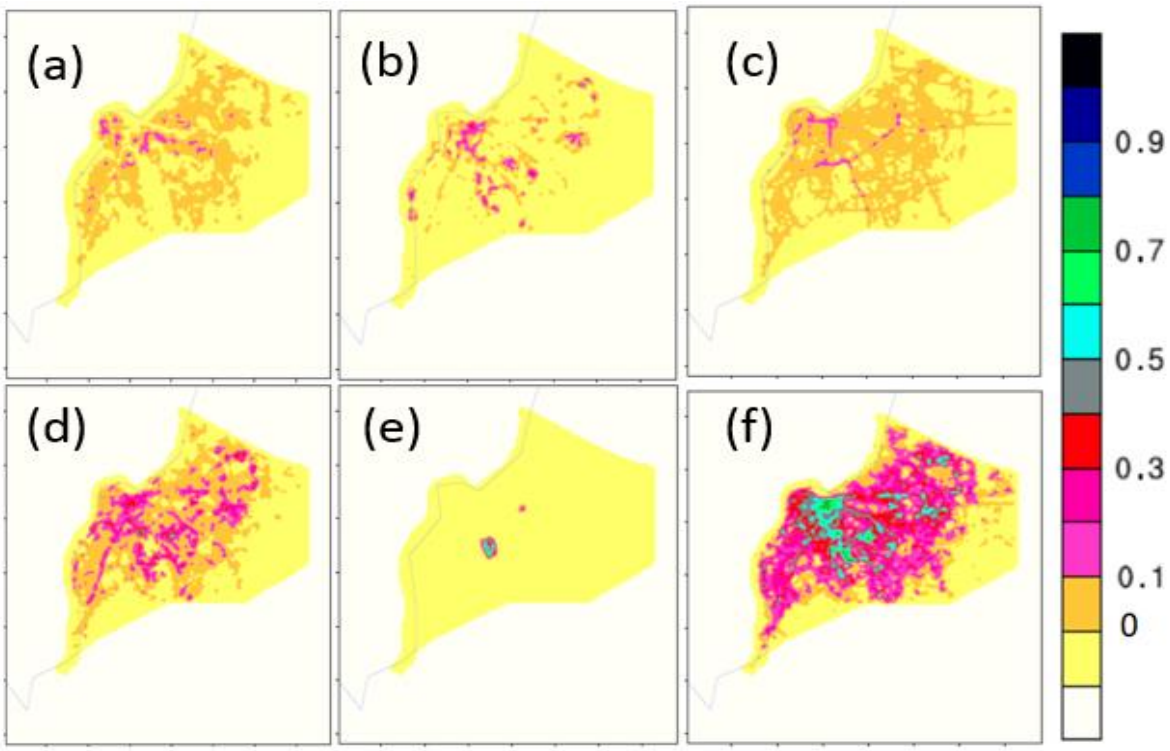

Figure 4.5 Land use fractions at horizontal resolution of 480m in WRF domain d03 for different urban impervious surfaces over the metropolitan area of Louisville: (a) residence roofs (b) non-residence roofs (c) streets (d) others (e) airports (f) the total of 5 impervious surfaces. The metropolitan area of Louisville, KY, U.S., is shaded in light yellow. When evaluating simulated surface properties in WRF, two meteorological stations are available in domain d03, which are located at the airports, as shown in (e).

With such a detailed land use information over the metro Louisville, the modifiable land cover patches are usually at the scale of a couple of hundred meters or less, suggesting that to represent the urban surface modifications at such fine scales, simulation using an ultra-high spatial resolutions (e.g. 50-100 m) is preferable to the typical resolutions used in regional climate models (e.g. 1-100 km). Further, ambient temperatures obtained at high resolutions (e.g. at census-tract level) can also be relevant

to health-related studies, particularly those examining the environmental justice issues. However, as to the numerical modeling, a variety of issues arise with ultra-high resolutions, including expensive computational costs, numerical instabilities, and the applicability of the parameterizations available in WRF. Here, a grid spacing of 480 m was chosen for the finest simulation domain for two reasons. First, coupling large-eddy simulation (LES) into WRF [153] found little improvement was gained regarding the fields related to hydrometeorology (e.g. surface latent and sensible heat fluxes, water vapor mixing ratio) when increasing horizontal resolution from 480 m to 50 m. Second, though land-cover at 480 m resolution is still highly mixed (Figure 4.5), the impact of heterogeneous surface can be taken into account by land surface models (LSM) with sub-grid schemes. In this study, S-Noah, which was developed and evaluated in the previous chapter, is applied. In addition, to deal with the 5 types of urban surfaces, the Single-Layer Urban Canopy Model (UCM) [154, 155] is coupled into the LSM.

The treatment of vertical mixing is closely related to horizontal resolution. Here, the first-order, non-local YSU scheme [156, 157] is chosen as planetary boundary layer (PBL) scheme owing to its performance in a recent comparative study [158]. In addition, given that our primary focus is to mitigate UHI effect during summer, and that convection in urban areas tends to be strong due to the high surface temperatures, a non-local scheme is preferred. If the horizontal resolution increases further (e.g. around 100m), the PBL scheme should be replaced by fully 3-dimension local turbulence schemes. Important parameters and physics schemes used for WRF simulation are summarized in Table 4.2.

Table 4.2 Important parameters and physical schemes used for WRF simulation.

	description
Period	June-August 2012 (with May as spinning-up)
Grid spacing	ΔX=ΔY=12 km (d01); 2.4 km (d02); 480 m (d03)
Number of grid points	X direction: 70 (d01); 70 (d02); 121 (d03)
	Y direction: 70 (d01); 70 (d02); 131 (d03)
Vertical levels	35 (model top at 100hpa)
Radiation scheme	RRTM (longwave); RRTMG (shortwave)
Surface layer and PBL scheme	Monin-Obukhov
	YSU
Cumulus scheme	Kain-Fritsch (off for d03)
Microphysics	Lin et al.
Urban physics	Single-layer Urban Canopy Model
Nudging	Spectral nudging above PBL (only for d01)

An interesting feature of the studied area is that the Ohio River runs alongside the metro Louisville (Figure 4.4b), and is expected to affect the ambient air temperatures nearby, which can be potentially important for populations along the river. However, the temperatures of in-land water bodies are usually not dealt with by the physics schemes in WRF. In other words, LSMs are not designed to deal with water surfaces. As a result, in WRF's default configuration, the water-surface-temperatures are provided by the driving data and interpolated to the simulation resolutions. In this study, the default river surface temperature was derived from NARR. It is found that the default river surface temperature has a diurnal variance as large as about 20 degrees, which is comparable to

the temperature variance of land surfaces but not reasonable for water surfaces. This is further confirmed by the measured temperatures of Ohio River (USGS Surface-Water Historical Instantaneous Data for Kentucky, U.S. Geological Survey, obtained from http://waterdata.usgs.gov/ky/nwis/uv) (Figure 4.6).

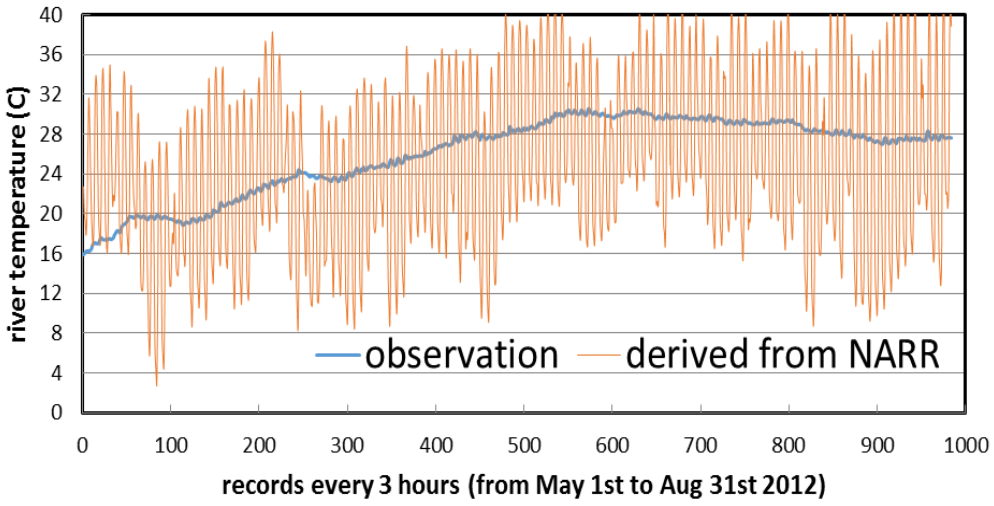

Figure 4.6 Time series of the temperature of the Ohio River at 3-hour interval through the simulation period by observation (black line) and from NARR (red line), respectively.

The unrealistic river temperature derived from NARR is due to the spatial resolution gap between NARR and our study. The 32 km resolution of NARR is still too coarse to capture the river, so that grid cells containing river surfaces are treated as land surfaces. A lake model [159] has recently been coupled into WRF to deal with in-land water bodies. However, the water-surface-temperatures from the lake models are mainly affected by solar radiation, soil under the water and the initial water temperature profile of the lakes, while the water-surface-temperatures of rivers are largely determined by upstream water temperatures. Therefore, in this study, measured water temperatures are used for the water-surface-temperature of the Ohio River, instead of temperatures from NARR or lake models. It turns out that using the measured water temperature can

produce reasonable 2m-air-temperature above the river, which has a significant impact on the surface air temperature of the metro area along the river, especially in terms of daily maximum and minimum temperatures.

Five ensembles are simulated for the BASE and ALBEDO case, respectively, generated by using different initial conditions. All results shown later in this chapter are the ensemble averages.

4.4 Results and Discussion

4.4.1 Results of the BASE Case

Given that surface air temperatures and wind speeds are commonly involved in assessing the heat stress in urban environments, the simulated 2m-air-temperature and 10m-wind-speed in BASE case are evaluated using TDL U.S. and Canada Surface Hourly Observations [160]. There are 160, 6, and 2 meteorological stations available within the simulation domains d01, d02, and d03, respectively. The two stations in d03 are located within the studied metropolitan area (Figure 4.5(e)). WRF performance is evaluated on a daily basis from June to August 2012 for each domain by comparing the average of observations and the average of WRF predictions from the grid cells where the stations are located. The comparison results for d01 are not shown, because d01 covers a large area and limited insight of model performance is obtained by comparing the domain-averaged results.

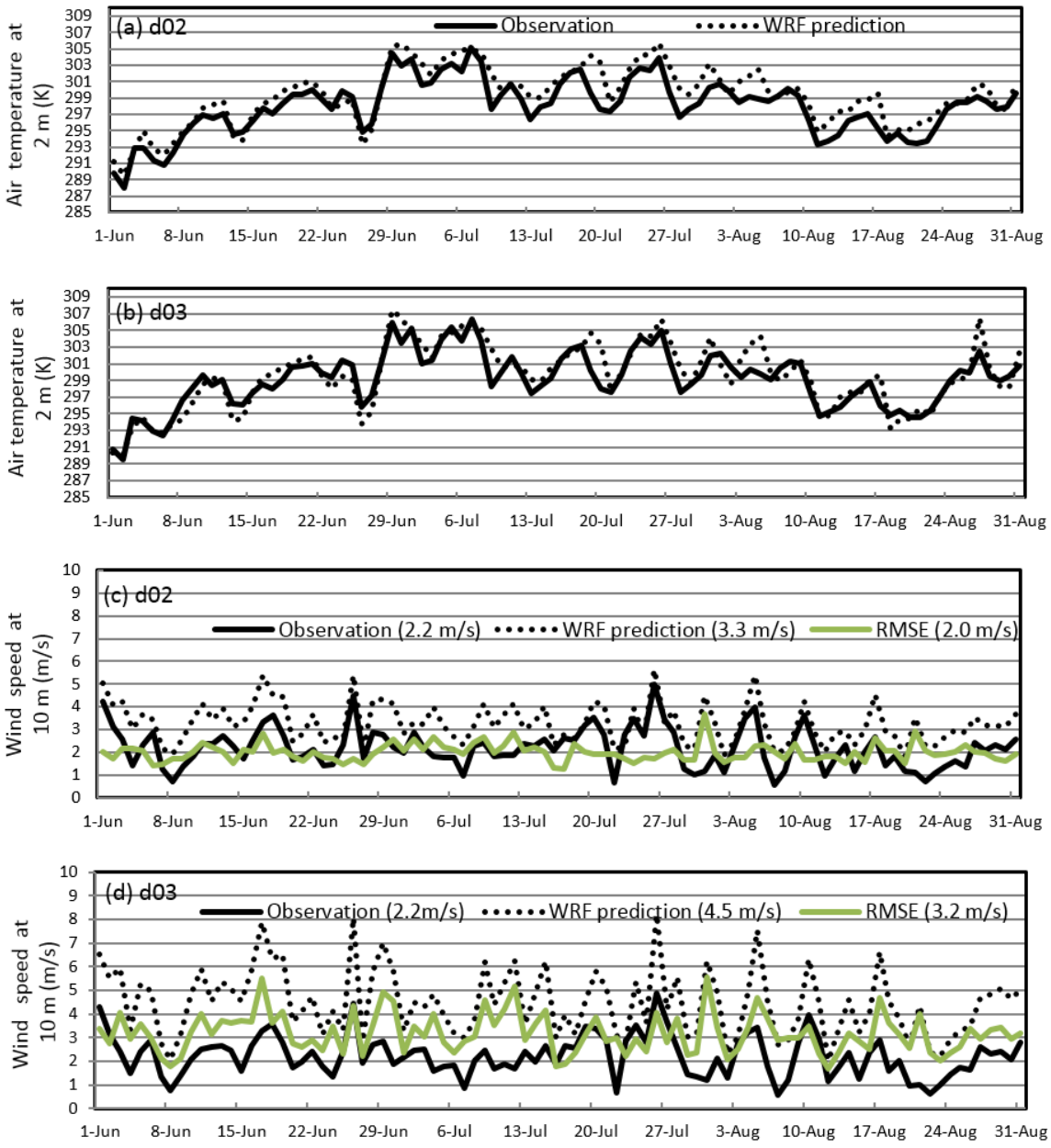

Figure 4.7 Evaluation of WRF performance on a daily basis by comparing with observations for (a) air temperature at 2-m height for domain d02; (b) same as (a) but for domain d03; (c) wind speed at 10-m height for domain d02, with number in parentheses the mean from June to August 2012; (d) same as (c) but for domain d03.

The surface temperature generally agrees well with the observations. The simulated surface wind speed, though strongly correlated with observations, is biased high. One

important reason for the over-estimation can be related to the driving fields, given that consistently higher surface wind exist in all simulation domains and that spectral nudging is applied above the PBL for domain d01. The discrepancy in surface wind profile between NARR and observations has been found before [161], where NARR is found to give higher near-surface winds (about 1-3 m/s) compared to observation by radiosonde. During the simulation, the bias is further enlarged when downscaling from domain d02 to d03, because some physics options (e.g. PBL scheme) become less appropriate when grid spacing decreases to sub-kilometer level. Similar root mean square error (RMSE) in the simulated 10m-wind-speed at sub-kilometer resolution has been reported by other studies [161] when comparing with observations, in which the local and 1.5-order Mellor–Yamada–Janjic (MYJ) PBL scheme [162, 163] was used for WRF.

In addition to the model performance in terms of domain average, the simulated surface properties along the Ohio River are also important, given the human activities near the river. When using water temperature from NARR, the contrast in 2m-air-temperature between river and its surrounding land does not make sense. The daily maximum 2m-air-temperature above the river is higher than its surrounding land surfaces (Figure 4.8a), while the daily minimum 2m-air-temperature above the river is lower than its surrounding land surfaces (Figure 4.8b). When using the observed river temperatures, however, reasonable contrast in 2m-air-temperature between river and its surrounding land is seen, with a significant cooling above the river for daily maximum temperature (Figure 4.8d) and a warming for the daily minimum (Figure 4.8e). The river temperature not only has a dramatic impact on the simulated air temperature directly above the river, but also on the air temperature in the metro area along the east side of the river, owing to the westerly wind during the summer (Figure 4.8c). As moving further to the east of the metro area, the impact of the river decreases rapidly. Hence, no significant difference is seen if only comparing WRF predictions with the two meteorological stations available in domain d03. Our study clearly showed that special carefulness should be paid when

rivers exist in the simulation domain. The ambient temperature change along the river due to different river temperatures is important when assessing human health related to heat stress and the interactions between potential land use change and the river.

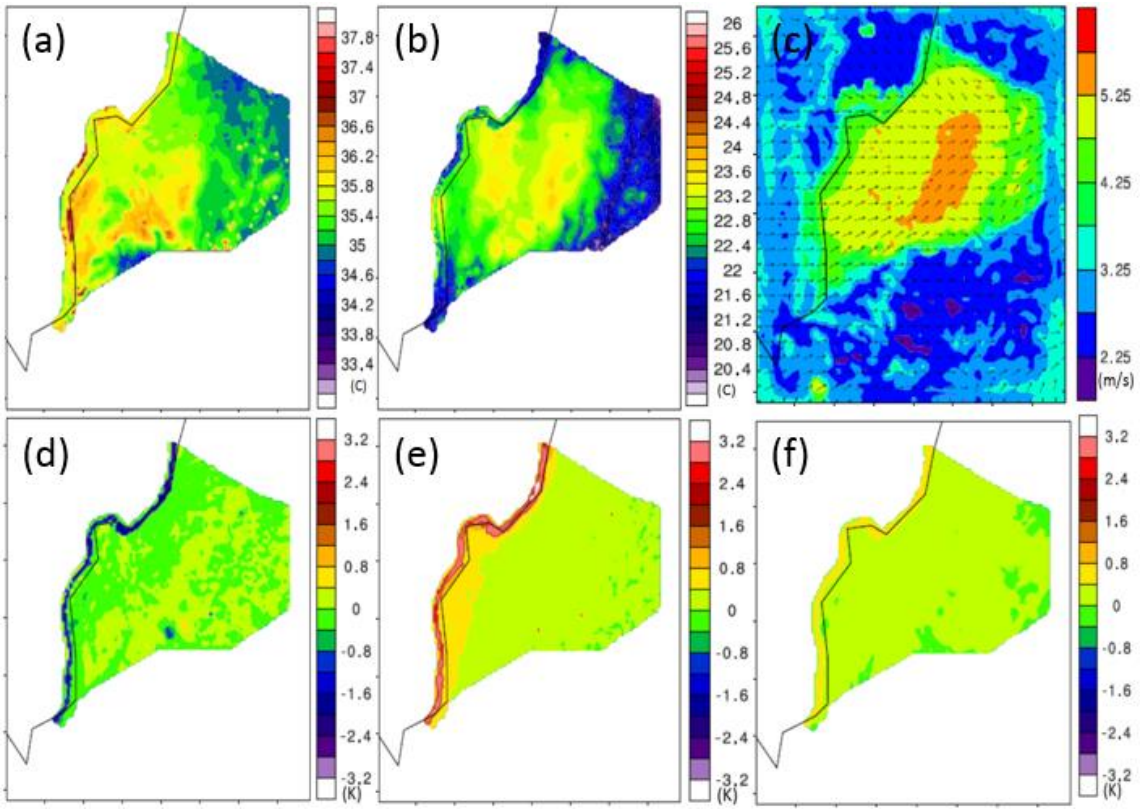

Figure 4.8 Average 2m-air-temperature over the metropolitan Louisville for the BASE case from June to August (a) daily maximum temperature when Ohio River temperature is derived from NARR; (b) same as (a) but for daily minimum temperature; (c) same as (a) but for wind at 10 m height; (d) difference in daily maximum temperature when observation and NARR are used to provide the Ohio River temperature as input to WRF respectively (using observation minus using NARR) ;(e) same as (d) but for daily minimum temperature; (f) same as (d) but for daily average temperature.

In general, the model performance for the BASE case is satisfying with the current WRF configuration, which gives us confidence in further investigating the mitigation efficacy of the ALBEDO case and the potential role cloud feedback may play.

4.4.2 Impact of the Mitigation Strategy on Urban Area

The mitigation efficacy in 2m-air-temperature of the surface whitening strategy is determined by the averaged difference from June to August between ALBEDO and BASE case in terms of daily minimum, maximum, and average temperatures (Figure 4.9(a)-(c)). The mitigation is most effective in modifying the daily maximum temperature, as expected. What is interesting is that the spatial pattern of mitigation efficacy in daily minimum temperature does not resemble the pattern in daily maximum temperature.

To further understand the relationship between the change in surface albedo and the mitigation efficacy for each 480m grid cell in the metro area, the grid-level albedo is calculated based on all land covers within the grid cell, and the grid-level surface albedo change between ALBEDO and BASE case is shown (Figure 4.9(d)). The results show that the mitigation in daily minimum temperature is consistent in space with the surface albedo changes, indicating that as to nighttime UHI, it is essential for the urban area to store less energy during the daytime, which is achieved by absorbing less shortwave radiation by surface whitening in the ALBEDO case. Conversely, the mitigation in daily maximum temperature does not follow the spatial patterns in albedo change. Stronger cooling effects show up in the south and middle of the metropolitan area where the change in albedo is relatively small.

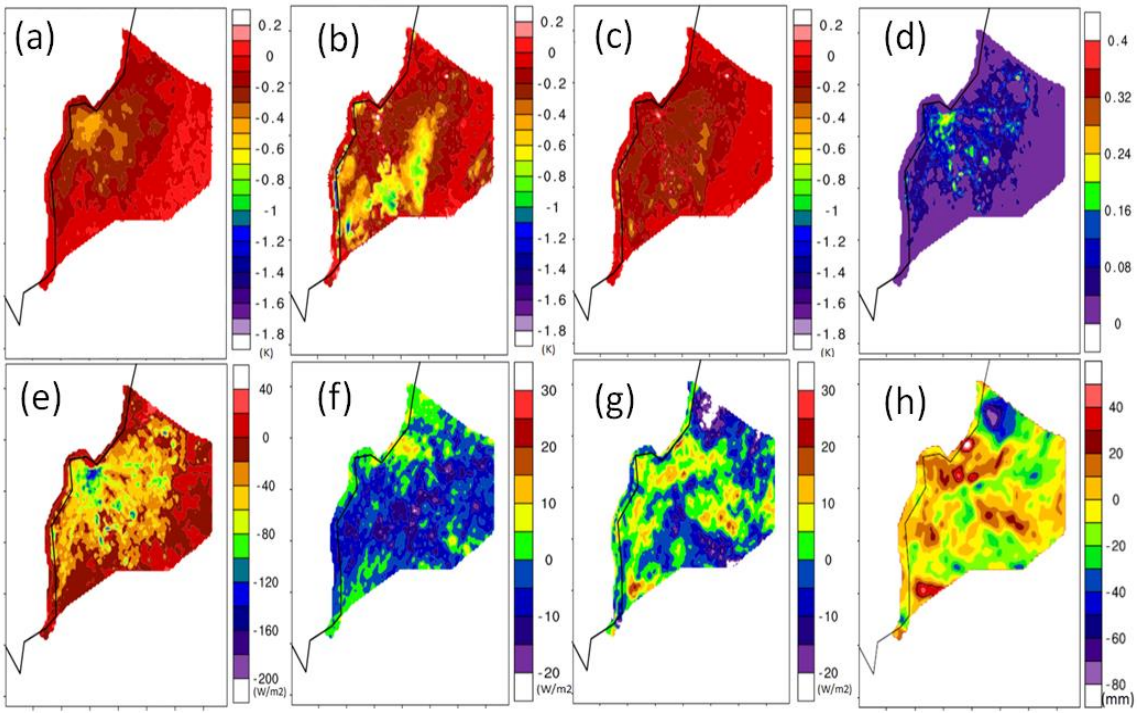

Figure 4.9 Differences between ALBEDO and BASE case (ALBEDO minus BASE) during the simulation period in (a) daily minimum surface temperature, (b) daily maximum temperature, (c) daily average temperature, (d) surface albedo at grid-level by averaging albedo values of all land covers in each 480m resolution grid cell, (e) sensible heat flux exchange between land surface and lower atmosphere between local time 3pm and 7pm, during which surface air temperature reaches its daily perk, (f) same as (e) but for the downward surface shortwave radiation blocked by clouds, (g) same as (e) but for the latent heat flux exchange between land and lower atmosphere, (h) accumulated precipitation.

Though data from other studies indicated that the average and peak ambient temperatures in urban areas decrease linearly in general as urban surface albedo increases, the efficacy of surface whitening may vary from city to city when the same mitigation strategy is applied [132, 149]. Such discrepancy may result from several factors, such as intensity of solar radiation, urban surfaces available for albedo change,

and urban morphology [164, 165]. Another factor that may potentially play an important role in determining the mitigation efficacy is the feedback through clouds, which limited studies have focused on, though the impact could be significant. For example, study [166] showed that by increasing the roof albedo in two Chicago, Illinois, neighborhoods, summer-time local 1.5m-air-temperature decreases significantly under clear sky condition. However, only 50%-70% of the clear-sky temperature mitigation can be achieved when cloudy days are also taken into account. Similar effect is also noticed by other study as well [167], in which a global-coverage gas, aerosol, transport, radiation, general circulation, mesoscale, and ocean model (GATOR-GCMOM) was used to investigate the impact of converting worldwide roof tops to white roofs. In addition, cloud feedback to the increased surface albedo may alter hydro-climate at urban and regional scale [168], resulting in potential negative consequences, such as drought.

Therefore, three factors are investigated here in their potential contributions to the spatial feature in the mitigation of daily maximum temperature. First, shortwave radiation (SW) reaching the surface changes resulting from the cloud feedback to the increased surface albedo. Figure 4.9(f) showed that weaker buoyance due to surface cooling results in less clouds in the middle of metro area, with less SW blocked by clouds and more reaching the surface. Meanwhile, sinking flow around the urban area tends to become weaker, leading to more clouds around the urban area in ALBEDO case with more SW blocked by clouds and less reaching the surface. To further confirm that the change in clouds is related to the circulation at the urban scale, instead of larger scales, we investigated the vertical profile of cloud mass during the daytime and nighttime, respectively (Figure 4.10), with no differences seen at night.

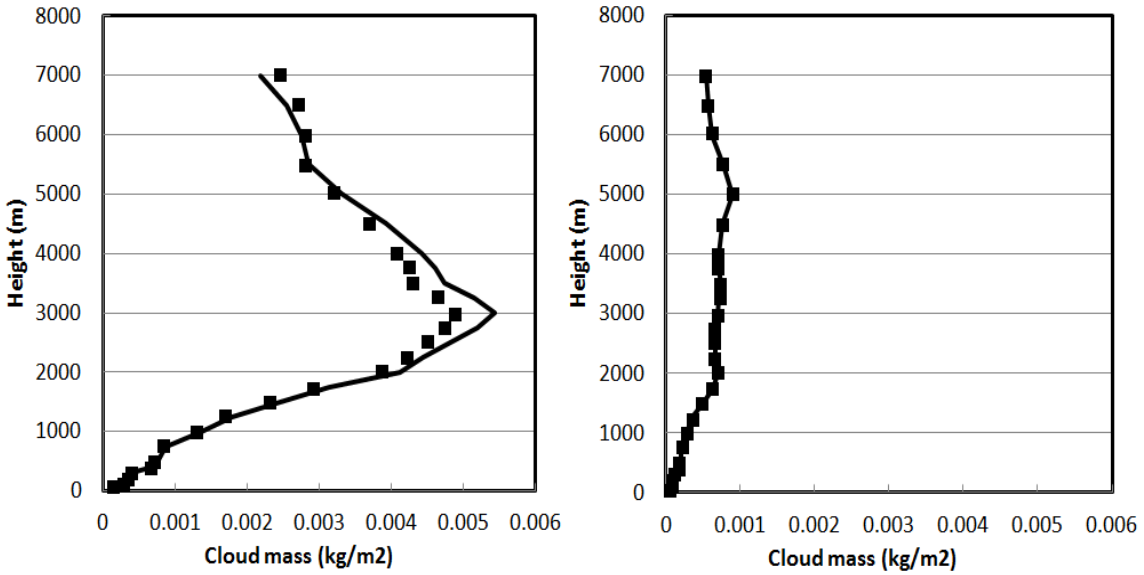

Figure 4.10 Vertical profile of cloud mass (average over the metropolitan area of Louisville, KY) for (a) daytime and (b) nighttime, with ALBEDO case in dot and BASE case in solid line.

The second factor involves cloud feedback in terms of precipitation. We found that resulting changes in latent heat follow well with that in accumulated precipitation in space (Figure 4.9(g) (h)). Change in latent heat is also important to surface whitening strategies, although it is usually not emphasized. This is because even in impervious-dense urban areas, there can be considerable amounts of vegetated patches, which are captured by sub-grid LSMs and will contribute to the grid-level latent heat flux and affect the grid-level 2m-air-temperature ultimately. In this study, both of the two cloud-related factors contribute to the stronger cooling in daily maximum temperature in the south region of the metropolitan area (Figure 4.9(f) (g)). In most of other metro regions, however, the impacts of the two factors tend to trade-off. The third factor is the change in atmospheric stability, which is critical in determining the heat exchange coefficient between 2m-air and land surfaces. Owing to the cooling in ALBEDO case, weaker circulation is expected between impervious-dense urban area and its surroundings,

leading to smaller heat exchange coefficient and consequently lower 2-m air temperature. Given the three factors discussed above, simulations with high spatial resolutions can be superior by better resolving the meteorological fields and capturing the cloud-related feedbacks.

As to the uncertainty related to the mitigation efficacy, the metro-area-averaged mitigation is significant based on the ensemble simulations. However, other sources of uncertainty, though not handled in this study can also be important, such as parameters used to drive the UCM [169]. In addition, we discussed the radiation change due to clouds feedbacks, and the radiation does not further interact with aerosols in this study, because no aerosols modules are coupled into WRF here. However, for cities heavily loaded with absorbing aerosols, impact of such clouds feedback may get amplified and even finally result in heating [167].

CHAPTER 5

INVESTIGATING THE IMPACT OF AEROSOLS FROM BIOMASS BURNING ON THE CLIMATE OF SOUTHEASTERN USA[4]

Atmospheric aerosols can affect the atmospheric conditions through 1) changing the radiation distribution by directly absorbing and scattering the solar radiation (known as aerosol direct effect); 2) modifying meteorological variables that depend closely on vertical and horizontal radiation distributions, such as planetary boundary layer (PBL) height, circulations, convection, cloud formation and precipitation; and 3) altering the formation of clouds and precipitation by serving as cloud condensation nuclei (CCN) and ice nuclei (IN) (known as aerosol indirect effect). In order to take into account the potential impacts of air pollutants to local/regional climate, chemical transport models have been coupled with regional climate models, such as WRF-CMAQ and WRF-Chem. Studies using such coupled modeling systems have shown that atmospheric aerosols can significantly influence the weather and climate at local or regional scales, such as floods [170], monsoon [171, 172], and multi-decadal variability in sea surface temperature [173].

[4] This chapter is based on the manuscript: Liu, P., Hu, Y., Nenes, A., and Russell, A.G. (2015), Contribution of the biomass burning aerosols to the climate of southeastern US during the main burning season (in preparation).

In the southeastern U.S., it has been demonstrated that biomass burning is a main source to atmospheric aerosols, especially during the main biomass burning season. Furthermore, emissions from biomass burning in the southeastern U.S. are expected to increase in the future. On one hand, wildfires are expected to increase due to climate change [174]. On the other hand, prescribed burning will become more frequent and extensive due to land use change. However, few studies have placed a particular focus the potential impact of biomass burning aerosols on the climate of this region. In this chapter, an attribution study will be carried out using the coupled WRF-CMAQ, to understand if aerosols from all emission sources do affect the climate in the southeastern U.S, how much of the impacts can be attributed to aerosols from biomass burning.

5.1 Introduction

Biomass burning (BB), as one of the largest sources of trace gases and aerosols in the atmosphere, can play an important role in air quality, weather and climate by influencing the chemistry and radiative forcing. As to air quality, studies [175-179] showed that in the southeastern US (SEUS), BB is a major source to particulate matter (PM) especially during late winter and early spring, when BB activities happen most frequently. BB is found to dominate reactive oxygen species (ROS) sources in PM during winter [180], and ROS are close related to adverse health effects of PM. Gas emissions from BB is found to contribute to the elevated ozone level, especially during heat wave events [181]. BB can also modify the weather conditions and even contribute to the extremes. For example, study [182] showed during a heat wave event in the western Europe, BB aerosols lead to the reduction in planetary boundary layer (PBL) height and horizontal wind speed, which are in favor of the air pollution. Another study [183] found that BB aerosols can increase the probability of tornado genesis, tornado intensity and longevity. As to the climate, though on global average, the radiative forcing of BB aerosols is estimated as 0.0 (-0.2 to +0.2) according to Fifth Assessment Report of Intergovernmental Panel on Climate

Change (IPCC) [184] in 2014, the climatic impact of BB can be much stronger at local and regional scales. For example, study [185] found BB aerosols intensify drought in equatorial Asia during El Niño. The radiative forcing of BB aerosols and the corresponding climate responses to BB have been investigated extensively using numerical modeling at both regional (e.g. South America; Africa) and global scales [186-190].

For the SEUS, though BB has been and will continue to be a major contributor to the aerosols, especially at lower atmosphere, existing studies specific for this region have mainly focused on the contribution of BB to aerosol mass or on the radiative forcing of BB aerosols [178], with limited studies regarding the potential impact of BB on regional climate. Therefore, the main task of this study is to understand under the current climate conditions, if aerosols from all emission sources do have an impact on the regional climate of SEUS, how much of the impact can be attributed to the BB aerosols. This study will particularly focus on the main biomass burning season in the SEUS (from January to April).

The impact of BB in SEUS can also be extracted from the existing studies in which global models are used. However, the relative coarse spatial resolutions in global models may make the estimates less reliable. For example, one study [191] showed the properties of BB aerosols change rapidly within the 2-4 hours after emission, which is neither covered by emission inventories nor captured by large-scale model simulations due to its relative coarse temporal and spatial resolution. In addition, it has also been found that the impact on clouds estimated in general circulation models (GCMs) can be five times smaller than that estimated through large eddy simulations (LES) due to the parameterization schemes in GCMs [192]. Therefore, this study is to use the regional climate model WRF (Weather Research and Forecasting) [14], coupled with the chemical transport model CMAQ (Community Multiscale Air Quality) [16] to estimate the contribution of BB to regional climate, so that the results may benefit from the relative

high spatial and temporal resolutions in meteorology and emissions, and from more detailed and complex chemistry processes in the atmosphere described by CMAQ.

5.2 Methods

5.2.1 Simulation Design

Existing studies show that large uncertainties exist in the estimates of the radiative forcing of BB aerosols and the climate responses, because compared with aerosols from other sources, BB aerosols have the following features: (1) BB aerosols are more abundant in absorbing components, namely black carbon and brown carbon [193]. (2) Large variance exists in the optical properties of black carbon (e.g. due to different mixing states) and brown carbon [194]. (3) The amount of BB emissions and plume height vary significantly from burning event to event. (4) Both the instantaneous [195] and equilibrium climate forcing and response [196] of BB aerosols depend highly on the horizontal and vertical distributions of absorbing aerosols, which vary significantly temporally and spatially. As a result, the convection, atmospheric stability and circulation are modified at different scales, which may lead to opposite impacts on clouds [186, 197] and radiative forcing. (5) The variation in other meteorological fields may also affect the cloud feedback to BB aerosols, such as the background column water vapor [198]. To account for the uncertainty in assessing the climate impact of BB, simulation with ensembles is necessary, which usually involves multi-year/decade simulations [188, 190, 199] and can be computationally demanding.

In this study, instead of the conventional ensemble method, a new ensemble method [200], referred to as “short ensembles”, is applied, in which the continuous multi-year long climate simulation is replaced by the ensembles of short-term simulations, as long as the ensembles are able to represent the climate. The “short ensembles” method is suitable to the situations, where the impact of fast processes (those that produce a model response

to a perturbation on a timescale of days for simulations with fixed sea-surface temperature) is investigated. The aerosol-related processes, such as the change in radiation and clouds, belong to the fast processes, as what is interested in this study. In addition, given that the primary goal of this study is to serve as an attribution study of the impact of BB to regional climate under the current climate conditions, instead of the equilibrium climate forcing and response, the climatic fields that take longer time to change and may regain equilibrium after long-term simulations, are not expect to change. Therefore, the "short ensembles" method fits the research goal of this study, and is much more computational effective compared with the conventional ensemble method.

To generate a representative estimate in terms of the impact of BB aerosols on regional climate, enough short ensembles are needed to cover a variety of atmospheric conditions and the wide variance in BB emissions as well. In the SEUS, the BB activities are usually most active from the middle of January to the middle of April, and this period from the year of 2006 to 2009 are investigated to represent the current climate and provide enough variability in meteorological conditions, as the impact of BB may vary with meteorological conditions. For each year, 4 short ensembles are included to cover the main biomass burning season, with a 22-day-period for each ensemble. For each ensemble, the first 8 days are used to spin-up, which has been demonstrated to be long enough for the model to produce responses to the perturbations from aerosols. The results from remaining 14 days will be used for the analysis.

As to the emission used for WRF-CMAQ, no difference in the emissions exists between different years. In other words, the emissions only carry the daily variability from January to April. The emissions, except fires, are mainly based on the emissions of the year 2007, which was originally prepared for another research project and has been described in detail and evaluated comprehensively [201]. The fire emissions are mainly derived by averaging the fire emissions across the year 2006 to 2008 to smooth the

episodic nature of fire emissions, so that the fire emissions represent a more typical level of BB emissions at present [201].

To estimate the relative contribution of BB aerosols to the total aerosols in terms of the impact on regional climate, 3 cases are simulated in this study. The first case serves as a control run, referred to as case CONT, with no aerosols in the modeling system. The second case, referred to as case ALL, includes all emission sources. Hence, the difference between ALL and CONT represents the impact of total aerosols. The third case, referred to as case NOFIRE, has the same emissions as case ALL, but excluding the emissions from BB. Therefore, the contribution from BB aerosols can be estimated from the difference between case ALL and case NOFIRE, and then compared with the impact from total aerosols. WRF version 3.3 is used for the case CONT. For case ALL and NOFIRE, the coupled WRF-CMAQ [37] with CMAQ version 5.0.1, is used to include the atmospheric chemistry processes into the meteorology. In addition, spectral nudging is applied during the simulation to guarantee that the three cases are under the similar climate conditions at large scales. Spectral nudging is applied to temperature, geopotential height and wind above the planetary boundary layer (PBL) to constrain the meteorological features at the scales of 800 km and larger.

5.2.2 Model Description

The simulation domain covers the middle and eastern U.S. (Figure 5.1) with a grid spacing of 12-km, and includes 180 × 189 grid cells in the latitudinal and longitudinal directions, respectively. To better capture the current climate conditions, reanalysis data are used to drive the regional climate model, instead of outputs from general circulation models. Here, the North American Regional Reanalysis (NARR) data is used, which covers North America with a temporal resolution of 3 hours and a spatial resolution of 32 km [67]. The main model configurations in WRF are as follows: 34 vertical layers with model top at 100hPa; Noah land surface model; Monin-Obukhov scheme for the surface

layer and Yonsei University scheme for PBL; Lin scheme for cloud microphysics; Kain-Fritsch scheme for cumulus convection; RRTMG scheme for long wave and short wave radiation transfer. For CMAQ, CB05 mechanism [202] is used for gas chemistry and aero6 for aerosol mechanism [203]. As to the aerosol optical properties, elementary carbon is the only absorbing aerosol component. The version of WRF-CMAQ used in this study does not include the interactions of aerosols with long wave radiation. This is not expected to be an important issue for this study, because the optical depth of BB aerosols damps rapidly as wavelength exceeds 600nm [204, 205].

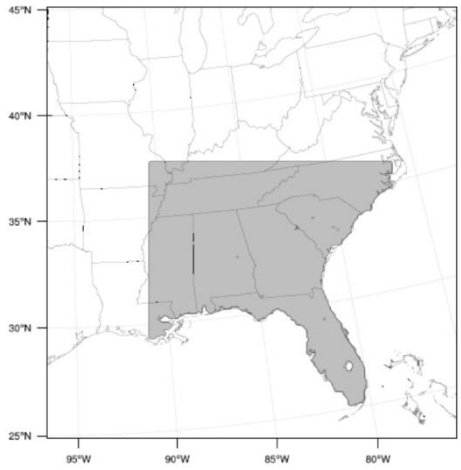

Figure 5.1 Simulation domain with grid spacing of 12km, with the shaded area as the area of interest of this study, which covers the most areas of the U.S. EPA region 4 for the southeastern U.S.

A limitation of this study is that the aerosol indirect effect is not included in the WRF-CMAQ system. Hence, any changes related to clouds and precipitations are only caused by the changes in atmospheric conditions originally generated from aerosol direct effect. The aerosol indirect effect from BB is expected to have a minor impact on the results [206], because the spatial resolution of 12km is still too coarse to solve the clouds. Therefore, this study provides a first-degree quantitative estimate of the radiative forcing

and climate response of BB aerosols during the main BB season in the SEUS. Continuous efforts in the future would be needed to include the aerosols indirect effect and conduct the simulations at cloud-resolved resolutions. It would be very interesting to find out to what extent the conclusions drawn in this study may change.

5.3 Results

If not stated explicitly, all results shown in this section are ensemble averages, that are calculated from the results of 224 days from the 16 ensembles (14 days in each ensemble). Hence, the ensemble average represents the climatic mean of the simulated season. As to the regional average, the region refers to the shaded area in Figure 5.1.

5.3.1 Aerosol Loadings

The contribution of biomass burning to the total aerosol loadings is first investigated. Given that elementary carbon (EC) is the only component that absorbs the solar radiation described in the model, the aerosol loadings are grouped into two, with the first group only including EC, and the second group including the scattering aerosol components, namely inorganics, primary and second organic matters.

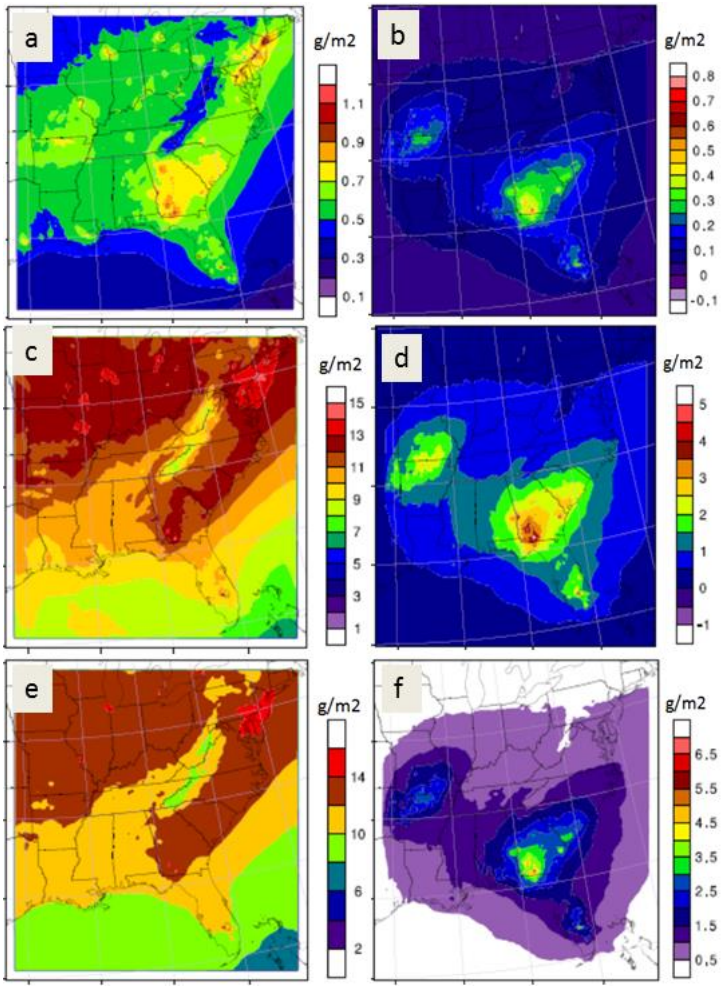

Figure 5.2 Column total aerosol loadings for (a) elementary carbon in case ALL, (b) the contribution from biomass burning to elementary carbon, which is the difference between ALL and NOFIRE cases (ALL minus NOFIRE), (c) scattering aerosols in case ALL, (d) the contribution from biomass burning to (c), (e) the sum of (a) and (c), (f) the sum of (b) and (d).

The spatial distribution of aerosol loading shows that two areas are mainly influenced by biomass burning (Figure 5.2). One area is the region of the southeastern U.S., which is the area of interest in this study, and the other area is around the states of Missouri and Arkansas. For both the absorbing and scattering aerosols, if BB aerosols are removed, the spatial distributions of aerosol loadings tend to become smoother over most of the

simulation domain, except a region in the northeastern U.S. In other words, biomass burnings from these two areas generate an extra horizontal gradient of the aerosol loading, and may potentially lead to the change in circulations, as suggested previously [197]. The results also show that for these two areas, biomass burning in general has a stronger contribution to EC loading than to other components, as biomass burning emissions are usually more abundant in EC than other emission sources. For example, in the southwest of Georgia, about 50% of the column total EC can be attributed to biomass burning; while about 30% of the scattering aerosols can be attributed to biomass burning.

In addition to the spatial distribution, aerosol vertical distributions are also of importance, especially for the absorbing aerosols. As demonstrated by multiple studies, absorbing aerosols at different heights may have contradicting impacts on atmospheric conditions and cloud formation [186, 197]. Therefore, the regional average aerosol concentration is calculated at different heights. The results (Figure 5.3) show that impact of BB can reach to the height of about 3 km, with the strongest impact from the surface to about 1 km, which is above the regional average planetary boundary layer (PBL) height (~ 700 m). For both absorbing and scattering aerosols, the contributions from BB are statistically significant at 95% confidence interval from surface to the height of 1 km. Another interesting feature to note is the change in the standard deviation (SD) between ALL and NOFIRE cases, with the former usually carrying a much wider variance than the latter at the same height. This feature implies that with the simulation design in this study, the ensembles are good at covering the wide variance in biomass burning emissions with relative uniform emissions from other sources over the simulated season, so that the mean impact of biomass burning for the season can be estimated. In addition, it would be interesting to find out if a similar change in SD also exists for other climatic fields (such as clouds), because such information indicates how sensitive those fields are to the variance of biomass burning.

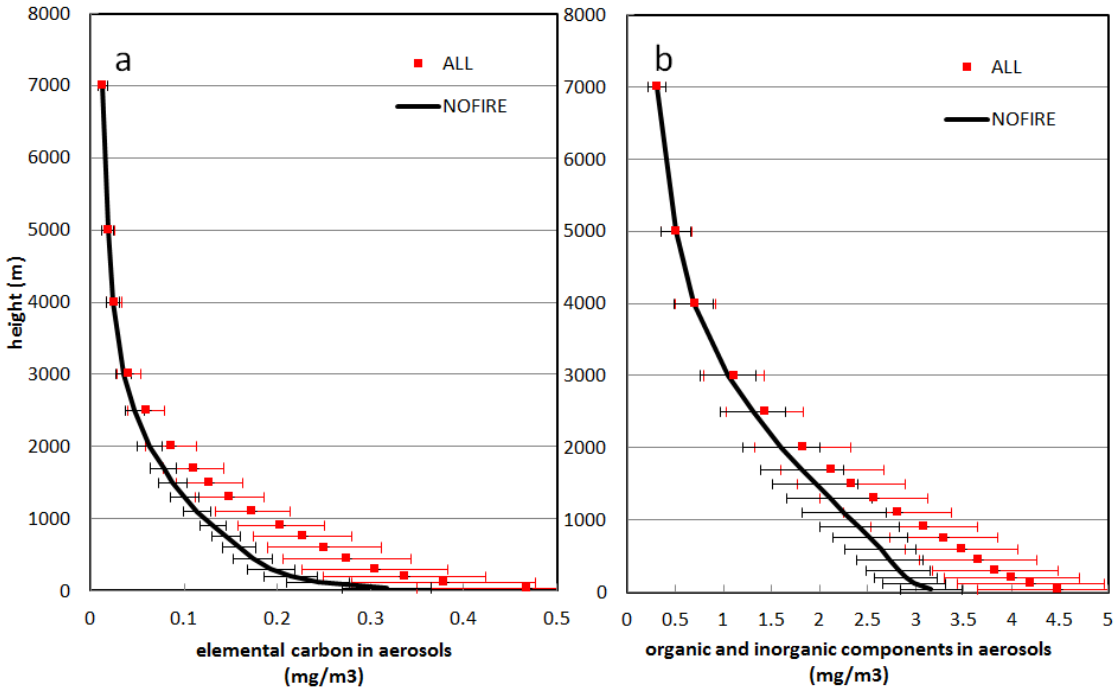

Figure 5.3 Regional average aerosol concentrations with height (a) for elemental carbon, and (b) for the scattering components, with error bar as the standard deviation calculated from 224 days of the 16 ensembles. The results for case ALL are in red, and NOFIRE case in black.

5.3.2 Impacts on Regional Climate

5.3.2.1 Radiation and Aerosol Radiative Forcing

Studies have shown that BB can substantially change the radiation energy distribution vertically during a single burning event, and as response, leading to a series of change in atmospheric conditions. For example, during summer 2007, it was found that [207] BB from Greece results in a reduction of ~ 50W/m^2 at the ground surface and the atmospheric heating of ~ 30W/m^2 for the shortwave radiation over the central Mediterranean area. Therefore, in this study, the impact of BB aerosols on the vertical

distribution of radiation energy is first investigated. Radiation that reaches the land surface, radiation that leaves the model top toward upper atmosphere, and the radiation in the atmosphere are calculated for each case, respectively (as summarized in Table 5.1).

Table 5.1 Summary of the regional average short wave (SW) and long wave (LW) radiation (in unit of W/m^2) under the conditions of clear sky and of total sky (namely with clouds included), respectively, with the standard deviation in parenthesis

			CASE		
			CONT	ALL	NOFIRE
Reaching the surface	SW	clear sky	252.3 (47.2)	247.3 (46.5)	247.9 (46.4)
		total sky	212.4 (52.7)	197.6 (58.2)	198.1 (58.2)
	LW	clear sky	296.7 (30.5)	288.4 (31.7)	288.4 (31.7)
		total sky	309.2 (33.5)	306.6 (37.0)	306.6 (37.0)
Leaving from model top toward space	SW	clear sky	58.2 (7.6)	60.3 (7.5)	60.3 (7.5)
		total sky	93.7 (30.0)	102.6 (33.1)	102.7 (33.1)
	LW	clear sky	247.8 (8.9)	253.2 (9.8)	253.2 (9.8)
		total sky	213.0 (24.7)	218.5 (24.4)	218.5 (24.4)
Atmosphere	SW	clear sky	67.4 (12.7)	69.9 (13.2)	69.4 (13.2)
		total sky	64.9 (12.2)	68.6 (13.0)	68.1 (13.0)
	LW	clear sky	-139.0 (13.4)	-152.1 (14.9)	-152.1 (15.0)
		total sky	-115.8 (17.3)	-134.5 (20.2)	-134.5 (20.2)

In general, the impact from total aerosols emerges with significant change in the radiation distribution is found between CONT and ALL cases. Small or little difference is found between ALL and NOFIRE cases. Hence, the contribution of BB on vertical radiation energy distribution is very weak in terms of the regional average. In addition,

little change in SD is found between ALL and NOFIRE case, indicating that the radiation energy is not sensitive to the range of concentrations that biomass burning aerosols vary.

For the shortwave (SW) radiation, the aerosol direct radiative forcing is estimated based on results in Table 5.1 under clear sky condition (summarized in Table 5.2). To clarify, the values obtained in Table 5.2 are slightly unbalanced, with the cooling effect at surface not equal to the total effects from the atmosphere and model top. This is because in Table 5.1, the radiation reaching the surface is not a net effect, and it only includes downward SW from atmosphere to the surface, but not the upward SW from the surface to atmosphere.

Table 5.2 Summary of aerosol direct forcing for shortwave radiation (in unit of W/m^2) for aerosols from all emission sources and from biomass burnings aerosols, respectively, with the standard deviation in parenthesis (Negative values represent the cooling effect and positive values represent the warming effect)

	all emissions	biomass burning
Surface	-5.0 (1.57)	-0.6 (0.54)
Model top	-2.1 (0.89)	0.0 (0.03)
Atmosphere	2.5 (1.05)	0.5 (0.45)

The positive radiative forcing of aerosols in the atmosphere results from the SW absorbed by EC. At the model top, BB aerosols provide a zero forcing in terms of regional average, which means that for BB aerosols, the SW radiation scattered in the atmosphere toward model top is almost completely compensated by the absorption of EC in BB aerosols. Therefore, BB emissions do not contribute to the cooling effect of 2.1 W/m^2 at model top for "all emissions". The results indicate that if increasing EC in BB emissions with other emissions unchanged, the amount of EC may have to increase at least by a factor of 4 to absorb the SW radiation scattered by other aerosols, and lead to

the change in radiative forcing of total aerosols from negative to zero or positive at the model top. Furthermore, if brown carbon from BB is taken into account, BB aerosols will have a net heating effect. Therefore, for the research in the future, it would be very interesting to see how results may change by including the brown carbons. Last, the SD of BB aerosol radiative forcing at the model top is one order of magnitude smaller than the SD of radiative forcing at the surface and in the atmosphere, indicating that the variance in the ratio between absorbing and scattering components in BB aerosols is much smaller than the variance in the BB aerosol loading itself. This is consistent with findings by other studies, which showed that for BB aerosols, the mass ratio of black carbon to organic matters usually falls between 0.05 to 0.1 [208].

Though the contribution of BB aerosols to the radiative forcing of total aerosols is statistically significant at a 95% confidence interval, the absolute magnitude is small, so that the question arises as if such small change matters to other climatic fields, which will be discussed in the following sections. In addition, a variety of important climatic fields are also investigated, as these fields may respond substantially to the horizontal radiation redistributions due to BB aerosols.

5.3.2.2 Temperature

Temperature, as one of the primary climatic fields, and is closely related to the energy distribution. Here, the surface air temperature at 2m height (T2) is examined, as it is also an important property to air quality and heat stress related to human health. Then, the vertical distribution of temperature is investigated.

Comparing ALL with CONT case, significant cooling is found for T2, with a regional average T2 decrease by 1.5K. The change in T2 is generally in agreement with the spatial distribution of aerosol loadings (Figure 5.2e and Figure 5.4a). However, the reason behind is not the direct cooling of T2 during the daytime, when solar radiation interacts strongly with the aerosols. Instead, the cooling of T2 during the nighttime contributes

mainly to the average T2 decrease (Figure 5.5). This is because during the daytime, when aerosols are included into the system, the decrease in solar radiation reaching the surface is to a large extent compensated by the reduced latent heat flux exchanged between the land surface and atmosphere. During the nighttime, however, longwave radiation dominates the surface energy balance and the cooling effect in land surface temperature during the daytime emerges to affect T2.

Though the impact of surface cooling due to the total aerosols is significant over the SEUS, little of the cooling in T2 can be attributed to BB aerosols, with a regional average T2 decrease by 0.05K due to BB aerosols. This is because the cooling in T2 results from the radiative forcing of aerosols and of clouds as well. The cloud radiative forcing is discussed later in section 5.3.2.4. It is found that compared with CONT, both aerosols and cloud change in ALL cool the surface with similar magnitude; while no cooling effect due to the cloud change in ALL can be attributed to BB, though BB aerosols contribute to about 10% of the radiative forcing of total aerosols.

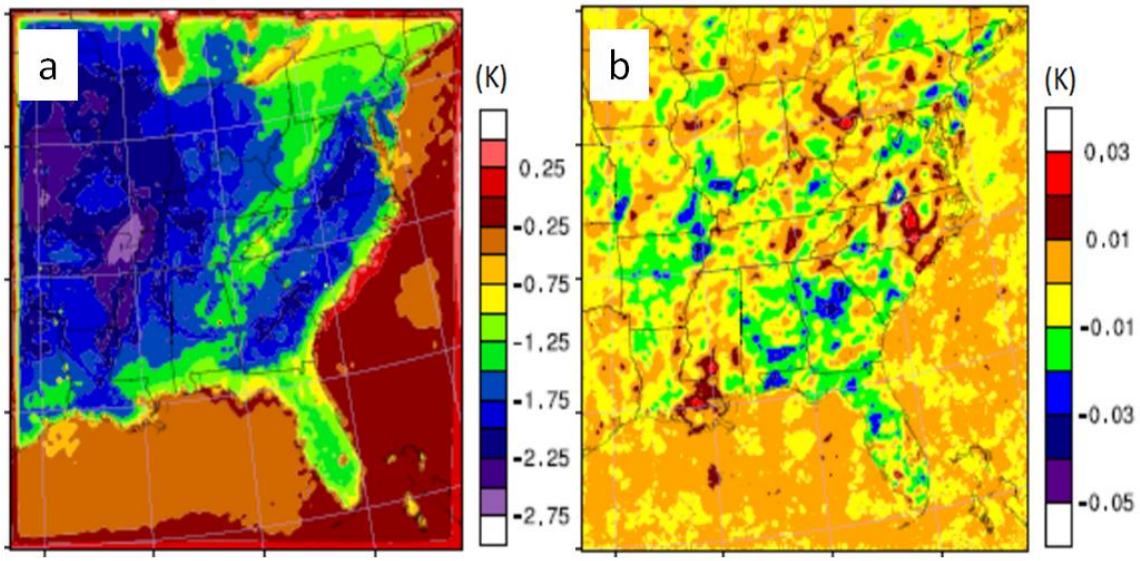

Figure 5.4 Air temperature at 2m height for (a) difference between ALL and CONT cases (ALL minus CONT), and (b) difference between FIRE and NOFIRE cases

As to the spatial pattern, though in general BB contributes to slight cooling over the southeastern U.S. and the region around Missouri and Arkansas (Figure 5.2f and Figure 5.4b), the change in T2 bears perturbations at scales much smaller than the T2 change due to all aerosols, and the small perturbations may result from the combined impacts of BB and the random errors in the modeling system.

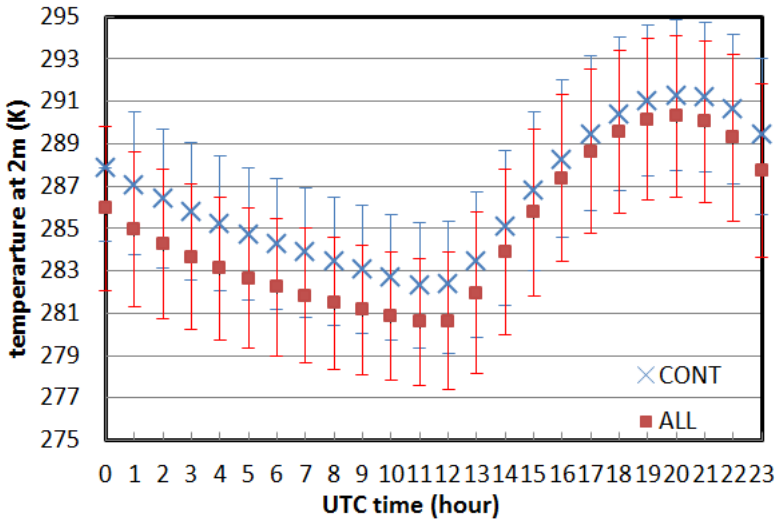

Figure 5.5 Diurnal cycle of the regional average air temperature at 2m height for case CONT and case ALL, with error bars as the standard deviation

The vertical distribution of temperature is also of interest, because it is closely related to atmospheric stability. Comparing ALL with CONT case (Figure 5.6), cooling is found from surface to about PBL (~ 700 m) with a slight temperature inversion from surface to about 100 m, and difference disappears above PBL, though above the PBL the aerosol concentrations are still high (Figure 5.3). The main reason is that temperature is nudged above PBL at scales of 800km and larger, so that little difference is seen in terms of the regional average. However, this does not mean that imposed constraints by nudging are too strong and not reasonable for the research goal of this study. In later section 5.3.2.3, it is shown that compared with CONT, circulations at lower atmosphere in ALL is modified

at scales much larger than the scale of circulation change due to BB aerosols alone. Comparing ALL with NOFIRE case, no difference is found at all heights. Though BB aerosols contribute to the atmosphere heating by 20% under clear sky (Table 5.2), the impact is too weak compared with other factors that determine the air temperature profile, such as clouds, which will be shown later in section 5.3.2.4. In addition, no difference is found in terms of the standard deviation, suggesting that temperature is not sensitive to the variance in BB aerosols even within PBL, where the influence and variance of biomass burning are expected to be strongest.

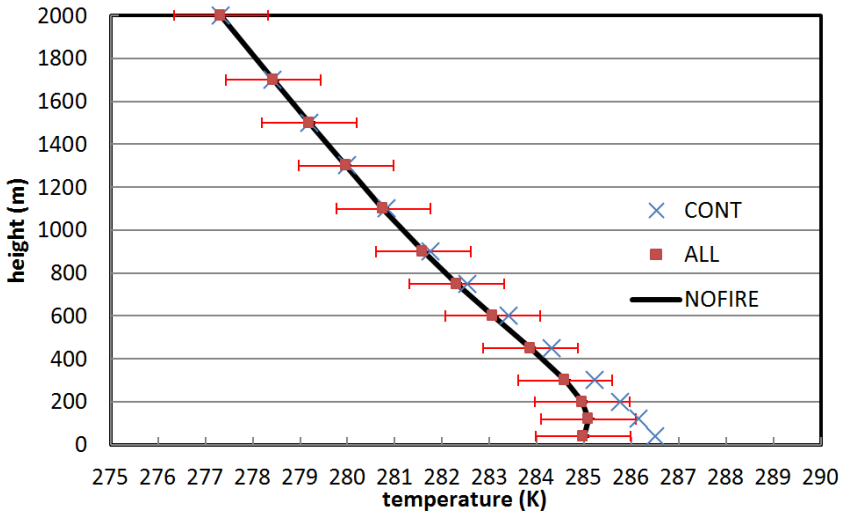

Figure 5.6 Regional average temperatures with height, with error bar as the standard deviation calculated from all 224 days of the 16 ensembles. Only the standard deviation of ALL case is shown, because all cases have similar standard deviations at the same height.

5.3.2.3 Circulations

Another important aspect to investigate is the potential change in circulations. Here, the wind fields at surface (10m height), 850 hpa are shown. The wind at 500 hpa was also examined with little change found between the three cases and not shown here. For CONT case, in general, the circulation of the simulation domain is determined by the large-scale circulations of the Hadley cell and the Ferrel cell. Around the middle of

troposphere (500 hpa), westerlies prevail. As going toward lower levels of the atmosphere, trade winds come into play as well, which blow from the southeast into the simulation domain around the south of 30N (Figure 5.7 a b). The descending motion of the Hadley cell also contributes to the formation of the high pressure system at the surface, the center of which is located on the east of Florida (Figure 5.8a).

Comparing ALL with CONT case, the pressure gradient from the center of high pressure system to the land decreases (Figure 5.8b), because of the substantial cooling of the land surface in ALL case. As a result, the surface winds become weaker by about 20% over the land on average (Figure 5.7c). The impact of surface cooling on the atmosphere almost disappears when the altitude increases to 850hpa (about 1.5km in height). Comparing ALL with NOFIRE case, little change is found in wind speed (Figure 5.7e f), with wave-like perturbations at small scales uniformly distributed over the total simulation domain, as found in T2 (Figure 5.4b). The results suggest that the perturbations introduced by total aerosols are able to modify the circulations at lower atmosphere. However, perturbations due to BB aerosols are too weak to develop into features at larger scales and to finally contribute to the circulation change due to total aerosols. In addition, the perturbations in circulations due to BB aerosols occur at scales much smaller than 800 km (Figure 5.7 e f). Given that no nudging was applied below PBL or scales smaller than about 800km, the small-scales perturbations from BB aerosols was not depressed from growing due to the implementation of nudging.

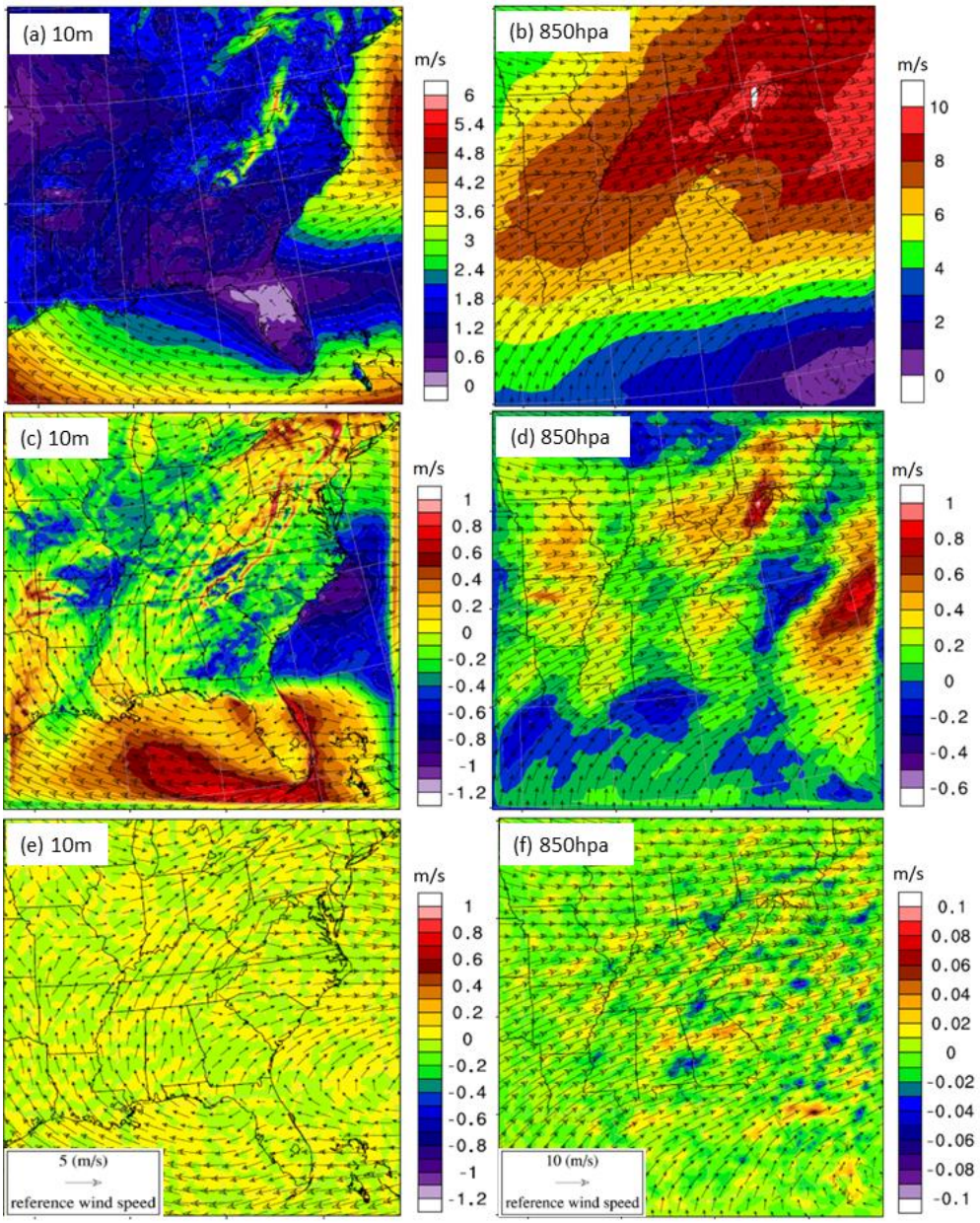

Figure 5.7 Wind field at 10m height (a, c, e) and at 850 hpa (b, d, f). The vectors represent the wind field for CONT case (a , b), for ALL case (c, d) and for NOFIRE (e, f). The reference wind speed vectors at 10m height and at 850 hpa are shown in the bottom left corner of plot (e) and (f) respectively. The contours represent the wind speed of CONT case (a, b), the wind speed difference between ALL and CONT (c, d), and the wind speed difference between ALL and NOFIRE (e, f).

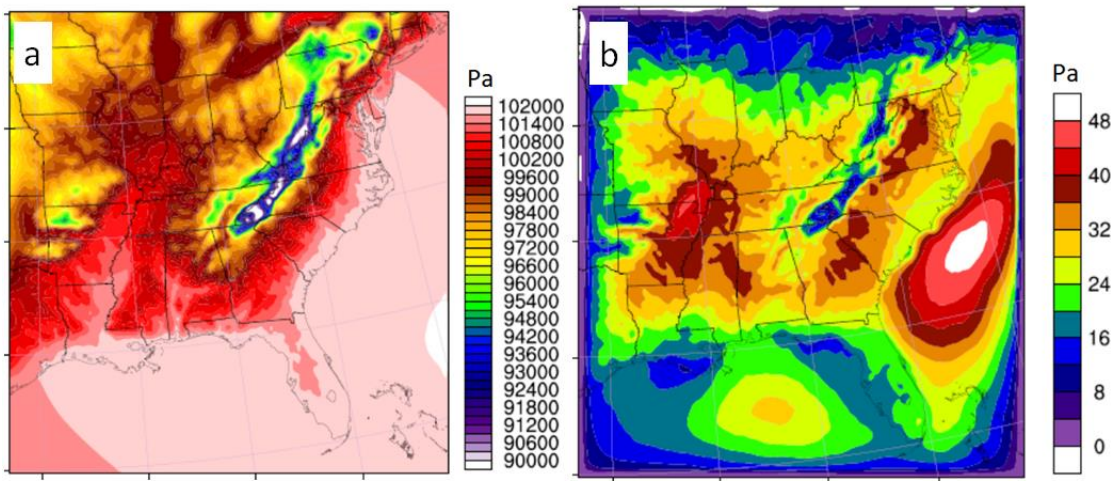

Figure 5.8 Sea surface pressure for (a) CONT case, and (b) difference between ALL and CONT case.

5.3.2.4 Clouds and Precipitation

Clouds, as mentioned before, play an important role in climate through interacting with radiation directly and through a series of responses to the perturbations in the system. Here, the cloud radiative forcing (summarized in Table 5.3) is first investigated, which is obtained from the difference between clear and total sky condition based on Table 5.1.

Table 5.3 Summary of cloud radiative forcings (in unit of W/m^2), with negative values representing the cooling effect and positive values representing the warming effect

		CASE		
		CONT	ALL	NOFIRE
Surface	SW	-39.9	-49.7	-49.8
	LW	12.5	18.2	18.2
Model top	SW	-35.5	-42.3	-42.4
	LW	34.8	34.7	34.7
Atmosphere	SW	-2.5	-1.3	-1.3
	LW	23.2	17.6	17.6

Compared with CONT, significant change is found in cloud radiative forcing in ALL (Table 5.3). The results also indicate the role that clouds play in redistributing the

radiation energy vertically. For example, compared with CONT, more LW radiation is emitted back to the surface in ALL, and less trapped within the atmosphere, which is related to the change in cloud amount and cloud height, as confirmed later in Figure 5.9. The contribution of BB aerosols to the change in cloud radiative forcing is found to be little, different from its contribution to the aerosol radiative forcing (Table 5.). The results suggesting that in terms of the regional average, impact from BB is too weak to change the cloud feedbacks.

An interesting thing to note is that when comparing ALL with CONT case, clouds actually provide a positive feedback to the initial surface cooling generated from the inclusion of aerosols in terms of the regional average. Comparing ALL case with CONT, the aerosols exert a cooling effect of 5.0 W/m^2 at the surface (Table 5.2). Meanwhile, the cloud cooling effect on surface also increased by 9.8 W/m^2 in SW and warming effect increases by 5.7 W/m^2 in LW (Table 5.3), leading to a net cooling effect of clouds of 4.1 W/m^2 on top of the aerosol cooling effect. To understand the reasons behind the positive cloud feedback to the surface cooling, the vertical distributions of clouds and relative humidity (RH) are shown below.

The results clearly show that compared with CONT, there is a significant increase in clouds from surface to about 500m for ALL case. The change of RH with height is similar to that of cloud water. When aerosols are introduced into the system, surface cooling weakens the convection and tends to depress the low-level cloud formation, as shown of the temperature inversion from surface to about 100m in Figure 5.6. However, the cooling of near surface air may also result in higher RH and tends to favor cloud formation. The net effect is determined by the two competing effects. From 500m to about PBL height, ALL has similar cloud amount to CONT. Then starting from 1km to 4km, less cloud is found in ALL with lower values in RH and temperature compared with that of CONT case at the same height, suggesting that the cloud formation is mainly reduced due to the decrease in water vapor. This is consistent with the radiation analysis

in section 5.3.2.1. For the LW radiation under clear sky, more energy is emitted from the atmosphere in ALL compared with CONT (Table 5.1).

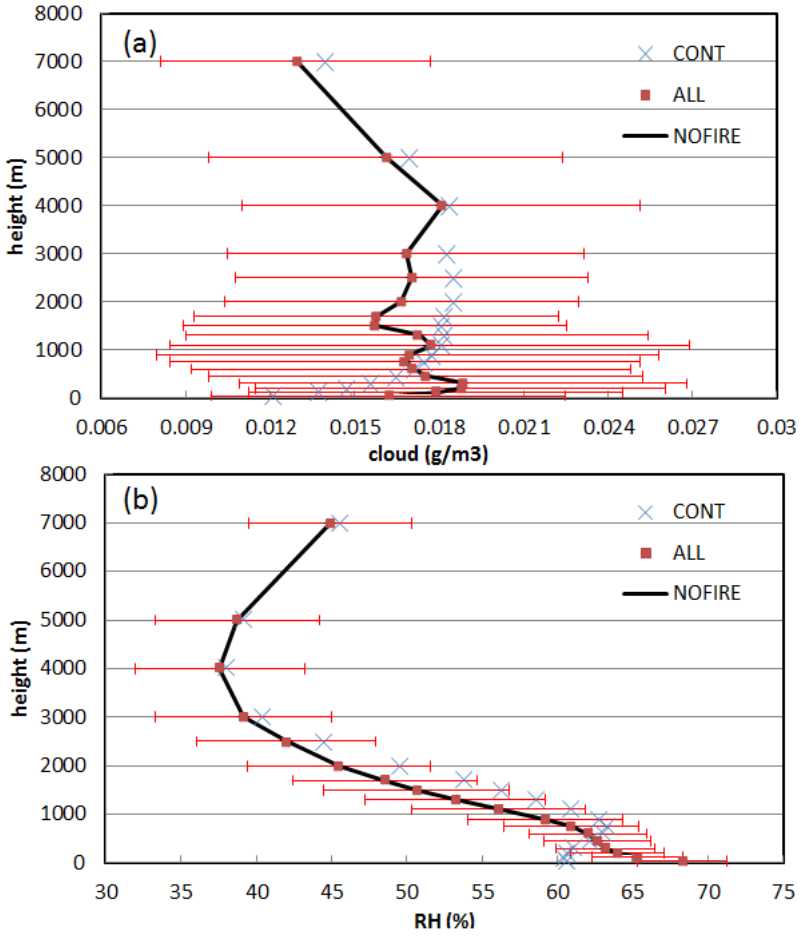

Figure 5.9 Regional average cloud water (a) and relative humidity (b) change with height, with error bar as the standard deviation calculated from all 224 days of the 16 ensembles. Only the standard deviation of ALL case is shown, because all cases have similar standard deviations at the same height.

As to the total precipitation over the southeastern U.S., no significant difference is found between ALL and NOFIRE cases in terms of the mean and distribution of precipitation. Comparing ALL with CONT case, less precipitation is found in ALL for the regional average, which may have potential impacts on regional climate during the

seasons following the simulated biomass burning season. However, no difference shows in soil moisture between ALL and CONT, because the reduced precipitation in ALL is balanced by the reduction in latent heat from land surface in ALL.

5.4 Discussion and conclusions

An interesting thing to point out here is the change in PBL height, which can be very important to regional climate and air quality. Compared with CONT case, ALL case has a higher PBL height (Figure 5.10), though ALL has a cooler surface so that lower PBL height is usually expected. The reason is that ALL case may have a stronger wind shear due to decreased wind at surface and the slightly increased wind at upper level, as found in section 5.3.2.3 (Figure 5.7), so that the increased turbulence via mechanical may compensate or even exceed decreased turbulence via buoyance. This result also reconfirms that compared with CONT, the circulations are modified by total aerosols at scales much larger than that by BB aerosols alone, and that the constraints imposed by nudging are reasonable for the research purpose of this study.

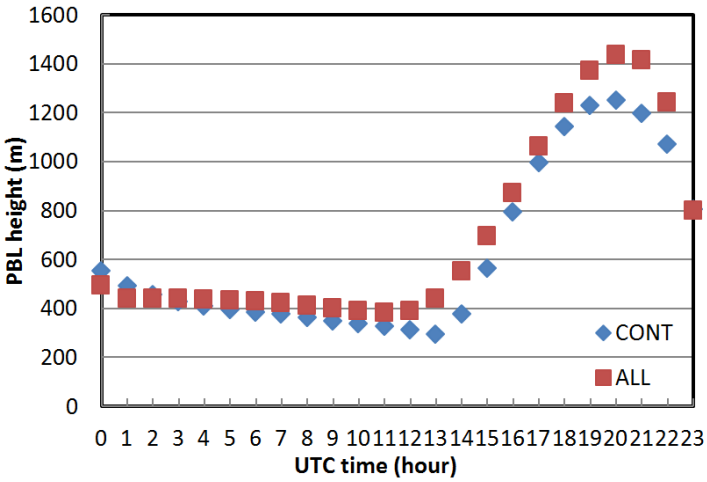

Figure 5.10 Diurnal cycle of the regional average PBL height

To summarize, in this chapter, compared with aerosols from all emission sources, the relative impact of biomass burning aerosols to the climate is estimated for the southeastern U.S. over the main burning season in this region. Simulations using "short ensembles" were conducted, which successfully covered the wide variance in biomass burning emissions and the atmospheric conditions during the burning season from the year 2006 to 2009.

A variety of climatic fields that are important to regional climate are investigated, including radiation, temperature, regional circulations, clouds and precipitation. The results showed that the total aerosols do have a significant influence on the climate in the southeastern U.S. during the season investigated. Though biomass burning is an important contributor to the total aerosol loading in the SEUS, BB aerosols contribute little to the impact on regional climate from total aerosols in terms of the ensemble mean of the regional average. In other words, perturbation induced by biomass burning is in general too weak to develop into features at larger scale and finally affect the regional climate.

In addition, though the wide variance occurs in the aerosol loadings from biomass burning, the investigated climatic fields are not sensitive to the wide change in biomass burning emissions. It is true that locally, the meteorological fields can be affected substantially by biomass burning. However, as mentioned, such local perturbations do not develop into features at larger scales to modify the climatic fields in terms of the regional average of the southeastern U.S.

CHAPTER 6

SUMMARY AND FUTURE DIRECTIONS

Towards the ultimate goal of understanding the impact of climate-responsive strategies on air quality, main efforts of this thesis are placed on to improve the performance of dynamic downscaling by nudging, and to better simulate the impacts of land use/land cover and biomass burning aerosols on regional climate.

First, this work clearly demonstrated that during dynamic downscaling, spectral nudging is superior to grid nudging by providing comparable high similarities to grid nudging at the large scale, and by providing reasonable low similarities at the small scale. With the insight into the impact of nudging during the dynamic downscaling shown by this work, continuous improvement in the general performance of dynamical downscaling can be possible. There have been contradicting results regarding whether dynamical downscaling provides added value to its driving fields. Studies that demonstrated that dynamic downscaling succeeded in adding value to its driving fields at small scales, used reanalysis data as the driving fields [209-211]; while the failed cases used outputs from GCMs as the driving fields [212]. It is not surprising that the downscaling performance is closely dependent on the quality of the driving fields. The reanalysis data provides "perfect" inputs to RCMs. However, no "perfect" inputs are available for future climate projections from GCMs. As mentioned in the very beginning of the thesis, of all four types of downscaling applications, from type 1 to type 4, constraints from real-world observation diminish. Pielke et al. [26] even asserts that type 4 dynamic downscaling fails to improve accuracy beyond what could be achieved by interpolating global model predictions onto a finer-scale terrain or landscape map. The main reasons behind the deteriorated downscaling results are due to the issues in GCMs, which are beyond my research scope. What I am interested is to explore the possibility to

use the tools of nudging help identify the main obstacles in the way of RCMs to add values at small scales. For example, during the downscaling, spectral nudging will be used to ensure that the RCMs do not drift away from the large-scale features. At the same time, different from the conventional practice in dynamical downscaling, a random/system bias can be introduced to the nudging fields to mimic the potential bias in GCMs, so that the most possible field/bias that hinders the RCMs from adding variance. With spectral nudging, the scales of input fields, at which the added values by downscaling will become deteriorated or hindered, can also be determined. Such information can be useful when choosing a GCM / ensembles of GCMs as the driving fields for RCMs, and can also provide additional criteria to evaluate the GCMs. What is more, the tools of nudging can also help to better understand the relative contributions of forcings at different scales to the added values during downscaling, and to better understand whether the features at small scales (or perturbations introduced at local/regional scales, e.g. land use change at scales of cities, emissions from biomass burning, and etc.) can develop into features at larger scales and even interact with the driving fields.

In this study, the widely used Noah land surface model has become more powerful by developing the sub-grid approach for it, termed as S-Noah. The performance of S-Noah was evaluated at the sub-grid level, by comparing with satellite observations. To our knowledge, this is the first study that focused on the sub-grid performance of for land surface models. In the future research, continuous efforts are of importance in terms of a better representation of the integrated system of land use/land cover change (especially urban heat mitigation strategies involving the land use/ land cover change), hydrology, and climate, using the RCMs and/or the coupled RCMs and chemical transport models. I am particularly interested in regions/cases where precipitation is sensitive to land use/ land cover change, through the response of clouds (especially warm clouds). For example, in some areas, their local/regional precipitation and clouds can be very sensitive

to land surface albedo during the summer time, and can be significantly depressed due to the increase of surface albedo. As a result, though mitigation strategies by increasing surface albedos may be effective in the short-term, these areas may bear a risk of drought in the long-term, which may even finally lead to the failure of mitigation strategies due to significant depress of latent heat. The model improvement from two aspects is of particular interest. On one hand, continuous effort is needed to improve the modeled land surface fluxes at the grid level. As the S-Noah approach developed in this study, the grid-level fluxes are aggregated by averaging the sub-grid fluxes weighted by land use fractions. Such aggregation approach may be over-simplified, as study indicated that the spatial patterns of the surface heterogeneity at the sub-grid level may also affect the aggregated fluxes at the grid level, especially for the sensible and latent heat [81]. Hence, it would be of interest if a parameterization can be developed and applied to S-Noah to take into account the spatial patterns of sub-grid surface heterogeneity. The parameter can be estimated using a series of simulations by large eddy simulations (LES) under different conditions of atmospheric stability. On the hand, it is essential to improve the model representation in the sub-grid cloud diagnose by taking into account the sub-grid land surface heterogeneity when RCM simulation are conducted at the spatial resolutions too coarse to resolve the clouds (e.g. larger than 3km). For example, within PBL, the probability density function of vertical velocity can be linked to the sub-grid heterogeneity through roughness, sensible heat flux and etc. In addition, if the sub-grid heat and momentum fluxes are not fully mixed until blending height is reached, it may affect the entrainment and detrainment rate of cloud parcels during the convection.

Last, this study investigated the contribution of biomass burning aerosols to the regional climate of the southeastern U.S., using the coupled WRF-CMAQ model. It is found that though aerosols from all emission sources do affect the regional climate, biomass burning aerosols contribute little to the change in regional climate, in terms of the ensemble average over the southeastern U.S. However, the conclusions drawn are

subject to change as the current WRF-CMAQ model is limited by the model representation from the following aspects, which are to be improved in the future: 1) to include the optical properties of brown carbon, and their aging and the corresponding change in the optical properties; 2) to include the cloud absorption of radiation due to the absorbing aerosols within the hydrometeor particles and the interstitial particles between the hydrometeor particles within the clouds; 3) to include the burning heat flux at the land surface due to the biomass burning events.

REFERENCES

[1] Lim, S.S., et al. (2012), A comparative risk assessment of burden of disease and injury attributable to 67 risk factors and risk factor clusters in 21 regions, 1990–2010: a systematic analysis for the Global Burden of Disease Study 2010, Lancet, 380, 2224–2260

[2] IPCC (2007), Climate Change 2007: The physical science basis, in Contribution of the Working Group I to the Fourth Assessment Report of the Intergovernmental Panel on Climate Change, edited by S. Solomon, D. Qin, M. Manning, Z. Chen, M. Marquis, K. B. Averyt, M. Tignor, and H. L. Miller, Cambridge University Press, Cambridge.

[3] Hogrefe, C., Lynn, B., Civerolo, K., et al.(2004), Simulation changes in regional air pollution over the eastern United States due to changes in global and regional climate and emissions, J. Geophys. Res., 109, D22301

[4] Murazaki, K., Hess, P. (2006), How does climate change contribute to surface ozone change over the United States? J. Geophys. Res.: Atmos., 111 (D5) D05301

[5] Jacobson, M. Z. (2008), On the causal link between carbon dioxide and air pollution mortality Geophys. Res. Lett., 35 (3), L03809

[6] Lin, J.-T., Patten, K. O., Hayhoe, K., Liang, X.-Z., and Wuebbles, D. J. (2008), Effects of Future Climate and Biogenic Emissions Changes on Surface Ozone over the United States and China J. Appl. Meteorol. Climatol., 47 (7), 1888– 1909

[7] Nolte, C. G., Gilliland, A. B., Hogrefe, C., and Mickley, L. J. (2008), Linking global to regional models to assess future climate impacts on surface ozone levels in the United States J. Geophys. Res.: Atmos., 113 (D14), D14307

[8] Wu, S., Mickley, L. J., Jacob, D. J., Rind, D., and Streets, D. G. (2008), Effects of 2000–2050 changes in climate and emissions on global tropospheric ozone and the policy-relevant background surface ozone in the United States J. Geophys. Res.: Atmos., 113 (D18), D18312

[9] Tagaris, E. (2009), Potential Impact of Climate Change on Air Pollution-Related Human Health Effects Environ. Sci. Technol., 43 (13), 4979– 4988

[10] Weaver, C. P., et al. (2009), A Preliminary Synthesis of Modeled Climate Change Impacts on U.S. Regional Ozone Concentrations. Bull. Amer. Meteor. Soc., 90, 1843–1863

[11] Dawson, J. P., Bloomer, B. J., Winner, D. A., and Weaver, C. P. (2013), Understanding the Meteorological Drivers of U.S. Particulate Matter Concentrations in a Changing Climate Bull. Am. Meteorol. Soc., 95 (4), 521– 532

[12] Fu, T-M., Zheng, Y., Paulot, F., Mao, J., and Yabtosca, R. M. (2015), Positive but variable sensitivity of August surface ozone to large-scale warming in the southeast United States. Nature Climate Change, 5,454–458

[13] Jacobson, M.Z., Seinfeld, J.H., Carmichael, G. R., and Streets, D. G. (2004),The effect on photochemical smog of converting the US fleet of gasoline vehicles to modern diesel vehicles. Geophys. Res. Lett., 31(2), L02116

[14] Skamarock, W. C., Klemp, J., Dudhia, J., Gill, D. O., Barker, D. M., Duda, M. G., Huang, X. Y., Wang, W., and Powers, J. G. (2008), A Description of the Advanced Research WRF Version 3, NCAR Technical note NCARTN-475+STR

[15] Houyoux, M., R. and Vukovich, J. M. (1999), Updates to the Sparse Matrix Operator Kernel Emissions (SMOKE) Modeling System and Integration with Models-3. in The Emission Inventory: Regional Strategies for the Future,. Raleigh, NC

[16] Byun, D. and Schere, K. (2006), Review of the Governing Equations, Computational Algorithms, and Other Components of the Models-3 Community Multiscale Air Quality (CMAQ) Modeling System. Applied Mechanics Reviews, 59(2), 51-77

[17] Yang, Y.J., Wilkinson, J.G., and Russell, A.G. (1997), Fast direct sensitivity analysis of multidimensional photochemical models. Environ. Sci. Technol., 31(10), 2859-2868.

[18] Napelenok, S., Cohan, D. S., Hu, Y., et al. (2006), Decoupled Direct 3D Sensitivity Analysis for Particulate Matter. Atmospheric Environment, 40, 6112-6121

[19] Zhang, W., Capps, S. L., Hu, Y., Nenes, A., Napelenok, S. L., and Russell, A. G. (2012), Development of the high-order decoupled direct method in three dimensions for particulate matter: enabling advanced sensitivity analysis in air quality models, Geosci. Model Dev., 5, 355-368

[20] Hakami, A., Henze, D. K., Seinfeld, J. H., Singh, K., Sandu, A., Kim, S., Byun, D., and Li, Q. (2007), The adjoint of CMAQ. Environ. Sci. Technol., 41, 7807– 17

[21] Capps, S. L., Henze, D. K., Hakami, A., Russell, A. G., and Nenes, A. (2012), ANISORROPIA: the adjoint of the aerosol thermodynamic model ISORROPIA, Atmos. Chem. Phys., 12, 527-543

[22] van Vuuren, D. P., Lucas, P. L., and Hilderink, H. (2007), Downscaling drivers of global environmental change: Enabling use of global SRES scenarios at the national and grid levels Global Environ. Change, 17, 114– 130

[23] Meehl, G. A., Stocker, T. F., Collins, W. D., Friedlingstein, P., Gaye, A. T., Gregory, J. M., Kitoh, A., Knutti, R., Murphy, J. M., Noda, A., Raper, S. C. B., Watterson, I. G., Weaver, A. J., and Zhao, Z. C. (2007), Global climate projections, in Climate Change 2007: The Physical Science Basis — Contribution of Working Group Ⅰ to the Fourth Assessment Report of the Inter-governmental Panel on Climate Change, pp. 747-845, Cambridge Univ. Press, Cambridge, U.K

[24] Houghton, J. T., and Ding, Y., Griggs, D. J., Noguer, M., van der Linden, P. J., Dai, X., Maskell, K., and Johnson, C. A. (2001), in Climate Change 2001: the Science Basis, pp. 944, Cambridge Univ. Press, Cambridge, U.K

[25] Castro, C. L., Pielke Sr., R. A., and Leoncini, G. (2005), Dynamical downscaling: Assessment of value retained and added using the Regional Atmospheric Modeling System (RAMS), J. Geophys. Res., 110, D05108

[26] Pielke, R. A., Wilby, R., Niyogi, D., Hossain, F., Dairuku, K., Adegoke, J., Kallos, G., Seastedt, T., and Suding, K. (2012), Dealing with Complexity and Extreme Events Using a Bottom-Up, Resource-Based Vulnerability Perspective, in Extreme Events and Natural Hazards: The Complexity Perspective (eds A. S. Sharma, A. Bunde, V. P. Dimri and D. N. Baker), American Geophysical Union, Washington, D. C..

[27] Denis, B., Laprise, R., Caya, D., and Cote, J. (2002), Downscaling ability of one-way nested regional climate models: the Big-Brother Experiment, Climate Dynamics, 18,627-646

[28] Leung L.R., Qian, Y., Bian, X., Washington, W.M., Han, J., and Roads, J. (2004) Mid-century ensemble regional climate change scenarios for the western United States. Clim Change 62(1–3), 75–113

[29] Liang, X.-Z., Pan, J., Zhu, J., Kunkel, K. E., Wang, J. X. L., and Dai, A. (2006), Regional climate model downscaling of the U.S. summer climate and future change, J. Geophys. Res., 111, D10108

[30] Pal, J.S., Giorgi, F., Bi, X., et al. (2007), Regional Climate Modeling for the Developing World: The ICTP RegCM3 and RegCNET. Bull. Amer. Meteor. Soc., 88, 1395–1409.

[31] Gustafson Jr. W. I., and Leung, R. L. (2007), Regional Downscaling for Air Quality Assessment. Bull. Amer. Meteor. Soc., 88, 1215–1227

[32]Lo, J. C.-F., Yang, Z.-L. , and Pielke Sr., R. A. (2008), Assessment of three dynamical climate downscaling methods using the Weather Research and Forecasting (WRF) model, J. Geophys. Res., 113, D09112

[33] Warner, T. T., Peterson, R. A., and Treadon, R. E. (1997), A tutorial on lateral boundary conditions as a basic and potential serious limitation to regional numerical weather prediction, Bull. Am. Meteorol. Soc., 78, 2599-2617

[34] Giorgi, F., and Mearns L. O. (1999), Introduction to special section: regional climate modeling revisited, J. Geophys. Res., 104, D6

[35] Jacobson, M. Z. (2002), Atmospheric Pollution: History, Sciences and Regulation. Cambridge University Press, New York, ISBN 0521010446, 399 pp.

[36] Jacob, D.J., and Winner, D. A. (2009), Effect of climate change on air quality, Atmospheric Environment, 43, 51-63

[37] Wong, D. C., Pleim, J., Mathur, R., Binkowski, F., Otte, T., Gilliam, R., Pouliot, G., Xiu, A., Young, J. O., and Kang, D. (2012), WRF-CMAQ two-way coupled system

with aerosol feedback: software development and preliminary results, Geosci. Model Dev., 5, 299-312

[38] Fishbone, L.G., Hill, D., and Sailor, V. L. (1980), MARKAL, a Multiperiod Linear-Programming Model for Energy-Systems Analysis Applied to the United-States. Bulletin of the American Physical Society, 25(4), 494-495

[39] Rathnagel, S. and Stocks, K. (1982), Energy Modeling for Technology-Assessment - the MARKAL Approach. Omega-International Journal of Management Science,10(5), 493-505

[40] Bin, S. and Dowlatabadi, H.(2005), Consumer lifestyle approach to US energy use and the related CO2 emissions. Energy Policy, 33(2), 197-208

[41] Schafer, A., and Jacoby, H. D. (2006), Vehicle technology under CO2 constraint: a general equilibrium analysis. Energy Policy, 34(9), 975-985

[42] EPA, (2008), Regulating Greenhouse Gas Emisssions under the Clean Air Act, ANPR,. US EPA: Washington, DC

[43] Dixon, P.G., and Mote, T. L. (2003), Patterns and causes of Atlanta's urban heat island-initiated precipitation, Journal of Applied Meteorology, 42 (9), 1273–1284

[44] Christy, J. R., Norris, W. B., Redmond, K., and Gallo, K. P. (2006), Methodology and results of calculating central California surface temperature trends: Evidence of human-induced climate change? Journal of Climate, 19 (4), 548–563

[45] Kueppers, L. M., Snyder, M. A., and Sloan, L. C. (2007), Irrigation cooling effect: Regional climate forcing by land-use change, Geophysical Research Letters, 34(3), L03703

[46] Ashley, W. S., Bentley, M. L., and Stallins, J. A. (2012), Urban-induced thunderstorm modification in the Southeast United States, Climatic Change, 113(2), 481–498

[47] Pan, H. L., and Mahrt, L. (1987), Interaction between soil hydrology and boundary layer development, Boundary-Layer Meteorology, 38 (1-2), 185–202

[48] Dickinson, R. E., Errico, R. M., Giorgi, F., and Bates, G. T. (1989), A regional climate model for the western United States, Climate Change, 15, 383-422

[49] Davies, H. C. (1976), A lateral boundary formulation for multi-level prediction models, Quart. J. Roy. Meteor. Soc., 102, 405–418

[50] Davies, H. C. (1983), Limitations of some common lateral boundary schemes used in regional NWP models, Mon. Weather Rev., 111, 1002–1012

[51] Stauffer, D. R., and Seaman, N. L. (1990), Use of four-dimensional data assimilation in a limited-area mesoscale model, Part I: Experiments with synoptic-scale data, Mon. Weather Rev., 118, 1250-1277

[52] Waldron, K. M., Paegle, J., and Horel, J. D. (1996), Sensitivity of a spectrally filtered and nudged limited-area model to outer model options, Mon. Weather. Rev., 124, 529-547

[53] von Storch, H., Langenberg, H., and Feser, F. (2000), A spectral nudging technique for dynamical downscaling purposes, Mon. Weather. Rev., 128, 3664-3673

[54] Miguez-Macho, G. (2004), Spectral nudging to eliminate the effects of domain position and geometry in regional climate model simulations. J. Geophys. Res.-Atmos.,109, D13104

[55] Miguez-Macho, G. (2005), Regional climate simulations over North America: Interaction of local processes with improved large-scale flow. Journal of Climate, 18(8), 1227-1246

[56] Leung, L. R., and Gustafson, W. I. (2005), Potential regional climate change and implications to US air quality, Geophys. Res. Lett., 32, L16711

[57] Forkel, R., and Knoche, R. (2006), Regional climate change and its impact on photooxidant concentrations in southern Germany: Simulation with a coupled regional climate-chemistry model, J. Geophys. Res., 111, D12302

[58] Steiner, A. L., Tonse, S., Cohen, R. C., Goldstein, A. H., and Harley, R. A. (2006), Influence of future climate and emissions on regional air quality in California, Geophys. Res., 111, D18303

[59] Tagaris, E., Liao, K.-J., Manomaiphiboon, K., He, S., Woo, J.-H., Amar, P., and Russell, A. G. (2008), The role of climate and emission changes in future air quality over southern Canada and northern Mexico, Atmos. Chem. Phys., 8, 3973-3983

[60] Feser, F., and von Storch, H. (2005), A spatial two-dimensional discrete filter for limited area model evaluation purposes, Mon. Weather Rev.,133, 1774-1786

[61] Feser, F. (2006), Enhanced detectability of added value in limited area model results separated into different spatial scales, Mon. Wea. Rev., 134, 2180-2190

[62] Rockel, B., Castro, C. L., Pielke Sr., R. A., von Storch, H., and Leoncini, G. (2008), Dynamical downscaling: Assessment of model system dependent retained and added variability for two different regional climate models, J. Geophys. Res.,113, D21107

[63] Winterfeldt, J., and Weisse, R. (2009), Assessment of value added for surface marine wind speed obtained from two regional climate models, Mon. Weather Rev., 137, 2955-2965

[64] Feser, F., Rockel, B., von Storch, H., Winterfeldt, J., and Zahn, M. (2011), Regional climate models add value, Bull. Amer. Meteor. Soc. 92, 1181–1192

[65] Stauffer, D.R., Seaman, N. L., and Binkowski, F. S. (1991), Use of four-dimensional data assimilation in a limited-area mesoscale model: Part II: effects of data assimilation within the planetary boundary layer, Mon. Wea. Rev., 119 , 734-754

[66] Seaman, N. L., Stauffer, D.R., and Lario-Gibbs, A. M. (1995), A multi-scale four-dimensional data assimilation system applied in the San Joaquin valley during SARMAP: Part I: Modeling design and basic performance characteristics, J. Appl. Meteor., 34, 1739-1761

[67] Mesinger, F., DiMego, G., Kalnay, E., Mitchell, K., Shafran, P. C., Ebisuzaki, W., Jovic, D., Woollen, J., Rogers, E., Berbery, E. H., Ek, M. B., Fan, Y., Grumbine, R., Higgins, W., Li, H., Lin, Y., Manikin, G., Parrish, D., and Shi, W. (2006), North American regional reanalysis, Bull. Am. Meteorol. Soc., 87, 343-360

[68] Mahmood, R., Foster, S. A. , Keeling, T., Hubbar, K. G. , Carlson, C., and Leeper, R. (2006), Impacts of irrigation on 20th Century temperatures in the Northern Great Plains, Global Planet Change, 54 (1-2),1–18

[69] Lobell, D. B., and Bonfils, C. (2008), The effect of irrigation on regional temperatures: a spatial and temporal analysis of trends in California, 1934–2002, Journal of Climate, 21(10), 2063–2071

[70] Hand, L. M., and Shepherd, J. M. (2009), An investigation of warm season spatial rainfall variability in Oklahoma City: possible linkages to urbanization and prevailing wind, Journal of Applied Meteorology and Climatology, 48(2), 251–269

[71] Kalnay, E., and Cai, M. (2003), Impact of urbanization and land use on climate change, Nature, 423(6953), 528–531

[72] Trenberth, K. E. (2004), Rural land-use change and climate, Nature, 427, 213

[73] Fall, S., Niyogi, D., Gluhovsky, A., Pielke, R. A., Kalnay, E., and Rochon, G. (2009), Impacts of land use land cover on temperature trends over the continental United States: assessment using the North American Regional Reanalysis, International Journal of Climatology, 30 (13), 1980–1993

[74] Scheitlin, K. N., and Dixon, P. G. (2010), Diurnal temperature range variability due to land cover and airmass types in the southeast, Journal of Applied Meteorology and Climatology, 49(5), 879–888

[75] Vose, R. S., Karl, T. R. , Easterling, D. R. , Williams, C. N., and Menne, M. J. (2004), Comment on 'Impact of land-use change on climate', Nature, 427(6971), 213–214

[76] Bonfils, C., Duffy, P. B. and Lobell, D. B. (2006), Comment on 'Methodology and results of calculating Central California surface temperature trends: evidence of a human-induced climate change?', Journal of Climate, 20(17),4486–4489

[77] Diffenbaugh, N. S. (2009), Influence of modern land cover on the climate of the United States, Climate Dynamics, 33(7), 945–958

[78] Jin, J., and Miller, N. L. (2011), Regional simulations to quantify land use change and irrigation impacts on hydroclimate in the California Central Valley, Theoretical and Applied Climatology, 104 (3), 429–442

[79] Chase, T. N., Pielke Sr., R. A. , Kittel, T. G. F. , Nemani, R. R. and Running, S. W. (2000), Simulated impacts of historical land cover changes on global climate in northern winter, Climate Dynamics, 16(2), 93–105

[80] Feddema, J. J., Oleson, K.W. , Bonan, G. B. , Mearns, L. O. , Buja, L. E. , Meehl, G. A. , and Washington, W. M. (2005), The importance of land-cover change in simulating future climates, Science, 310, 1674–1678

[81] Hu, Z., and Islam, S. (1997), Effects of spatial variability on the scaling of land surface parametrisations, Boundary-Layer Meteorol, 83, 441–461

[82] Weaver, C. P., and Avissar, R. (2001), Atmospheric Disturbances Caused by Human Modification of the Landscape, Bull. Amer. Meteor. Soc., 82, 269–281

[83] Mahmood, R., et al. (2010), Impacts of land use/land cover change on climate and future research priorities, Bulletin of the American Meteorological Society, 91(1), 37–46

[84] Hogue, T. S., Bastidas, L. A. , Gupta, H. V. , and Sorooshian, S. (2006), Evaluating model performance and parameter behavior for varying levels of land surface model complexity, Water Resources Research, 42(8), W08430

[85] De Haan, L. L., Kanamitsu, M., Lu, C.-H., and Roads, J. O. (2007), A comparison of the Noah and OSU land surface models in the ECPC seasonal forecast model, Journal of Hydrometeorology, 8(5), 1031–1048

[86] Miao, J.-F., Chen, D., and Borne, K. (2007), Evaluation and comparison of Noah and Pleim–Xiu land surface models in MM5 using GÖTE2001 data: spatial and temporal variations in near-surface air temperature, Journal of Applied Meteorology and Climatology, 46(10), 1587–1605

[87] Ruane, A. C., and Roads, J. O. (2008), Diurnal to annual precipitation sensitivity to convective and land surface schemes, Earth Interactions, 12, 1–13

[88] Sridhar, V. , Elliott, R. L. Chen, F., and Brotzge, J. A. (2002), Validation of the NOAH-OSU land surface model using surface flux measurements in Oklahoma, Journal of Geophysical Research-Atmospheres, 107(D20), 4418

[89] Chen, F., Yates, D. N. , Nagai, H., LeMone, M. A. , Ikeda, K., and Grossman, R. L. (2003), Land surface heterogeneity in the Cooperative Atmosphere Surface Exchange Study (CASES-97). Part I: Comparing model surface flux maps with surfaceflux tower and aircraft measurements, Journal of Hydrometeorology, 4(2), 196–218

[90] LeMone, M. A., Tewari, M., Chen, F., Alfieri, J. G., and Niyogi, D. (2008), Evaluation of the Noah land surface model using data from a Fair-Weather IHOP_2002 day with heterogeneous surface fluxes, Monthly Weather Review, 136(12), 4915–4941

[91] Radell, D. B., and Rowe, C. M. (2008), An observational analysis and evaluation of land surface model accuracy in the Nebraska Sand Hills, Journal of Hydrometeorology, 9(4), 601–621

[92] Xia, Y. L., Ek, M., Sheffield, J., Livneh, B., Huang, M. Y. , Wei, H. L., Feng, S., Luo, L. F. , Meng, J., and Wood, E. (2013), Validation of Noah-simulated soil temperature in the North American Land Data Assimilation System Phase 2, Journal of Applied Meteorology and Climatology, 52(2), 455–471

[93] Gago, E. J., Roldan, J., Pacheco-Torres, R., and Ordóñez, J. (2013), The city and urban heat islands: A review of strategies to mitigate adverse effects, Renewable and Sustainable Energy Reviews, 25, 749-758

[94] Trusilova, K., Jung, M., Churkina, G., Karstens, U., Heimann, M, and Claussen, M. (2008), Urbanization impacts on the climate in Europe: numerical experiments by the PSU–NCAR Mesoscale Model (MM5), Journal of Applied Meteorology and Climatology, 47(5), 1442–1455

[95] Georgescu, M., Moustaoui, M., Mahalov, A., and Dudhia, J. (2011), An alternative explanation of the semiarid urban area “oasis effect”, Journal of Geophysical Research-Atmospheres, 116, D24113

[96] Chen, H., Tian, H., Liu, M., Melillo, J., Pan, S., and Zhang, C. (2006), Effect of land-cover change on terrestrial carbon dynamics in the southern United States, Journal of Environmental Quality, 35 (4),1533-1547

[97] Bonan, G. B. (2001), Observational Evidence for Reduction of Daily Maximum Temperature by Croplands in the Midwest United States, Journal of Climate, 14(11), 2430–2442

[98] Matyas, C. J., and Carleton, A. M. (2010), Surface radar-derived convective rainfall associations with Midwest US land surface conditions in summer seasons 1999 and 2000, Theoretical and Applied Climatology, 99(3), 315–330

[99] Mishra, V., Cherkauer, K. A., Niyogi, D., Lei, M., Pijanowski, B. C., Ray, D. K. , Bowling, L. C., and Yang, G. X. (2010), A regional scale assessment of land use/land cover and climatic changes on water and energy cycle in the upper Midwest United States, International Journal of Climatology, 30(13), 2025–2044

[100] Snyder, P. K., Delire, C., and Foley, J. A. (2004), Evaluating the influence of different vegetation biomes on the global climate, Climate Dynamics, 23(3), 279–302

[101] McPherson, R. A. (2007), A review of vegetation–atmosphere interactions and their influences on mesoscale phenomena, Progress in Physical Geography, 31(3), 261–285

[102]Loridan, T., and Grimmond, C. S. B. (2012), Multi-site evaluation of an urban land-surface model: intra-urban heterogeneity, seasonality and parameter complexity requirements, Quarterly Journal of the Royal Meteorological Society, 138(665), 1094–1113

[103] Li, D., Bou-Zeid, E., Barlage, M., Chen, F., and Smith, J. A. (2013), Development and evaluation of a mosaic approach in the WRF-Noah framework, Journal of Geophysical Research-Atmospheres, 118, 11918–11935

[104] Rieck, M., Hohenegger, C., and van Heerwaarden, C. C. (2014), The Influence of Land Surface Heterogeneities on Cloud Size Development, Mon. Wea. Rev., 142, 3830–3846

[105] Myneni, R. B., Hoffman, S., Knyazikhin, Y., Privette, J. L. , Glassy, J., Tian, Y., and et al. (2002), Global products of vegetation leaf area and fraction absorbed PAR from year one of MODIS data, Remote Sensing of Environment, 83, 214–231

[106] Zeng, X. B., Dickinson, R. E. , Walker, A., Shaikh, M., DeFries, R. S., and Qi, J. G. (2000), Derivation and evaluation of global 1-km fractional vegetation cover data for land modeling, Journal of Applied Meteorology, 39(6), 826-839

[107] Miller, J., Barlage, M., Zeng, X.B. , Wei, H. L. , Mitchell, K, and Tarpley, D (2006), Sensitivity of the NCEP/Noah land surface model to the MODIS green vegetation fraction data set, Geophysical Research Letters, 33(13), L13404

[108] White-Newsome, J. L., Brines, S. J., Brown, D. G. , Dvonch, J. T. , Gronlund, C. J. , Zhang, K., Oswald, E. M. , and O'Neill, M. S. (2013), Validating Satellite-Derived Land Surface Temperature with in Situ Measurements: A Public Health Perspective, Environmental Health Perspectives, 121, 925–931

[109] Norman, J. M., and Becker, F. (1995), Terminology in thermal infrared remote sensing of natural surfaces, Agricultural and Forest Meteorology, 77,153–166

[110] Wan, Z. M., and Li, Z. L. (2008), Radiance-based validation of the V5 MODIS land-surface temperature product, International Journal of Remote Sensing, 29(17), 5373-5395

[111] Coll, C., Wan, Z. M. , and Galve, J. M. (2009), Temperature-based and radiance-based validations of the V5 MODIS land surface temperature product, Journal of Geophysical Research-Atmospheres, 114, D20102

[112] Masuoka, E., Fleig, A., Wolfe, R. E. , and Patt, F. (1998), Key characteristics of MODIS data products, IEEE Transactions on Geoscience and Remote Sensing, 36(4), 1313−1323

[113] Snyder, W. C., Wan, Z. M. , Zhang, Y., and Feng, Y. Z. (1998), Classification-based emissivity for land surface temperature measurement from space, International Journal of Remote Sensing, 19(14), 2753–2774

[114] Homer, C., Dewitz, J., Fry, J., Coan, M., Hossain, N., Larson, C., Herold, N., McKerrow, A., Van Driel, J., N., and Wickham, J. (2007), Completion of the 2001 National Land Cover Database for the Conterminous United States, Photogrammetric Engineering and Remote Sensing, 73(4), 337-341

[115] Rigo, G., Parlow, E., and Oesch, D. (2006),Validation of satellite observed thermal emission with in-situ measurements over an urban surface, Remote Sensing of Environment, 104(2), 201-210

[116] Wang, K. C., and Liang, S. L. (2009), Evaluation of ASTER and MODIS land surface temperature and emissivity products using long-term surface longwave

radiation observations at SURFRAD sites, Remote Sensing of Environment, 113(7), 1556-1565

[117] Vivoni, E. R., Moreno, H. A. , Mascaro, G., Rodríguez, J. C. , Watts, C. J. , Garatuza-Payan, J., and Scott, R. L. (2008), Observed relation between evapotranspiration and soil moisture in the North American monsoon region, Geophysical Research Letters, 35(22), L22403

[118] Voogt, J. A., and Oke, T. R. (2003), Thermal remote sensing of urban climates, Remote Sensing of Environment, 86(3), 370–384

[119] Avissar, R., and Schmidt, T. (1998), An Evaluation of the Scale at which Ground-Surface Heat Flux Patchiness Affects the Convective Boundary Layer Using Large-Eddy Simulations, Journal of the Atmospheric Sciences, 55, 2666–2689

[120] Roy, S. B., Weaver, C. P. , Nolan, D. S. , and Avissar, R. (2003), A preferred scale for landscape forced mesoscale circulations? Journal of Geophysical Research-Atmospheres, 108(D22), 8854

[121] Baldocchi, D. D., and Rao, K. S. (1995), Intra-field variability of scalar flux densities across a transition between a desert and an irrigated potato field, Boundary-Layer Meteorology, 76, 109-136

[122] Tomlinson, C. J., Chapman, L., Thornes, J. E. , and Baker, C. J. (2011), Remote sensing land surface temperature for meteorology and climatology: a review, Meteorological Application, 18(3), 296–306

[123] Xu, S. L. (2009), An approach to analyzing the intensity of the daytime surface urban heat island effect at a local scale, Environmental Monitoring and Assessment, 151, 289-300

[124] Zakšek, K., and Oštir, K. (2012), Downscaling land surface temperature for urban heat island diurnal cycle analysis, Remote Sensing of Environment, 117,114–124

[125] Roth, M., Oke, T. R., and Emery, W. J. (1989), Satellite-derived urban heat islands from three coastal cities and the utilization of such data in urban climatology, International Journal of Remote Sensing, 10(11), 1699-1720

[126] Zhou, J., Chen, Y. H., Zhang, X., and Zhan, W. F. (2013), Modelling the diurnal variations of urban heat islands with multi-source satellite data, International Journal of Remote Sensing, 34(21), 7568-7588

[127] Carnahan, W. H., and Larson, R. C. (1990), An analysis of an urban heat sink, Remote Sensing of Environment, 33(1), 65–71

[128] Peňa, M. (2008), Relationships between remotely sensed surface parameters associated with the urban heat sink formation in Santiago, Chile, International Journal of Remote Sensing, 29(15), 4385–404

[129] Clinton, N., and Gong, P. (2013), MODIS detected surface urban heat islands and sinks: Global locations and controls, Remote Sensing of Environment, 134, 294-304

[130] Wan, Z.M. (2014), New refinements and validation of the collection-6 MODIS land-surface temperature/emissivity product, Remote Sensing of Environment, 140, 36-45

[131] Pu, R. L., Gong, P., Michishita, R., and Sasagawa, T. (2006), Assessment of multi-resolution and multi-sensor data for urban temperature retrieval, Remote Sensing of Environment, 104(2), 211-225

[132] Stone, B. Jr, Vargo, J., Liu, P., Habeeb, D., DeLucia, A., Trail, M., Hu, Y., and Russell, A. G.(2014), Avoided Heat-Related Mortality through Climate Adaptation Strategies in Three US Cities, PLoS ONE 9(6), e100852

[133] Anderson, G. B., Dominici, F., Wang, Y., McCormack, M. C., Bell, M. L., and Peng, R. D. (2013), Heat-related emergency hospitalizations for respiratory diseases in the Medicare population. American Journal of Respiratory and Critical Care Medicine, 187, 1098–1103

[134] Gronlund, C. J., Zanobetti, A., Schwartz, J. D., Wellenius, G. A., and O'Neill, M. S. (2014), Heat, heat waves, and hospital admissions among the elderly in the United States, 1992–2006. Environmental Health Perspectives, 122, 1187–1192

[135] Gosling, S., Lowe, J., McGregor, G., Pelling, M., and Malamud, B. (2009), Associations between elevated atmospheric temperature and human mortality: a critical review of the literature. Climatic Change, 92, 299–341

[136] Anderson, G. B., and Bell, M. L. (2009), Weather-related mortality: a study of how heat, cold, and heat waves affect mortality in the United States. Epidemiology, 20, 205–213.

[137] Hajat, S., and Kosatsky, T. (2010), Heat-related mortality: a review and exploration of heterogeneity. J Epidemiol Community Health, 64, 753–760

[138] Georgescu, M., Morefield, P. E., Bierwagen, B. G., and Weaver, C. P. (2014), Urban adaptation can roll back warming of emerging megapolitan regions. Proc. Natl. Acad. Sci. (USA), 111, 2909–2914

[139] McCarthy, M., Best, M., Betts, R. (2010), Climate change in cities due to global warming and urban effects. Geophys Res Lett, 37, L09705

[140] Argüeso, D., Evans, J. P., Fita, L., Bormann, K. J. (2014), Temperature response to future urbanization and climate change. Climate Dynamics, 42, 2183 -2199

[141] Meehl, G. A., and Tebaldi, C. (2004), More intense, more frequent, and longer lasting heat waves in the 21st century. Science, 305, 994–997.

[142] Tebaldi, C., Hayhoe, K., Arblaster, J., and Meehl, G. (2006), Going to the extremes: An intercomparison of model-simulated historical and future changes in extreme events. Climatic Change, 79, 185–211

[143] Simolo, C., Brunetti, M., Maugeri, M., and Nanni, T. (2011), Evolution of extreme temperatures in a warming climate, Geophys. Res. Lett. 2011, 38, L16701

[144] Lau, N.-C., and Nath, M. J. (2012), A model study of heat waves over North America: Meteorological aspects and projections for the twenty-first century. J. Climate, 25, 4761–4784

[145] Li, D.; Bou-Zeid, E. (2013), Synergistic Interactions between Urban Heat Islands and Heat Waves: The Impact in Cities Is Larger than the Sum of Its Parts. J. Appl. Meteor. Climatol., 52, 2051–2064

[146] Cui, Y. Y., and de Foy., B (2012), Seasonal Variations of the Urban Heat Island at the Surface and the Near-Surface and Reductions due to Urban Vegetation in Mexico City. Journal of Applied Meteorology and Climatology, 51(5), 855-868

[147] Li D, Bou-Zeid, E., and Oppenheimer, M. (2014), The effectiveness of cool and green roofs as urban heat island mitigation strategies. Environmental Research Letters, 9, 055002

[148] Georgescu, M. (2015), Challenges Associated with Adaptation to Future Urban Expansion. J. Climate, 28, 2544–2563

[149] Santamouris, M. (2014) Cooling the cities – a review of reflective and green roof mitigation technologies to fight heat island and improve comfort in urban environments., Solar Energy, 103, 682–703

[150] Voorhees A, Fann N, Fulcher C, Dolwick P, Hubbell B, et al. (2011), Climate change-related temperature impacts on warm season heat mortality: A proof-of-concept methodology using BenMAP. Environ Sci Technol 45: 1450–1457

[151] Peng, R., Bobb, J., Tebaldi, C., McDaniel, L., Bell, M., et al. (2011), Toward a quantitative estimate of future heat wave wave mortality under global climate change. Environ Health Perspect, 119, 701–706

[152] Yang J, Wang Z. H., and Kaloush K. E. (2015) Environmental impacts of reflective materials: is high albedo a'Silver Bullet' for mitigating urban heat island? Renew. Sustainable Energy Rev., 47, 830–843

[153] Talbot C, Bou-Zeid, E., and Smith, J. (2012), Nested Mesoscale Large-Eddy Simulations with WRF: Performance in Real Test Cases. J. Hydrometeor, 13, 1421–1441

[154] Kusaka, H., Kondo, H., Kikegawa, Y., and Kimura, F. (2001), A simple single-layer urban canopy model for atmospheric models: Comparison with multi-layer and slab models, Boundary-Layer Meteorology, 101, 329–358

[155] Kusaka, H., and Kimura, F. (2004), Thermal effects of urban canyon structure on the nocturnal heat island: Numerical experiment using a mesoscale model coupled with an urban canopy model, Journal of Applied Meteorology, 43, 1899–1910

[156] Noh, Y., Cheon, W. G. , Hong, S. Y. , and Raasch, S. (2003), Improvement of the K-profile model for the planetary boundary layer based on large eddy simulation data. Bound.-Layer Meteor., 107, 401–427

[157] Hong, S. Y., Noh, Y., and Dudhia, J. (2006), A new vertical diffusion package with an explicit treatment of entrainment processes. Mon. Wea. Rev., 134, 2318–2341

[158] Shin, H., and Hong, S.-Y. (2011), Intercomparison of planetary boundary-layer parametrizations in theWRF model for a single day from CASES-99, Bound.-Layer Meteor., 139, 261–281

[159] Gu, H., Jin, J., Wu, Y., Ek, M., and Subin, Z. (2015), Calibration and validation of lake surface temperature simulations with the coupled WRF-lake model, Clim. Chang., 129, 471–483

[160] Meteorological Development Laboratory/Office of Science and Technology/National Weather Service/NOAA/U.S. Department of Commerce (1987), TDL U.S. and Canada Surface Hourly Observations, daily from December 1976 to present, http://rda.ucar.edu/datasets/ds472.0/, Research Data Archive at the National Center for Atmospheric Research, Computational and Information Systems Laboratory, Boulder, Colo.

[161] Horvath, K., Koracin, D., Vellore, R., Jiang, J., and Belu, R. (2012), Sub-kilometer dynamical downscaling of near-surface winds in complex terrain using WRF and MM5 mesoscale models. J. Geophys. Res., 117, D11111

[162] Mellor, G. L., Yamada, T. (1982), Development of a turbulence closure model for geophysical fluid problems. Reviews of Geophysics, 20, 851–875

[163] Janjic, Z. I. (2002), Nonsingular implementation of the Mellor–Yamada level 2.5 scheme in the NCEP Meso model, NCEP Office Note, 437, 1–61

[164] Wang, Z.-H., Bou-Zeid, E., Au, S. K., and Smith, J. A. (2011), Analyzing the Sensitivity of WRF's Single-Layer Urban Canopy Model to Parameter Uncertainty Using Advanced Monte Carlo Simulation. J. Appl. Meteor. Climatol., 50, 1795–1814

[165] Botham-Myint, D., Gerald, W. R., and Sailor, D. J. (2015) Thermal footprint effect of rooftop urban cooling strategies Urban Climate

[166] Krayenhoff, E. S., and Voogt, J. A. (2010), Impacts of Urban Albedo Increase on Local Air Temperature at Daily–Annual Time Scales: Model Results and Synthesis of Previous Work. J. Appl. Meteor. Climatol., 49, 1634–1648

[167] Jacobson, M. Z., and Ten Hoeve, J. E. (2012), Effects of Urban Surfaces and White Roofs on Global and Regional Climate. J. Climate, 25, 1028–104

[168] Georgescu, M., Mahalov, A., and Moustaoui, M. (2012), Seasonal hydroclimatic impacts of Sun Corridor expansion, Environ. Res. Lett., 7, 1–9

[169] Wang, Z.-H., Bou-Zeid, E., Au, S. K., and Smith, J. A. (2011), Analyzing the Sensitivity of WRF's Single-Layer Urban Canopy Model to Parameter Uncertainty Using Advanced Monte Carlo Simulation. J. Appl. Meteor. Climatol., 50, 1795–1814

[170] Fan, J., Rosenfeld, D., Yang, Y., Zhao, C., Leung, L. R., and Li, Z. (2015), Substantial contribution of anthropogenic air pollution to catastrophic floods in Southwest China, Geophys. Res. Lett., 42, 6066–6075

[171] Salzmann, M., Weser, H., and Cherian, R. (2014), Robust response of Asian summer monsoon to anthropogenic aerosols in CMIP5 models, J. Geophys. Res. Atmos., 119, 11321–11337

[172] Wang, T. J., Zhuang, B. L., Li, S. , Liu, J., Xie, M., Yin, C. Q. , Zhang, Y., Yuan, C., Zhu, J. L., Ji, L. Q., and Han,Y. (2015), The interactions between anthropogenic aerosols and the East Asian summer monsoon using RegCCMS, J. Geophys. Res. Atmos., 120, 5602–5621

[173] Boo, K.-O., Booth, B. B. B ., Byun, Y.-H. , Lee, J., Cho, C. H. , Shim, S., and Kim, K.-T. (2015), Influence of aerosols in multidecadal SST variability simulations over the North Pacific, J. Geophys. Res. Atmos., 120, 517–531.

[174] Zhang, X., Kondragunta, S., and Roy, D. P. (2014), Interannual variation in biomass burning and fire seasonality derived from geostationary satellite data across the contiguous United States from 1995 to 2011, J. Geophys. Res. Biogeosci., 119, 1147–1162

[175] Zheng, M., Cass, G. R., Schauer, J. J., and Edgerton, E. S. (2002), Source apportionment of PM2.5 in the southeastern United States using solvent-extractable organic compounds as tracers, Environ. Sci. Technol., 36(11), 2361–2371

[176] Marmur, A., Park, S.-K., Mulholland, J. A., Tolbert, P. E., and Russell, A. G. (2006), Source apportionment of PM2.5 in the southeastern United States using

receptor and emission-based models, Conceptual differences and implications for time-series health studies Atmos. Environ., 40, 2533– 2551

[177] Tian, D., Hu, Y. T., Wang, Y. H., Boylan, J. W., Zheng, M., and Russell, A. G. (2009), Assessment of biomass burning emissions and their impacts on urban and regional PM2.5: A Georgia case study, Environ. Sci. Technol., 43(2), 299–305

[178] Zhang, X., Hecobian, A., Zheng, M., Frank, N. H., and Weber, R. J. (2010), Biomass burning impact on PM 2.5 over the southeastern US during 2007: integrating chemically speciated FRM filter measurements, MODIS fire counts and PMF analysis, Atmos. Chem. Phys., 10, 6839-6853

[179] Ford, B., and Heald, C. L. (2013), Aerosol loading in the Southeastern United States: Reconciling surface and satellite observations, Atmos. Chem. Phys., 13(18), 9269–9283.

[180] Verma, V., Fang, T., Guo, H., King, L., Bates, J. T., Peltier, R. E., Edgerton, E., Russell, A. G., and Weber, R. J. (2014), Reactive oxygen species associated with water-soluble PM2.5 in the southeastern United States: spatiotemporal trends and source apportionment, Atmos. Chem. Phys., 14, 12915-12930

[181] Hodnebrog, Ø., Solberg, S., Stordal, F., Svendby, T. M., Simpson, D., Gauss, M., Hilboll, A., Pfister, G. G., Turquety, S., Richter, A., Burrows, J. P., and Denier van der Gon, H. A. C. (2012), Impact of forest fires, biogenic emissions and high temperatures on the elevated Eastern Mediterranean ozone levels during the hot summer of 2007, Atmos. Chem. Phys., 12, 8727-8750

[182] Péré, J. C., Mallet, M., Pont, V., and Bessagnet, B. (2011), Impact of aerosol direct radiative forcing on the radiative budget, surface heat fluxes, and atmospheric dynamics during the heat wave of summer 2003 over western Europe: A modeling study, J. Geophys. Res., 116, D23119

[183] Saide, P. E., Spak, S. N. , Pierce, R. B. , Otkin, J. A. , Schaack, T. K. , Heidinger, A. K., da Silva, A. M., Kacenelenbogen, M., Redemann, J., and Carmichael, G. R. (2015), Central American biomass burning smoke can increase tornado severity in the U.S, Geophys. Res. Lett., 42, 956–965

[184] Intergovernmental Panel on Climate Change (IPCC) (2014), IPCC Fifth Assessment Report, Climate Change 2013: The Physical Science Basis. [Available at https://www.ipcc.ch/report/ar5/wg1/, Accessed April 2, 2014.]

[185] Tosca, M. G., Randerson, J. T., Zender, C. S., Flanner, M. G., and Rasch, P. J. (2010), Do biomass burning aerosols intensify drought in equatorial Asia during El Niño?, Atmos. Chem. Phys., 10, 3515-3528

[186] Zhang, Y., Fu, R., Yu, H., Dickinson, R. E., Juarez, R. N., Chin, M., and Wang, H. (2008), A regional climate model study of how biomass burning aerosol impacts land-atmosphere interactions over the Amazon, J. Geophys. Res., 113, D14S15

[187] Jeong, G.-R., and Wang, C. (2010), Climate effects of seasonally varying Biomass Burning emitted Carbonaceous Aerosols (BBCA), Atmos. Chem. Phys., 10, 8373-8389

[188] Randles, C. A., and Ramaswamy, V. (2010), Direct and semi-direct impacts of absorbing biomass burning aerosol on the climate of southern Africa: a Geophysical Fluid Dynamics Laboratory GCM sensitivity study, Atmos. Chem. Phys., 10, 9819-9831

[189] Mao, J., Horowitz, L. W. , Naik, V., Fan, S., Liu, J., and Fiore, A. M. (2013), Sensitivity of tropospheric oxidants to biomass burning emissions: implications for radiative forcing, Geophys. Res. Lett., 40, 1241–1246

[190] Jacobson, M. Z. (2014), Effects of biomass burning on climate, accounting for heat and moisture fluxes, black and brown carbon, and cloud absorption effects, J. Geophys. Res. Atmos., 119, 8980–9002

[191] Vakkari, V., et al. (2014), Rapid changes in biomass burning aerosols by atmospheric oxidation, Geophys. Res. Lett., 41, 2644–2651

[192] Johnson, B. T. (2005), The Semidirect Aerosol Effect: Comparison of a Single-Column Model with Large Eddy Simulation for Marine Stratocumulus. J. Climate, 18, 119–130

[193] Washenfelder, R. A., et al. (2015), Biomass burning dominates brown carbon absorption in the rural southeastern United States, Geophys. Res. Lett., 42, 653–664

[194] Saleh, R., et al. (2014), Brownness of organics in aerosols from biomass burning linked to their black carbon content, Nat. Geosci., 7(9), 647–650

[195] Wang, C. (2013), Impact of anthropogenic absorbing aerosols on clouds and precipitation: A review of recent progresses, Atmos. Res., 122, 237–249

[196] Ban-Weiss, G. A., Cao, L, Bala, G., and Caldeira, K. (2012), Dependence of climate forcing and response on the altitude of black carbon aerosols, Climate Dyn., 38, 897–911

[197] Lee, S. S., Feingold, G., McComiskey, A., Yamaguchi, T., Koren, I., Vanderlei Martins, J., and Yu, H. (2014), Effect of gradients in biomass burning aerosol on shallow cumulus convective circulations, J. Geophys. Res. Atmos., 119, 9948–9964

[198] Ten Hoeve, J. E., Remer, L. A., and Jacobson, M. Z. (2011), Microphysical and radiative effects of aerosols on warm clouds during the Amazon biomass burning season as observed by MODIS: impacts of water vapor and land cover, Atmos. Chem. Phys., 11, 3021-3036

[199] Tummon, F., Solmon, F., Liousse, C., and Tadross, M. (2010), Simulation of the direct and semidirect aerosol effects on the southern Africa regional climate during the biomass burning season, J. Geophys. Res., 115, D19206

[200] Wan, H., Rasch, P. J., Zhang, K., Qian, Y., Yan, H., and Zhao, C. (2014), Short ensembles: an efficient method for discerning climate-relevant sensitivities in atmospheric general circulation models, Geosci. Model Dev., 7, 1961-1977

[201] Odman, M. T. (2014), "Emissions and Air Quality Modeling for SEMAP" Final Report to Southeastern States Air Resource Managers (SEMAP), Inc., 526 Forest Parkway, Suite F Forest Park, Georgia

[202] Sarwar, G., Luecken, D., Yarwood, G., Whitten, G., and Carter, B. (2008), Impact of an updated Carbon Bond mechanism on air quality using the Community Multiscale Air Quality modeling system: preliminary assessment. Journal of Applied Meteorology and Climatology, 47, 3-14

[203] Binkowski, F. S., and Roselle, S. J. (2003), Models-3 Community Multiscale Air Quality (CMAQ) model aerosol component 1. Model description, J. Geophys. Res., 108, 4183

[204] Kirchstetter, T. W., Novakov, T., and Hobbs, P.V. (2004), Evidence that the spectral dependence of light absorption by aerosols is affected by organic carbon,J. Geophys. Res.,109, D21208

[205] Russell, P. B., Bergstrom, R. W., Shinozuka, Y., Clarke, A. D., DeCarlo, P. F., Jimenez, J. L., Livingston, J. M., Redemann, J.,Dubovik, O., and Strawa, A.(2010), Absorption Angstrom Exponent in AERONET and related data as an indicator of aerosol composition, Atmos. Chem. Phys., 10, 1155–1169

[206] Yu, S., Mathur, R., Pleim, J., Wong, D., Gilliam, R., Alapaty, K., Zhao, C., and Liu, X. (2014), Aerosol indirect effect on the grid-scale clouds in the two-way coupled WRF–CMAQ: model description, development, evaluation and regional analysis, Atmos. Chem. Phys., 14, 11247-11285

[207] Kaskaoutis, D. G., Kharol, S. K. ,Sifakis, N., Nastos, P. T., Sharma, A. R., Badarinath, K.V. S., and Kambezidis, H. D. (2011), Satellite monitoring of the biomass-burning aerosols during the wildfires of August 2007 in Greece: climate implications, Atmos. Environ., 45, 716–726

[208] Bond, T. C., et al. (2013), Bounding the role of black carbon in the climate system: A scientific assessment, J. Geophys. Res. Atmos., 118, 5380–5552

[209] Lorenz, P., and Jacob, D. (2010), Validation of temperature trends in the ENSEMBLES regional climate model runs driven by ERA40, Clim. Res., 44, 167–177

[210] Bukovsky, M. S. (2012), Temperature trends in the NARCCAP regional climate models, J. Clim., 25, 3985–3991

[211] de Elía, R., Biner, S., and Frigon, A. (2013), Interannual variability and expected regional climate change over North America, Clim. Dyn., 41(5), 1245-1267

[212] Racherla, P. N., Shindell, D. T. , and Faluvegi, G. S. (2012), The added value to global model projections of climate change by dynamical downscaling: A case study over the continental U.S. using the GISS-ModelE2 and WRF models, J. Geophys.Res., 117, D20118